Odd-Z Transactinide Compound Nucleus Reactions Including the Discovery of ^{260}Bh

by

Sarah Lynn Nelson

B.S. (University of California, Santa Barbara) 2003

A dissertation submitted in partial satisfaction of the

requirements for the degree of

Doctor of Philosophy

in

Chemistry

in the

GRADUATE DIVISION

of the

UNIVERSITY OF CALIFORNIA, BERKELEY

Committee in charge:

Professor Heino Nitsche, Chair
Professor Joseph Cerny
Professor P. Buford Price

Spring 2008

The dissertation of Sarah Lynn Nelson is approved:

Chair: Date:

Date:

Date:

University of California, Berkeley

Spring 2008

Odd-Z Transactinide Compound Nucleus Reactions Including the Discovery of ^{260}Bh

by

Sarah Lynn Nelson

Abstract

Odd-Z Transactinide Compound Nucleus Reactions Including the Discovery of ^{260}Bh

by

Sarah Lynn Nelson

Doctor of Philosophy in Chemistry

University of California, Berkeley

Professor Heino Nitsche, Chair

Several reactions producing odd-*Z* transactinide compound nuclei were studied with the 88-Inch Cyclotron and the Berkeley Gas-Filled Separator at the Lawrence Berkeley National Laboratory. The goal was to produce the same compound nucleus at or near the same excitation energy with similar values of angular momentum via different nuclear reactions. In doing so, it can be determined if there is a preference in entrance channel, because under these experimental conditions the survival portion of Świątecki, Siwek-Wilczńska, and Wilczyński's "Fusion By Diffusion" model is nearly identical for the two reactions. Additionally, because the same compound nucleus is produced, the exit channel is the same.

Four compound nuclei were examined in this study: ^{258}Db, ^{262}Bh, ^{266}Mt, and ^{272}Rg. These nuclei were produced by using very similar heavy-ion induced-fusion reactions which differ only by one proton in the projectile or target nucleus (e.g.: ^{50}Ti + ^{209}Bi vs. ^{51}V + ^{208}Pb). Peak 1*n* exit channel cross sections were determined for each reaction in each pair, and three of the four pairs' cross sections were identical within

statistical uncertainties. This indicates there is not an obvious preference of entrance channel in these paired reactions. Charge equilibration immediately prior to fusion leading to a decreased fusion barrier is the likely cause of this phenomenon.

In addition to this systematic study, the lightest isotope of element 107, bohrium, was discovered in the ^{209}Bi(^{52}Cr,*n*) reaction. ^{260}Bh was found to decay by emission of a 10.16 MeV alpha particle with a half-life of 35^{+19}_{-9} ms. The cross section is 59^{+29}_{-20} pb at an excitation energy of 15.0 MeV. The effect of the $N = 152$ shell is also seen in this isotope's alpha particle energy, the first evidence of such an effect in Bh.

All reactions studied are also compared to model predictions by Świątecki, Siwek-Wilczńska, and Wilczyński's "Fusion By Diffusion" theory.

Dedication

This dissertation is dedicated to my brother Steven. You started out helping me with science at a very early age by showing me amoebae in your microscope and Jearl Walker's "Kinetic Karnival" programs. Later on you helped me understand the mole with M&Ms, assisting me through high school chemistry. During my entire college education you have been there for me, whether to answer a physics question or to complain to about the annoyance of the day. As many times as I wanted to quit, you were there to listen and talk me off the academic ledge. For all of this, talks about cooking, HBO, beer, cars, and so much more, this work is for you.

Table of Contents

List of Figures

List of Tables

Acknowledgments

First of all I would like to thank my graduate advisor Heino. From my beginnings as a naïve first-year graduate student pitching wacky ideas for research, to driving out to Livermore for side projects, to the meat of this work presented here, you have always been supportive and open-minded. I also learned that an advisor that cares about his graduate students as human beings is a valuable thing indeed.

I would like to bow in honor to Ken Gregorich for his ever-flowing wisdom and patience to answer the dumbest of dumb questions. Without your help I would still be scratching my head, trying to figure out how to set anything up or cursing at my compiler. You made this work happen.

Many thanks also go to Darleane Hoffman for impromptu talks about all manner of science, and more importantly, advice about being a woman in physical science. You are a role model to me, and if I achieve half of what you have in your career I will consider myself successful.

To the staff and post-docs that have helped me so much: Ralf Sudowe, Chris Düllmann, Cody Folden, Robert Eichler, Liv Stavsetra, and Jan Dvořák, when I was too embarrassed to ask someone else a dumb question I went to one of you. You also provided great moral support to me on many occasions when I was usually worrying about something irrational or got so frustrated I broke down.

Many thanks are also in order to the LLNL bunch that I knew before I even came to Berkeley: Ken Moody, Jackie Kenneally, Dawn Shaughnessy, Joshua Patin, and later on, Philip Wilk. Thanks for help with practice talks and qual exam questions, expanding my radiochemistry experience, and pointers on how to survive the Berkeley graduate chemistry machine.

Great technical thanks go the operations staff of the 88-Inch Cyclotron, especially Jim Morel, Daniela Leitner, Michelle Galloway, Bill Tiffany, and all the operators, whose expertise and help got every experiment off the ground regardless of the sometimes numerous and serious problems that came up. Thanks also to Mike Johnson for many stimulating discussions about everything.

Deep thanks go to my late seventh grade science teacher Ms. Hansen, who indirectly ignited my interest in transuranic elements and never discouraged me from reading about them from college chemistry texts when I was "supposed to" be reading fiction for ten minutes each day. I would also like to thank my high school honors chemistry teacher Mr. Brett for encouraging women to go into science, for teaching nuclear science, and for not letting me go to the regular level course when the going got tough. Additional thanks go to the late Dr. Aaron D. Brown (or "Dr. B" as we would call him), my Chem 1 professor at Ventura College. You were a man of great integrity, wisdom, and a source of inspiration to me at a very dark time in my life. I only wish that you were around today so I could share with you how far you helped me go in science.

I would like to thank my friends, Joe Hickey & Karma Sawyer for many lunches, dinners, trips to Yogurt Park, long homework sessions, and general complain-o-ramas

over these years. You guys are rock stars and will always have a special place in my heart. Best wishes to you both, you deserve the best!

I would like to thank my family, specifically my dad and my brother Steve, for their support through this process. We have had many long phone conversations with me wondering if this was all worth it, was I smart enough to be in Berkeley, should I finish this, etc. Thanks for your patience and encouragement over many long years.

1. Introduction

This dissertation involves the study of the transactinide elements, or those elements possessing a proton number, or *Z*, greater than or equal to 104. These elements are located in row seven in the periodic table and represent the filled 5f electron shell and filling of the 6d shell. The transactinide (TAN) series can be viewed in Figure 1.1, the present-day periodic table of the elements. All TAN elements are unstable to radioactive decay and must be produced by artificial means such as a particle accelerator.

Detailed characterization of new transactinide elements and their various isotopes is required prior to their chemical study. Decay properties such as half-lives, decay modes and their branching, and production cross sections are all essential to an understanding of their nuclear properties. In addition to preparing us for chemistry studies, these data are vital to the understanding of nuclear structure, the existence and strength of spherical and deformed shell gaps, and they also aid in strengthening models used to make valuable predictions.

The production and identification of transactinide elements present many challenges, not the least of which are their short half-lives and low production rates. These elements can only be synthesized one atom at a time, and sensitive detection equipment is required for conclusive identification. Formerly, elements up to mendelevium ($Z = 101$) were identified by chemical separation [1]. Today, physical separation and identification methods are required to avoid potentially controversial

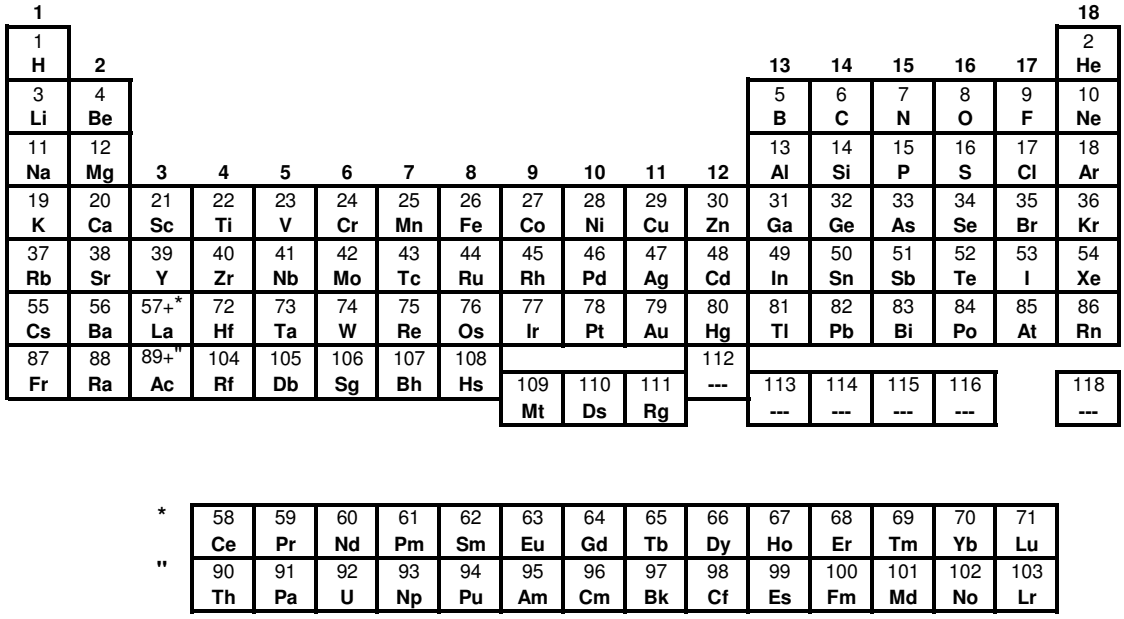

Figure 1.1: Periodic table of the elements (as of May 2008). Transactinide elements that are partially placed in periods 9-11 and 13-18 are those for which chemistry has not been investigated.

claims made by chemical separations alone. Equipment such as magnetic rigidity [2] and velocity separators [3] aid in physically reducing the large amount of unwanted background activities. To date, fourteen TAN elements spanning *Z* from 104 - 116 and 118 have been reported, and eight have been named. A table detailing these discoveries is presented in Table 1.1. It should be noted that many of these claims were/are not without considerable controversy over discovery credit and naming rights. Because few research facilities in the world have the equipment to run such experiments, it may be some time before the most recent claims can be independently verified. An addition to the excitement surrounding the production and verification of a new element, the cross sections for these yet unconfirmed elements by Oganessian *et al.* are surprisingly

Z	Name and Symbol*	Year/s Discovered	Reaction/s Used	Laboratory of Discovery	Other Names and Symbols Used
104	rutherfordium, Rf	1964-99	$^{249}Cf(^{12}C, xn)^{261-x}Rf$, $^{249}Cf(^{13}C,xn)^{262-x}Rf$	LBNL [4]	kurchatovium, Ku, dubnium, Db
105	dubnium, Db	1968-70	$^{243}Am(^{22}Ne,4\text{-}5n)^{265-x}Db$	JINR [5]	hahnium, Ha, joliotium, Jl. nielsbohrium, Ns
106	seaborgium, Sg	1974	$^{249}Cf(^{18}O,4n)^{263}Sg$	LBNL [6]	rutherfordium, Rf
107	bohrium, Bh	1981	$^{209}Bi(^{54}Cr,n)^{262}Bh$	GSI [7]	nielsbohrium, Ns
108	hassium, Hs	1984	$^{208}Pb(^{58}Fe,n)^{265}Hs$	GSI [8]	hahnium, Ha
109	meitnerium, Mt	1982	$^{209}Bi(^{58}Fe,n)^{266}Mt$	GSI [9]	-
110	darmstadtium, Ds	1994	$^{208}Pb(^{62}Ni,n)^{269}Ds$	GSI [10]	-
111	roentgenium, Rg	1994	$^{209}Bi(^{64}Ni,n)^{272}Rg$	GSI [11]	-
112	Confirmed but unnamed	1996	$^{208}Pb(^{70}Zn,n)^{277}112$	GSI [12]	-
113	unnamed	2003-04	$^{209}Bi(^{70}Zn,n)^{278}113$, $^{237}Np(^{48}Ca,3n)^{282}113$	RIKEN [13], JINR [14]	-
114	unnamed	1999	$^{244}Pu(^{48}Ca,3n)^{289}114$	JINR [15]	-
115	unnamed	2004	$^{243}Am(^{48}Ca,3\text{-}4n)^{287,288}115$	JINR [14]	-
116	unnamed	2000	$^{248}Cm(^{48}Ca,3n)^{293}116$	JINR [16]	-
118	unnamed	2006	$^{249}Cf(^{48}Ca,3n)^{294}118$	JINR [17]	-

Table 1.1: Names, symbols, and periods of discovery for the transactinide elements. Reactions used are displayed with the laboratories of discovery. Other names and symbols used in the literature are listed as well for clarification.
*Names assigned by the International Union of Pure and Applied Chemistry (IUPAC).

consistent, at or near one picobarn (pb) (see [18] for a review). It will be interesting to learn if these results stand the test of time upon another laboratory's verification.

1.1 The Compound Nucleus

Because no TANs exist in nature, and they must be produced by artificial means, we will examine the methods by which this takes place. Bombardment of thin targets by ion beams to produce a compound nucleus (CN) is the common method of TAN production. A CN is produced when the projectile and target nuclei fuse to become a single body, and the incident energy is shared among the nucleons. A symbolic representation of a CN reaction is shown below:

$$a + X \rightarrow C^* \rightarrow Y + b \qquad \text{Equation 1.1}$$

where a and X represent the target and projectile, respectively, C^* represents the excited-state CN, and Y and b represent the product and emitted particles, respectively. The CN only exists for an unobservably short amount of time, on the order of 10^{-16} – 10^{-19} s. Once formed, it does not "remember" the method of formation (other than its excitation energy and angular momentum) and decays according to statistical rules [19]. We will see that this is a crucial concept to many studies presented in this dissertation.

There is a considerable amount of excitation energy in the CN dependent on the reaction used, and de-excitation occurs via particle emission or fission. The emitted particles carry away a portion of the excitation energy, and more than one particle may be emitted in this process. Neutron emission in de-excitation is energetically more favorable than charged particle emission due to the neutrons not needing to overcome the influence of the Coulomb barrier.

$$V_C = \frac{Z_1 Z_2 e^2}{r} \qquad \text{Equation 1.2}$$

The classic expression for the Coulomb barrier is seen above in Equation 1.2 [19]. Z_1 and Z_2 represent the proton numbers of the interacting nuclei, r represents the interaction

distance, commonly written as: $r = R_o (A_1^{1/3} + A_2^{1/3})$, where R_o = 1.2 fm. In TAN formation, fission of the CN occurs more often than particle emission, resulting in low production rates.

Cross sections, symbolized by σ, represent the relative probability for a given nuclear reaction to occur. The units associated with a cross section are those of area. The expression for the reaction cross section is [19]:

$$\sigma = \frac{R}{I * N} \qquad \text{Equation 1.3}$$

where R is the production rate of the nuclide of interest, I is the incident particle flux from the beam in particles/area, and N represents the number of target nuclei present per unit area. The unit used in discussing cross sections is the barn, which is equal to 10^{-24} cm^2. Typical TAN cross sections are in the nb to pb range (10^{-33} – 10^{-36} cm^2).

Sequences of cross sections plotted as a function of their energy are known as excitation functions. The excitation function for a particular de-excitation pathway, or exit channel, will increase in magnitude with increasing projectile energy because of the increasing probability that the two nuclei will fuse. At a particular energy this increase will slow and quickly decrease with increasing energy due to the increased losses to fission of the excited CN, or the emission of a neutron. More specific information about excitation functions may be found in Section 1.4.2.1. Measuring these excitation functions is very important in the study of TANs, as it can yield valuable information about the physics of the specific reaction.

1.2 Compound Nucleus Reaction Types

There are two types of heavy-ion induced fusion reactions: hot fusion and cold fusion. The main difference between the two is the range of CN excitation energies achieved during the reaction. Hot fusion reactions typically use light ion projectiles such as ^{15}N, ^{18}O, or the doubly-magic ^{48}Ca, on actinide targets such as ^{238}U or ^{244}Pu. These reactions occur at compound nucleus excitation energies of ~30 MeV and greater at which the emission of three or more neutrons (or charged particles) is favorable. The projectile and target combinations used in this type of reaction tend towards the neutron-rich side and thus are desired in the search for the so-called "Island of Stability" for TAN elements ([18], see [20] for a review). This island is a region of the chart of nuclides that is thought to be both proton and neutron shell-stabilized [21], resulting in relatively long half-lives, and is in early stages of its scientific exploration [18].

The reactions used by the Joint Institute for Nuclear Research (JINR) in Dubna, Russia to synthesize elements 114, 115, 116, and 118 are all examples of hot fusion reactions. Their use of a doubly-magic ^{48}Ca beam is believed to lower the excitation energy of the fusing system somewhat, helping to partially reduce losses of the CN to fission compared to that of a non-spherical projectile.

Predictive codes such as HIVAP [22] are available which model hot fusion reactions, enabling the experimenter to have a better estimate of the outcome of a particular reaction. These codes are quite complex and involve the use of many parameters, as hot fusion reaction mechanics are not yet well understood.

Cold fusion reactions are, as the name would suggest, "cold". These reactions involve compound nucleus excitation energies on the order of 10-25 MeV and the

evaporation of only 1-2 neutrons, in contrast to the 3+ neutrons of a hot fusion type reaction. Medium-mass projectiles such as ^{50}Ti or ^{54}Cr are used with spherically shell-stabilized targets of ^{208}Pb or ^{209}Bi. This type of reaction tends to produce isotopes toward the more neutron-deficient side of the chart of nuclides. An advantage that cold fusion reactions have is that the CN is formed with a relatively low excitation energy, which decreases the competition from fission during de-excitation. An additional advantage to using a spherical, shell-stabilized target is the assertion that the "hard" spherical target nucleus allows fusion even at large values of *x*, or effective fissility [23], which will be discussed in the following section. These reduced losses to fission mean an increase in cross section, which is why researchers at GSI used this type of reaction in the discovery of elements 107-112 (see [24] for a review).

1.3 Effective Fissility

In addition to the group at the Gesellschaft für Schwerionenforschung (GSI) using cold fusion reactions with enhanced survivability to fission (as opposed to the hot fusion reactions), they chose to study more asymmetric reactions producing odd-*Z* TANs. It was believed that this combination of reducing losses to fission by choice of reaction type, along with choice of reaction pathway, would lead to higher cross sections and greater success in the synthesis of TAN elements. The idea that more asymmetric reactions (relatively speaking) would possess larger cross sections comes from the concept of effective fissility [23, 25]. This fissility parameter is a macroscopic scaling factor that does not take into account nuclear structure effects. It is calculated as a

weighted mean of the dinuclear system's probability to fission before and after fusion, denoted by x:

$$x = (Z/101.8)\, f(I)\, [(1 - \alpha) + \alpha f(\kappa)] \qquad \text{Equation 1.4}$$

$$f(I) = (1 - I)/(1 - 1.78I^2) \qquad \text{Equation 1.5}$$

$$I = (N - Z)/(N + Z) \qquad \text{Equation 1.6}$$

$$f(\kappa) = 4/(\kappa^2 + \kappa + \kappa^{-1} + \kappa^{-2}) \qquad \text{Equation 1.7}$$

$$\kappa = (A_1/A_2)^{1/3} \qquad \text{Equation 1.8}$$

where $f(I)$ and I are related to the proton-neutron asymmetry, $f(\kappa)$ and κ take into account decreasing Coulomb energy, and the weighting parameter $\alpha = 1/3$ is determined from a fit to experimental data. This quantity has a direct relationship to the asymmetry of the reaction in question. When producing the same CN, an asymmetric reaction will have a lower effective fissility than a more symmetric reaction. Adding neutrons to the heavier member of the reaction (almost always the target, in heavy element studies) will reduce the value of x. Lower effective fissilities represent higher cross sections, because the CN is allowed to form at lower excitation energies and the losses to fission are diminished. A diagram of various hot and cold fusion reaction cross sections as a function of their fissilities is presented in Figure 1.2. This clearly illustrates the differences in reaction type, as their cross sections vary as a function of their effective fissilities.

1.4 Fusion Models

The classic treatment regarding the synthesis of compound nuclei is from the work of Sikkeland *et al.* [26], drawn from earlier work by Jackson [27]. This model treats CN formation as the product of two parameters: 1) The capture cross section of the

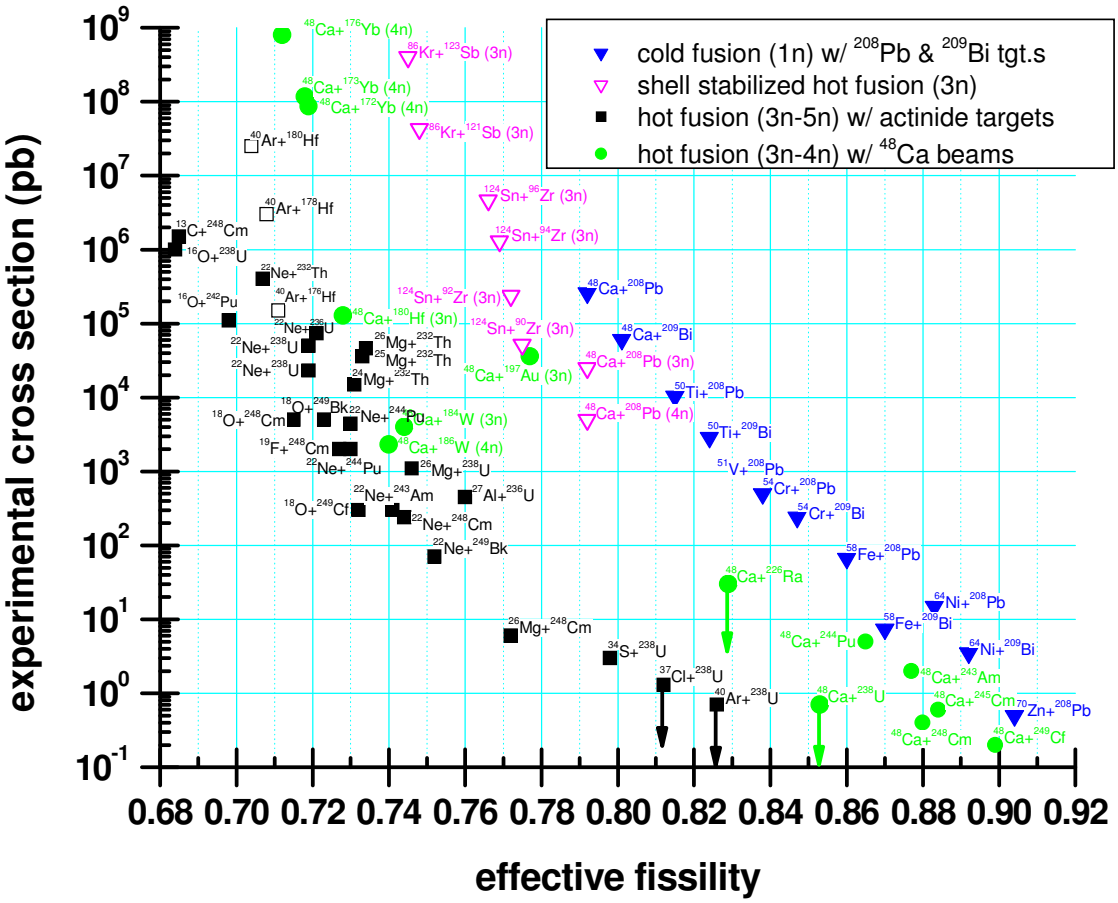

Figure 1.2: Graph of experimental cross sections as a function of their effective fissility. Filled squares represent hot fusion reactions, and downward-facing filled triangles represent cold fusion reactions with shell-stabilized Pb and Bi targets. Data compiled by K. E. Gregorich.

projectile and target nuclei (also referred to as "sticking"), and 2) the probability of this excited CN to survive fission by emitting neutrons (or protons, or alpha particles; also referred to as "surviving"). The cross section for the evaporation of x neutrons is given by:

$$\sigma_X = \sigma_{CN} P_X \prod_{i=1}^{X} \left(\frac{\Gamma_n}{\Gamma_n + \Gamma_f}\right) \qquad \text{Equation 1.9}$$

where σ_{CN} is the cross section for CN formation, P_X is the probability of emitting x neutrons, and Γ_n and Γ_f are the partial widths for neutron emission and fission, respectively. These widths are quantities proportional to the decay probability of the mode in question. The classical expression for σ_{CN} is:

$$\sigma_{CN} = \pi r^2 (1 - \frac{V_C}{E}), \qquad (E > V_C) \qquad \text{Equation 1.10}$$

where r is again our interaction distance, V_C is the Coulomb barrier, and E is the energy of the projectile. This indicates that CN production is not possible at energies below the Coulomb barrier. We now know this is not the case, as fusion below the nominal classical barrier does exist due to a number of factors including: Quantum mechanical tunneling through the barrier [28], projectile and target deformations and vibrations, and neck formation near contact.

This treatment of cross sections works well for the synthesis of lighter nuclei up to Fm. However, as these CN increase in Z and A, this approach begins to break down by orders of magnitude, failing to predict the formation of elements such as $Z = 112$. Another factor must be responsible for the deterioration of this method at higher Zs and masses.

1.4.1 Hindrance to Fusion in Heavy Element Synthesis

Much work has been done to investigate the reason for this hindrance to fusion in the heaviest elements, and it is now believed to be essentially the result of nuclear geometry [25, 29]. We know that the CN is formed in a "pocket" in the mutual nuclear and Coulomb potentials, which can be seen as a minimum in Figure 1.3, the reaction of ^{70}Zn with ^{208}Pb at 235 MeV. One coordinate of this multidimensional space is the

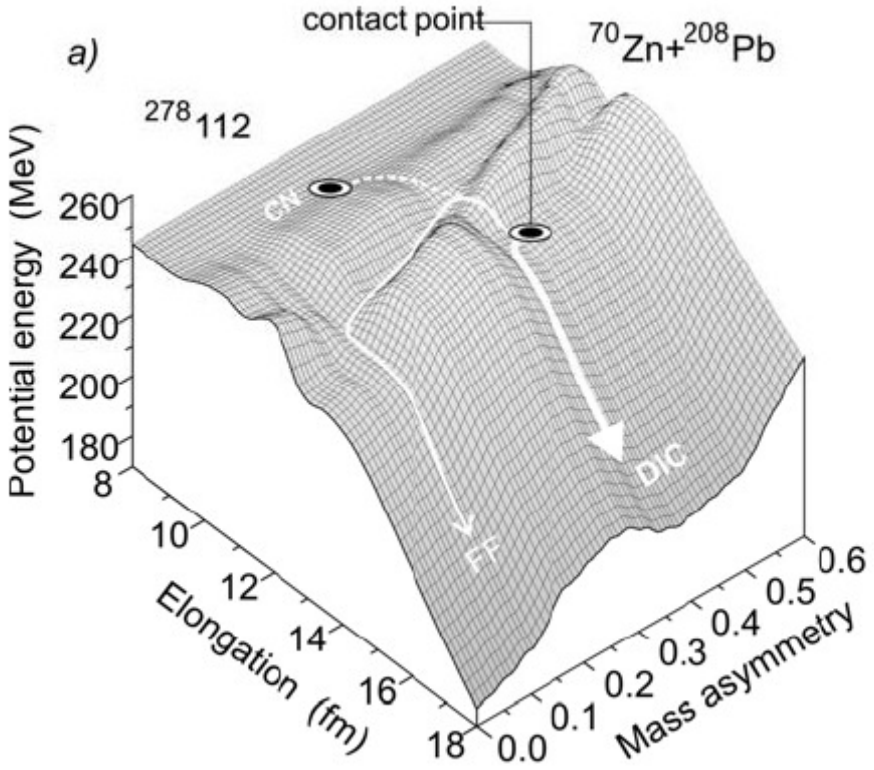

Figure 1.3: Graphical representation of the potential energy surface, showing the possible paths a dinuclear system can take at the point of contact. CN stands for compound nucleus, FF stands for fusion-fission, and DIC stands for deep inelastic collision. Adapted from [18].

elongation of the system. In the case of the fusing system, this is the sum of the nuclear diameters in the touching configuration. There is a critical size at which the system will fall on the inside of the fission saddle (viewed from the side of the elongation and potential energy axes) and coalesce into a single body, or be formed on the outside of the saddle point and re-disintegrate into two bodies. A graphical representation of this for a light and heavy system may be viewed in Figure 1.4. The effective fissility of the system is an important consideration as well, because a more asymmetric system will have a

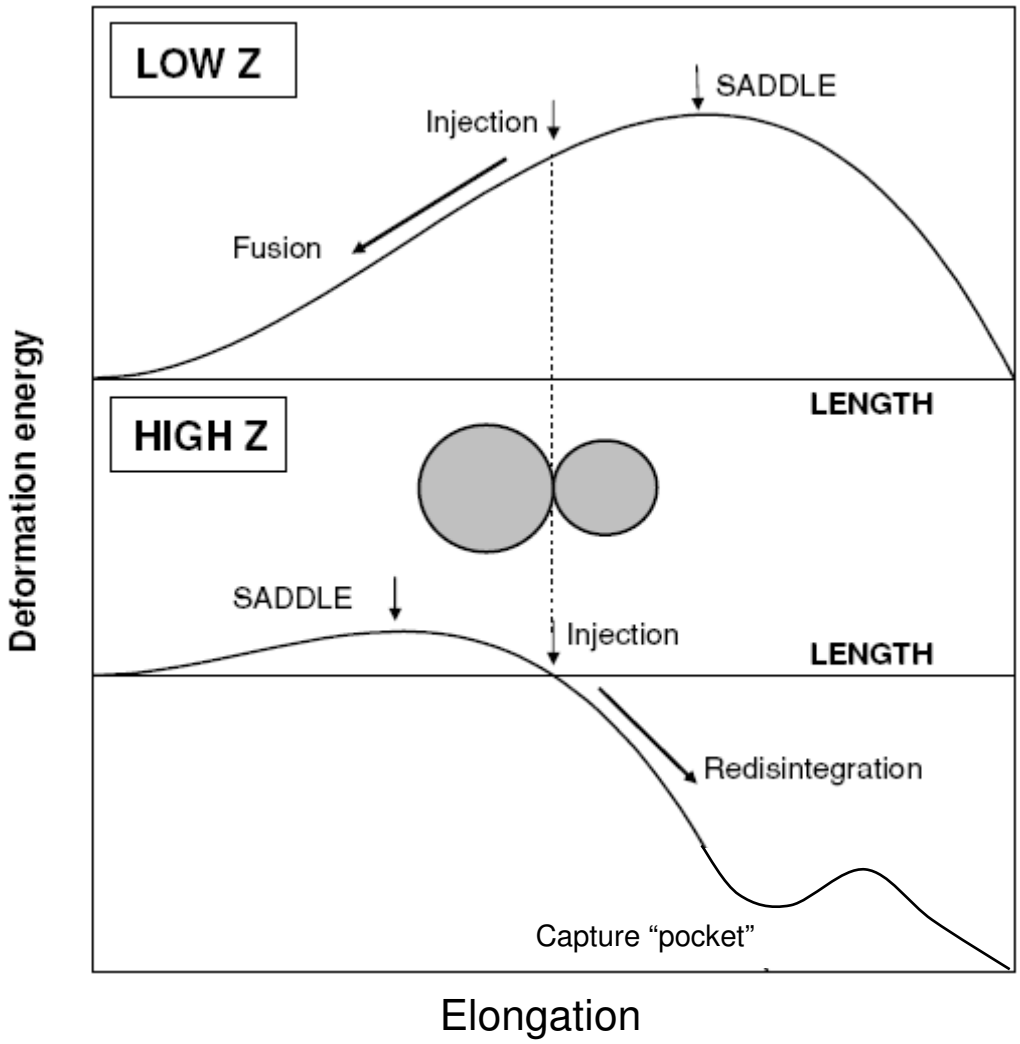

Figure 1.4: Two-dimensional representation of hindrance to fusion, resulting from the location of the fusing system on the fission barrier. Adapted from [29].

smaller overall elongation and a higher probability of falling on the favorable side of the barrier for CN formation.

Classically speaking, if the nuclei come into contact on the unfavorable side of the fission barrier, there is a zero probability for the system to fuse. We know this conclusion not to be completely true, because we have observed heavy elements corresponding to this situation. All TANs formed in cold fusion type reactions to-date

have been formed below the barrier (see Section 1.4.2.2), and by virtue of their existence we know there is a finite probability for sub-barrier fusion.

Świątecki, Siwek-Wilczyńska, and Wilczyński have developed a model incorporating a novel diffusion term known as the "Fusion By Diffusion" model [29, 30]. Together with the aforementioned "sticking" and "surviving" terms, it reproduces experimental 1*n* cross sections very well.

1.4.2 "Fusion By Diffusion"

This new diffusion term arises from the elegantly simple treatment of the system as a one-dimensional thermally fluctuating body faced with a parabolic barrier, devised by Świątecki *et al*. At a fixed total energy of the system, the thermal shape variations allow for a small probability for the system to eventually "diffuse" over this barrier. The relation presented for this factor of the model is:

$$P_{diffuse} = (1 - erf\sqrt{H/T})/2 \qquad \text{Equation 1.11}$$

where *erf* is the error function, H represents the barrier height, and T represents a mean temperature of the system. For cold fusion reactions, the value of T is approximately 0.6 MeV. The system is in a lower energy state after fusing based on the lower surface area of the new single body as compared to the di-nuclear system, and this process occurs rapidly. The authors use the term "injection point", x_o, to describe the elongation (assumed to be a delta function at $t = 0$) at which the two nuclei begin to diffuse. However, at $t > 0$, the distribution rapidly spreads about a mean of x_o. A small portion of this distribution diffuses over the parabolic barrier, providing a probability for the CN to not immediately re-disintegrate. This is presented graphically in Figure 1.5.

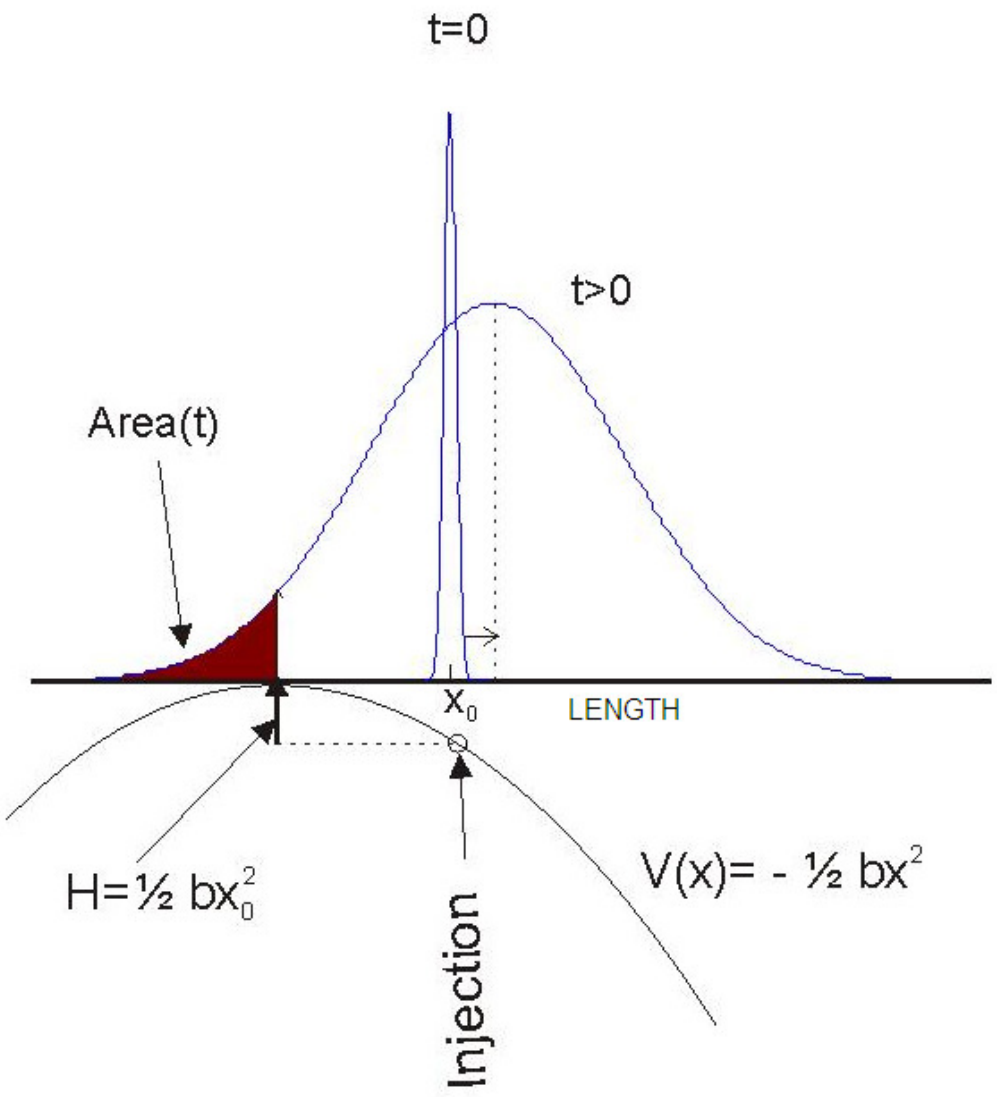

Figure 1.5: Graphical representation illustrating diffusion over the "sticking" barrier. At the point of injection ($t = 0$) the entire distribution is on the unfavorable side of the barrier. At $t > 0$ this Gaussian distribution is widened, allowing the shaded portion to "diffuse" over the barrier. Adapted from I. Dragojević [31].

In the case when the "Fusion By Diffusion" (FBD) model is applied to reactions where only one neutron is emitted during de-excitation, it is important that the competition between neutron emission and fission be accounted for, and that the nucleus

not fission nor emit another neutron after the first neutron is emitted. Świątecki *et al.* [29, 30, 32] present enhanced versions of the conventional Γ_n/Γ_f and σ_{CN}, along with the new diffusion term to arrive at a new three-factor expression for CN formation and survival represented by Fusion = Stick * Diffuse * Survive, or:

$$\sigma_{1n} = \sigma_{CN} P_{diffuse} P_{survive} \qquad \text{Equation 1.12}$$

1.4.2.1 "Optimum Energy Rule"

All three factors in the FBD model are functions of the same center of mass projectile energy, and their product leads to a theoretical 1*n* excitation function, as well as the energy at its peak. Świątecki *et al.* have deconstructed the shape of an excitation function into its constituent parts. There is a rapid increase in cross section above the threshold for the emission of one neutron and all three factors in Equation 1.12 increase rapidly. This increase turns over abruptly when the energy reaches the threshold for second-chance fission (fission after the first neutron has been emitted) or for the emission of a second neutron, whichever is lower. The cross section continues to decrease rapidly with increasing energy. This individual increase and decrease can be modeled with exponential functions. The approximately Gaussian-like appearance of many experimental excitation functions is a result of the energy loss over the target thickness. An illustrative example may be seen in Figure 1.6.

To calculate the optimum bombarding energy for a 1*n* reaction, one ideally desires to produce this nucleus at an energy high enough to increase the probability of fusion, but low enough such that second chance fission is not possible. In this dissertation it has been calculated as:

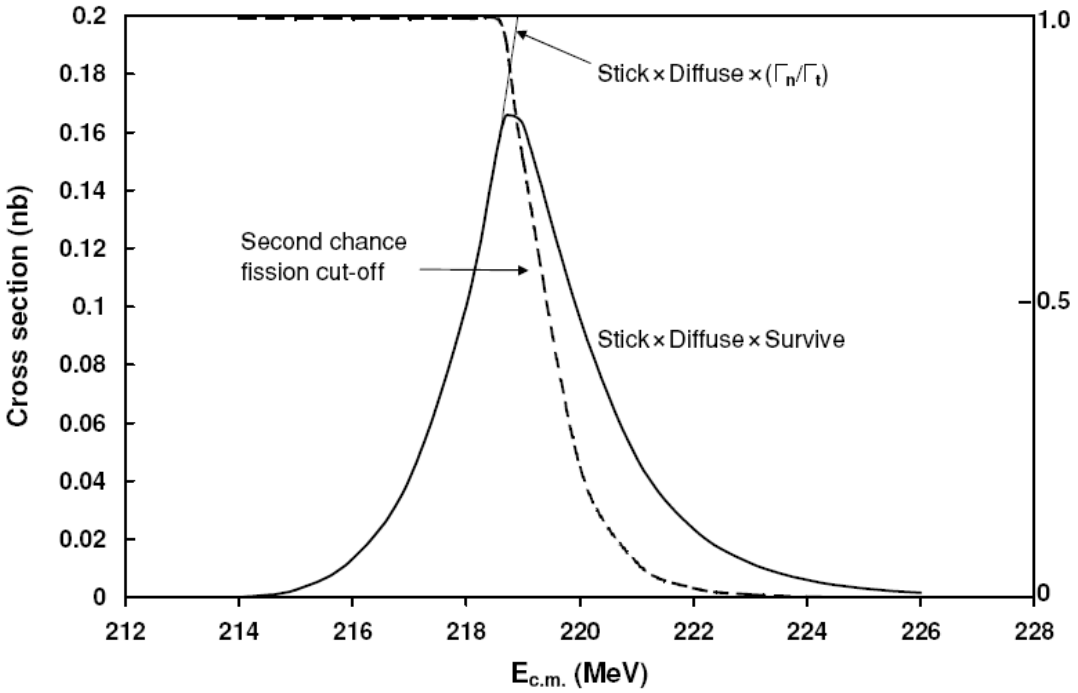

Figure 1.6: An excitation function shown as the intersection of two exponential-like functions. As the energy increases, the cross section increases rapidly until the cutoff for second chance fission is reached. Data are shown for the ^{58}Fe + ^{208}Pb reaction, adapted from [29].

$$E_{CM,\,opt} = (M_{CN-1} + M_n + B_f) - (M_{proj} + M_{tgt}) + 0.3\ MeV \qquad \text{Equation 1.13}$$

where M_n is the mass of the emitted neutron, B_f is the fission barrier or shell correction energy, M_{proj} and M_{tgt} are the masses of projectile and target nucleus, respectively. Additionally, for the reactions producing ^{260}Bh and ^{266}Mt studied in this dissertation, an empirically-derived energy offset was added to the final value calculated by the "Optimum Energy Rule" [33]. During the course of this study, Świątecki informed us that the reactions producing odd-Z CN required an additional 1 – 3 MeV to reach the true maximum of the excitation function. Experimental results seem to agree, and will be discussed where appropriate.

1.4.2.2 An Enhanced Barrier

Because the conventional treatment of the Coulomb barrier assumes the two interacting bodies are static and spherical, a more sophisticated approach to calculating an interaction barrier, *B*, has been produced by Świątecki *et al.* [29] in development of the FBD model. Their semi-empirically derived formula comes from fitting the sticking cross section of forty-five reactions, and obtaining good values for *B* and *v*, the barrier and its Gaussian distribution. These values were then plotted as a function of the Coulomb parameter *z* [29]:

$$z = \frac{Z_1 Z_2}{(A_1^{1/3} + A_2^{1/3})} \qquad \text{Equation 1.14}$$

A cubic fit was extrapolated from their findings, and is presented with new and unpublished constants [29, 32]:

$$B = 0.86665612z + 0.00099062z^2 - 0.0000012434z^3 \qquad \text{Equation 1.15}$$

We use this method of calculating *B* for all reactions contained in this work, and examine what, if any, relationship the barrier has to the cross sections.

1.5 Scope

In this dissertation, experiments producing various odd-*Z* TAN isotopes are investigated. These studies are of interest for many reasons. By studying reactions that make the same compound nucleus by changing only the location of one proton between the reactions (e.g.: ^{50}Ti + ^{209}Bi vs. ^{51}V + ^{208}Pb), we may test the effect the entrance channel has on the cross section. This work is similar in philosophy to the work of S. N. Ghoshal [34] where pairs of reactions producing ^{63}Zn, ^{62}Zn, and ^{62}Cu were studied.

The reactions producing odd-*Z* TAN CN such as Db, Bh, Mt, and Rg (*Z* = 105, 107, 109, and 111, respectively) were first studied using even-*Z* projectiles on ^{209}Bi targets (as opposed to odd-*Z* projectiles on ^{208}Pb targets) because lower effective fissility was expected to lead to larger cross sections. Many odd-*Z* projectile reactions producing odd-*Z* CN had not been studied in-depth until this project was undertaken. The goal of this work was to study the missing reactions in these pairs, and to re-examine reactions with large cross sections. The reaction pairs of interest are presented in Table 1.2, and the decay properties of those reaction products synthesized and studied in this work are depicted in Figure 1.7.

The reactions in this study are the only ones feasible for this type of systematic study, because the odd-*Z* element lower in *Z* than Db is lawrencium (Lr), not a TAN, and the odd-*Z* element higher than Rg is element 113, with low cross sections that would make its measurement impractical. An equivalent even-*Z* CN study is not yet possible. To achieve a set of even-*Z* reactions only differing by one proton one would require the use of a radioactive target or projectile that is beyond current experimental capabilities. This systematic study is now complete, with only work to further refine the results left to be examined.

Nuclide	Reaction	Previous Work	Reactions Studied in This Work
^{258}Db	^{208}Pb(^{51}V,*n*)	n/a	Chapter 3
	^{209}Bi(^{50}Ti,*n*)	GSI [7, 35, 36]	Chapter 3
^{262}Bh	^{208}Pb(^{55}Mn,*n*)	LBNL [37]	Chapter 4
	^{209}Bi(^{54}Cr,*n*)	GSI [7, 38]	Chapter 4
^{266}Mt	^{208}Pb(^{59}Co,*n*)	n/a	Chapter 6
	^{209}Bi(^{58}Fe,*n*)	GSI [9, 39, 40]	-
^{272}Rg	^{208}Pb(^{65}Cu,*n*)	LBNL [41]	-
	^{209}Bi(^{64}Ni,*n*)	GSI [11, 42], RIKEN [43]	-

Table 1.2: Summary of odd-*Z* transactinide reaction pairs, indicating those reactions studied before to 2003, and those reactions which are presented in this dissertation.

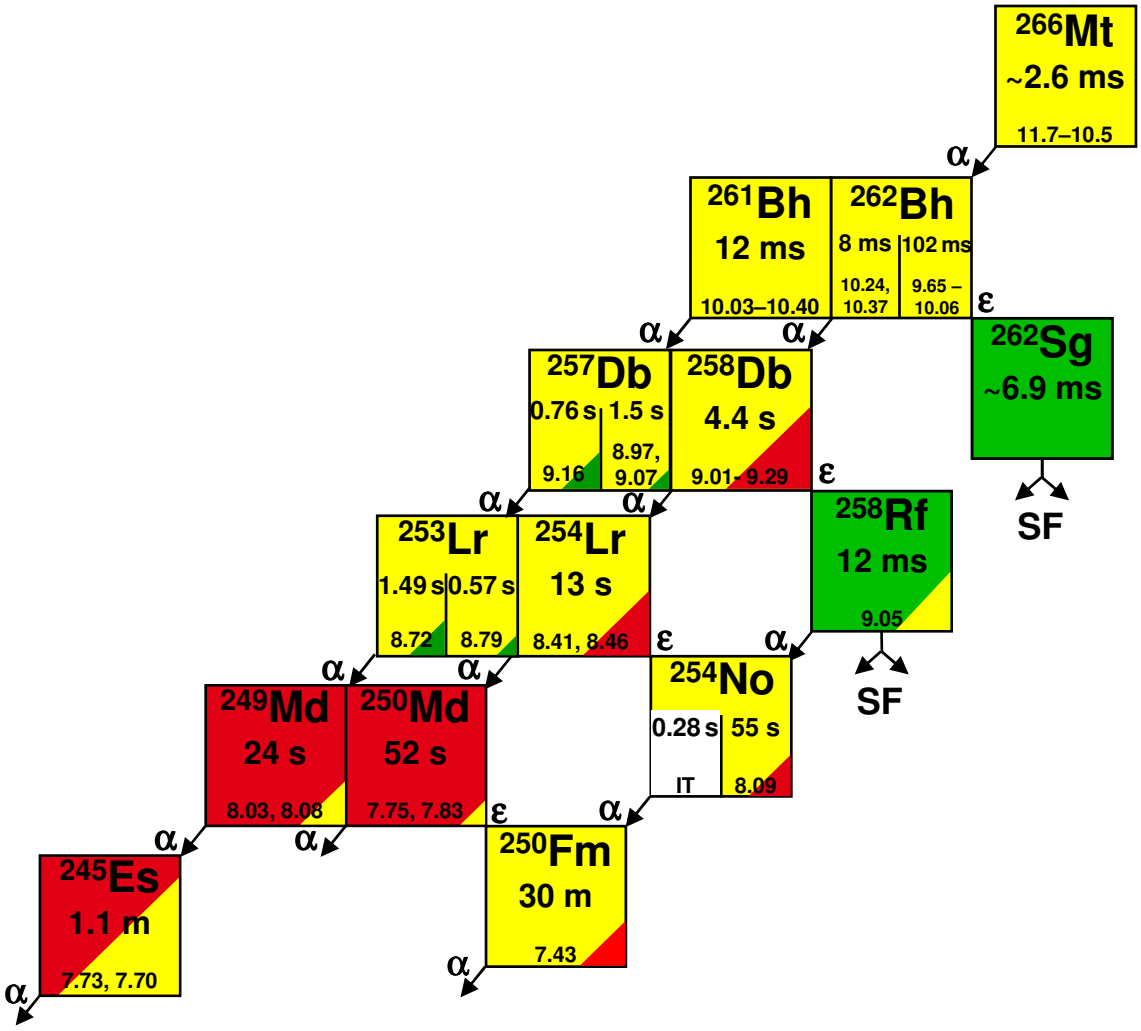

Figure 1.7: Decay properties of nuclides produced in the study of differing entrance channels. Detailed information about each nuclide can be found in each chapter's results section. Energies listed in MeV. Data from [35-39, 44-49].

W. J. Świątecki [50] has provided us with predictions of these reactions' cross sections and their optimum bombarding energies. If the same CN is produced at or near the same excitation energy, the survival portion of the FBD model is nearly identical for the two reactions. Since capture cross sections are relatively well-understood, this

method can be used as a critical test of the novel "diffusion" portion of the model. His predictions are compared to our experimental results and the previous results on ^{266}Mt by GSI in Darmstadt, Germany [40], ^{272}Rg by GSI [11, 42] and the Institute of Physical and Chemical Research (RIKEN) in Saitama, Japan [43]. We also examine any possible role the barrier *B* plays in cross section magnitudes.

Świątecki also provided us with a prediction of the cross section and peak location for the new isotope ^{260}Bh [51] that was discovered during the course of these experiments. The discovery of any new TAN isotope adds to our knowledge and understanding of this relatively new and unexplored region of the chart of nuclides. Models used to predict nuclear and decay properties such as masses, decay energies, half-lives, proton and neutron shells, etc. are enriched with each new discovery such as this.

2. Experimental Apparatus and Procedures

Several experimental components are required for a successful heavy-ion induced-fusion reaction to take place. Specific data analysis treatments are also necessary for an accurate understanding of the data acquired. Here, these items and methods are presented in detail.

2.1 Experimental Apparatus

The ions for the beam are generated by the upgraded advanced electron cyclotron resonance (AECR-U) ion source at the LBNL 88-Inch Cyclotron, accelerated to the appropriate energy, and directed to our experimental area. The beam is then focused by a series of magnets, passes through a collimator, and encounters a thin carbon foil, or "window". This window separates the evacuated beamline from the 0.5 Torr (67 Pa) of helium fill gas used in the Berkeley Gas-Filled Separator (BGS). The window consists of natural carbon at a thickness of 45 $\mu g/cm^2$. Because of damage sustained during high-intensity BGS experiments, these windows break approximately every two to three days. A telescoping arm containing five carbon windows aids in rapid replacement of broken windows, as the experiment cannot proceed without one. After passing through this carbon window, the beam encounters our target system. Two types of targets are used at the BGS, stationary targets and rotating wheel targets.

2.1.1 Targets

2.1.1.1 Stationary Targets

The stationary targets are used primarily for low beam intensity experiments such as producing short-lived isotopes for TAN homologue chemistry studies [52], or for producing short-lived alpha activity for BGS focal plane detector calibration. These targets are small. They are affixed to aluminum frames with approximately 6 – 10 mm diameter openings for the beam and reaction products to pass through. Backing materials consist of carbon or thin aluminum. Target materials vary dependent upon what the specific needs of the experimenter require. In this work, rare earth targets such as ^{173}Yb were used. Because these targets are not cooled, beam intensities must be kept to the 100-nA range to avoid damaging or destroying them. Up to five stationary targets are mounted on a telescoping arm which allows the assembly to be retracted when not in use. This arm is also fully retracted when conducting BGS experiments with the rotating wheel targets.

2.1.1.2 Rotating Target Wheel

The beam intensities used in TAN experiments with the BGS need to be higher than what a stationary target could withstand, approximately 0.5 – 1.0 particle μA. Thus, an enhanced target system has been developed with multiple large-area targets on a rotating wheel for cooling purposes. Nine arc-shaped large-area targets are fastened to the periphery of a 35.6-cm diameter rotating wheel. The speed of wheel rotation is variable but typically is 5 - 10 Hz during a BGS experiment.

The sets of ^{208}Pb and ^{209}Bi targets used in the course of this work were fabricated at the GSI target laboratory and at the target fabrication lab at LBNL. The targets consist of 460 μg/cm^2 ^{208}Pb or 440 μg/cm^2 ^{209}Bi metal evaporated onto a 35 μg/cm^2 carbon backing. A 5-10 μg/cm^2 layer of carbon is applied to the front to prevent loss of target material to sputtering and to enhance radiative cooling. Calculations of energy loss through the carbon window, target backing, and target material are done with the use of the program SRIM-2003 [53]. An image of the ^{209}Bi target wheel used in these studies is presented in Figure 2.1. These targets are thick enough to enable relatively fast measurements of cross sections, yet thin enough to allow the products of interest to recoil out of the target and into the volume of the BGS.

2.1.2 Rutherford Detectors

Unreacted beam particles scattered from the targets are detected by two *p-i-n* diodes and used to monitor the beam intensity. These detectors are installed at a 27.2 degree azimuthal angle to the beamline at a distance of 292 mm from the target. Perforated screens are installed upstream of these detectors to shield them from excess radiation damage. The screening factor of 1398 ± 70 was measured by Peterson [54, 55], which is the ratio of transmitted particles versus total incident particles. This factor is important in calculating accurate cross sections, as will be examined later in Section 2.2.2.1.

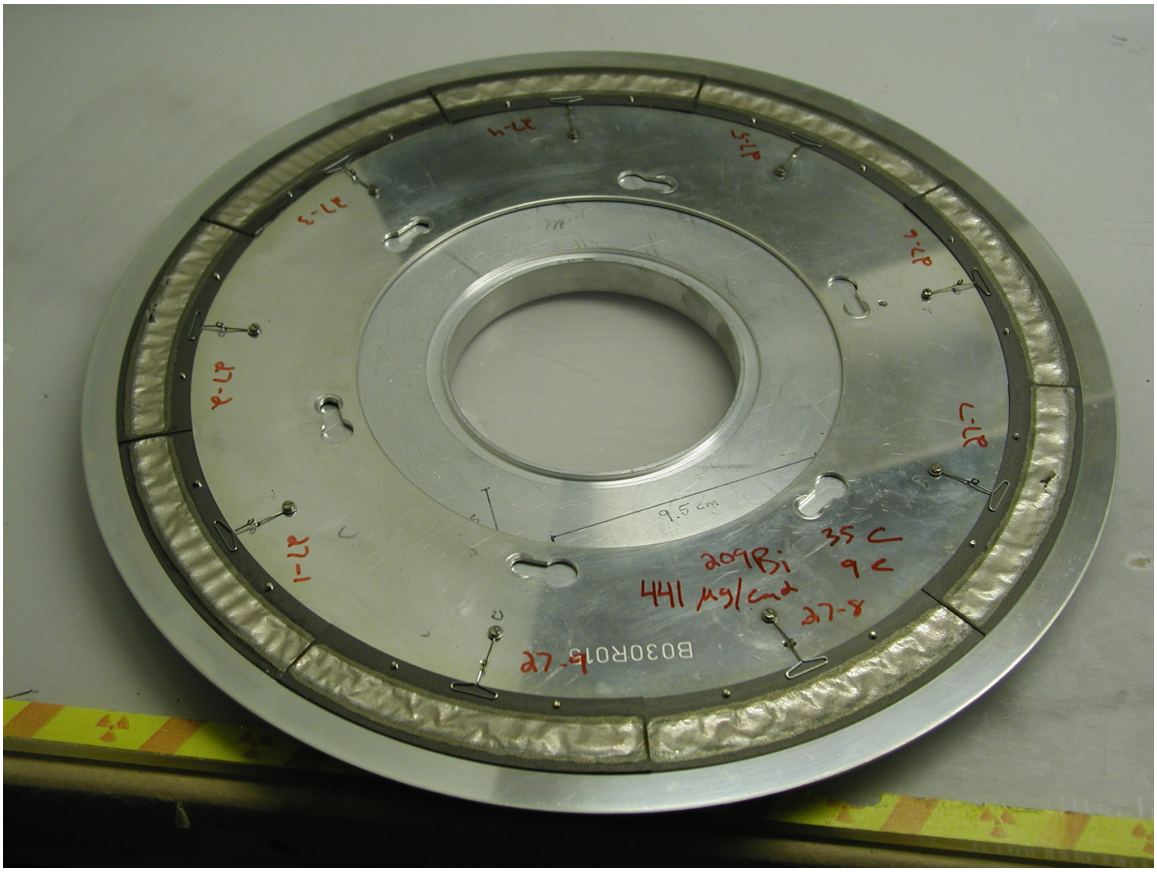

Figure 2.1: ^{209}Bi target wheel used in experiments with BGS. Individual targets are mounted on the periphery of the wheel, seen as textured strips. Numbers indicate individual target number (e.g.: 27-1) and target set properties.

2.1.3 The Berkeley Gas-Filled Separator

The use of magnetic rigidity and velocity separators for the detection of TAN elements has allowed researchers to study isotopes with short half-lives that could not be studied via chemical separation. The vast majority of material entering a separator is undesired, and the probability for a nuclear reaction producing a TAN is very small compared to the probability for other reactions to occur. Activity from transfer reactions, reactions in the beam stop, elastically-scattered target atoms, and unreacted beam all must

be separated prior to reaching the detector. These separators enable us to eliminate a substantial portion of these unwanted background activities that would otherwise interfere with identification of TAN elements and their decay products.

The BGS is a magnetic rigidity separator operating on a few basic principles of physics. First, the total momentum transfer in these CN reactions ensures that all products are ejected in a forward direction and into the separator volume. Second, the behavior of a charged particle in a magnetic field is well-characterized by the Lorentz force:

$$\vec{F} = q(\vec{v} \times \vec{B}) \qquad \text{Equation 2.1}$$

where q is the charge of the particle, v is its velocity vector, and B is the magnetic field vector. The scalar version ($F = qvB$) must be set equal to the centripetal force:

$$F = \frac{mv^2}{\rho} \qquad \text{Equation 2.2}$$

where m is the particle's mass, v its velocity, and ρ the radius of curvature of the particle's path. Combining these two equations of force yields the equation for magnetic rigidity:

$$B\rho = \frac{mv}{q} \qquad \text{Equation 2.3}$$

The quantity $B\rho$ determines what products will be guided through the separator to the focal plane detector and is ultimately the final goal of these calculations. Some of the quantities in this expression are straightforward to determine, others are not. The magnetic field B is a more complex value to calculate and will be discussed shortly. ρ is a fixed quantity, determined by the design of the BGS. m is the mass number of interest, already known. The velocity v is determined by the reaction kinematics and the beam

energy used. The charge q is not a straightforward calculation and will be covered shortly.

2.1.3.1 Estimating $B\rho$

As the evaporation residue (EVR) formed in the CN reaction recoils out of the target and into the BGS, it immediately encounters the helium fill gas. The EVR undergoes many charge-equilibrating collisions with the He gas, producing a distribution of charge states with a defined mean. Estimating this mean charge state is one of the challenges in preparing for an experiment.

Previous studies (see [56] for a review) indicate that the average charge state is proportional to $vZ^{1/3}$, where Z is the atomic number of the EVR in question. The velocity is commonly expressed in units of v_o, or the Bohr velocity (2.19 x 10^6 m/s). Much work has been done on this topic, and the most recent advancements involve a sinusoidal correction by K. E. Gregorich [57] to previous work by Ghiorso [58]. Gregorich devised an enhanced fit to the data presented in Ghiorso's work, incorporating this sinusoidal component that accounts for the electrons lost across an entire row of the periodic table. This formula is presented below, and is what was used to calculate the average charge state q in this work:

$$\bar{q} = px + r + s\sin\left\{\frac{2\pi}{32}[Z - (px + r) - t]\right\} \qquad \text{Equation 2.4}$$

where $x = (v/v_o)Z^{1/3}$, $p = 0.641$, $r = -0.235$, $s = 0.517$, and $t = 74.6$.

When the average charge state has been calculated, this value q is used to calculate the magnetic rigidity. Now that all variables on the right side of Equation 2.3 are known, we may solve for $B\rho$. After determining the desired magnetic rigidity, we use

the following set of relations to determine the appropriate currents for the individual BGS magnets (the BGS magnets themselves will be discussed in the next section):

$$I\mathrm{Q1} = 765 B\rho \frac{A}{T \cdot m} \qquad \text{Equation 2.5(a)}$$

$$I\mathrm{M1} = [\frac{B\rho}{0.002467 + 0.002016R}]\frac{A}{T \cdot m} \qquad \text{Equation 2.5(b)}$$

$$I\mathrm{M2} = [\frac{B\rho}{\frac{0.002467}{R} + 0.002016}]\frac{A}{T \cdot m} \qquad \text{Equation 2.5(c)}$$

Here, *R* represents the ratio of magnets M2/M1, a value of 1.69, which was experimentally determined to be the optimal value for EVR transmission through the BGS to the focal plane detector. (The focal plane detector is discussed in Section 2.1.4.2.)

2.1.3.2 The BGS Magnets

The BGS is comprised of three magnets: a vertically focusing quadrupole, a gradient-field dipole, and a flat-field dipole. The quadrupole magnet pushes the cone-like shape of the product distribution to one more horizontal in alignment. This results in the BGS having a large angular acceptance of 45 msr, compared to 15 msr of other separators in use. The gradient-field dipole magnet serves to steer out a large portion of the undesirable products and beam due to their differing magnetic rigidities. The flat-field dipole continues to guide those products possessing the magnetic rigidity of interest through to the focal plane detector, improves the horizontal focus and steers the

remaining undesirables to the Ta beam stop. A graphic of the BGS and its other components such as the target chamber is depicted in Figure 2.2.

The 70-degree bend angle of the BGS allows a high separation of EVRs from the unreacted beam and transfer products on the order of 10^9 or greater. Suppression of the full-energy beam is on the order of 10^{17}-10^{18}. The trade-off of having a large bend angle is that there is correspondingly a large dispersion of products. Changing the magnetic rigidity by 1% changes the horizontal alignment of the focal plane image by 2 cm, a large amount. We compensate for this large image by the use of a wide focal plane detector.

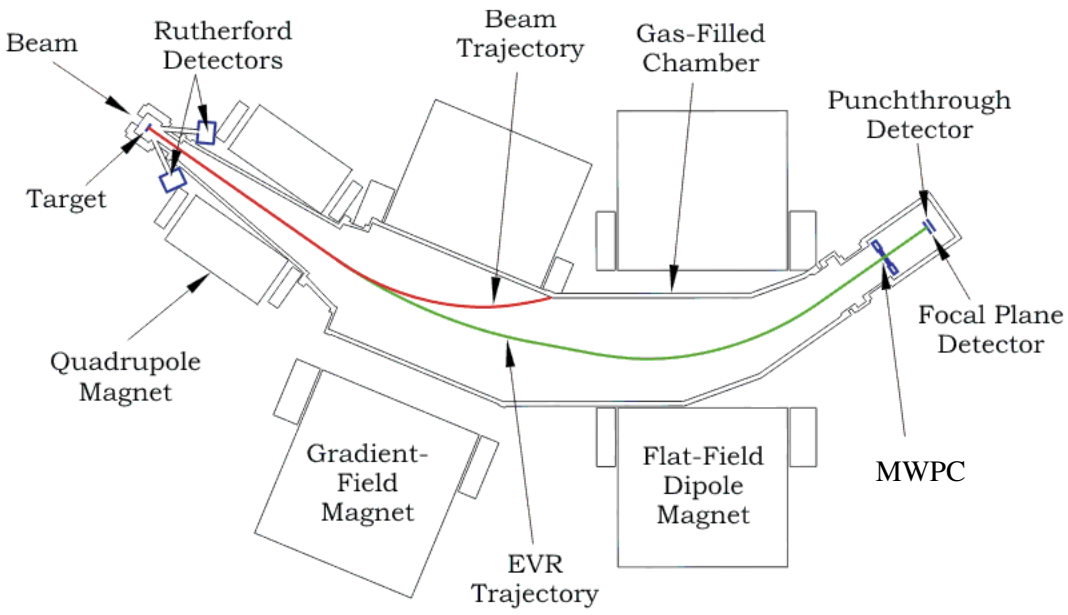

Figure 2.2: A schematic diagram of the Berkeley Gas-Filled Separator (BGS) and its components. See text for detailed information.

2.1.4 Detector Array

The work presented in this dissertation made use of two detectors installed in the BGS detector box, a gas-filled multi-wire proportional counter (MWPC), and the Si-strip focal plane detector (FPD). Each detector serves an important purpose during an experiment, and the use of the two in conjunction is particularly powerful.

2.1.4.1 Multi-Wire Proportional Counter

After the EVRs traverse the 4.6-meter path length of the BGS, they encounter the first of two detectors: the MWPC. The MWPC is modeled after those detailed in Figure 3 in [59], and can be seen installed in profile in Figure 2.3. This detector consists of two exterior mylar windows that seal in isobutane gas, two wire grids which act as anodes behind the mylar, and a center cathode plane made of metalized polyester foil. The bias is determined after the experiment has begun (typically 400-500 V). When an EVR passes through this detector, the gas particles along the EVR's path become ionized and the resulting ions and electrons are accelerated by the potential. A cascade of charge multiplication occurs and current flows through the device. The charge is collected and the signal is fed to the data acquisition system. The registration of a signal in the MWPC also initiates the start of a time recording in the time to amplitude converter (TAC). The time interval stops when a signal in the FPD is recorded. Signals in the MWPC are primarily used to discriminate implantation-like events such as EVRs from decay-like events such as alpha decays or fissions. This is helpful in data analysis, where events in the FPD which have energy signals like an alpha decay are ruled out as real alpha decays because of a MWPC or TAC signal in the data readout.

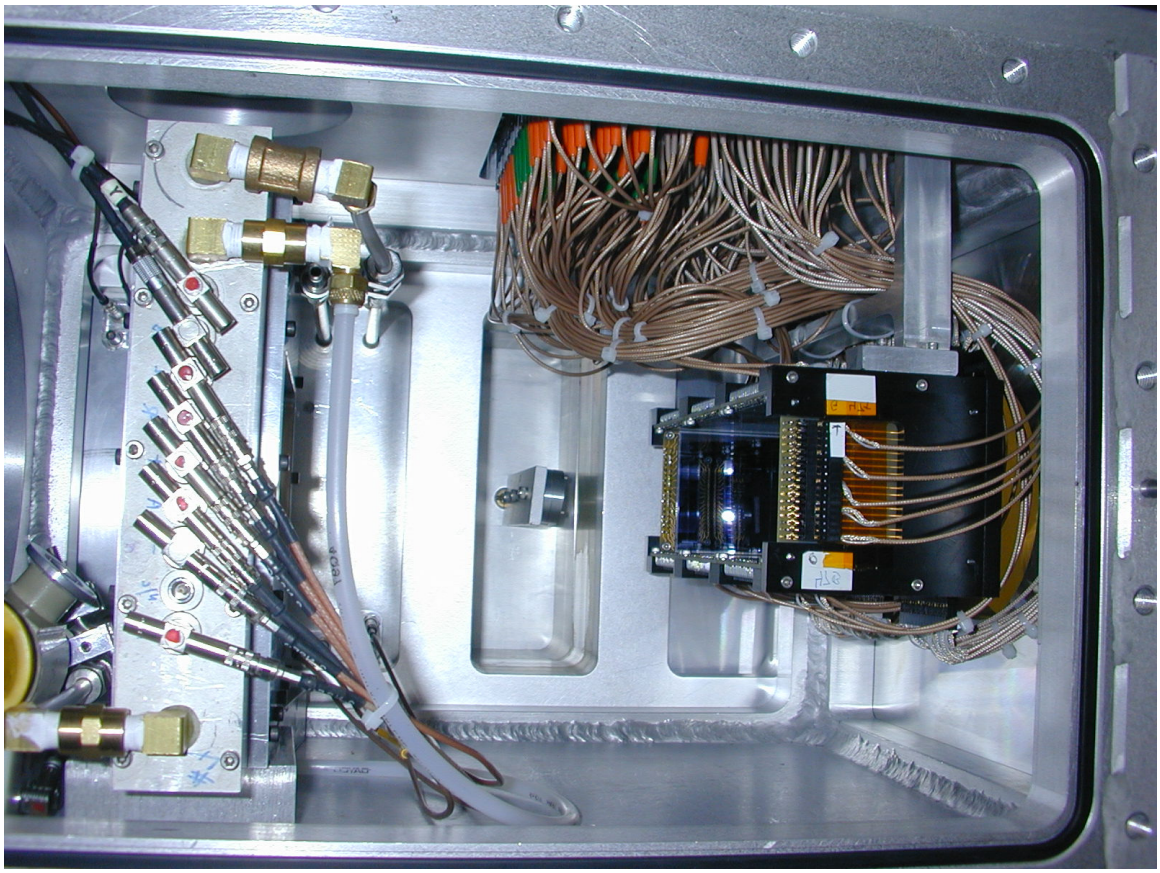

Figure 2.3: BGS MWPC (left) and FPD (right) installed in the detector enclosure. Reaction products proceed from left to right.

2.1.4.2 Focal Plane Detector

The main detector used in all BGS physics experiments is the FPD, depicted in Figure 2.4. This detector is constructed from 58 x 58 mm silicon strip detector cards, each with sixteen strips. The overall geometry of the detector is that of a five-sided box to increase the probability of detecting charged particles emitted in a forward direction. The main segment is situated at the focal plane of the BGS, where three cards totaling 48 strips are located. These cards are wired at the top and bottom of each strip, so time, energy, and position information may be obtained. The horizontal position is determined

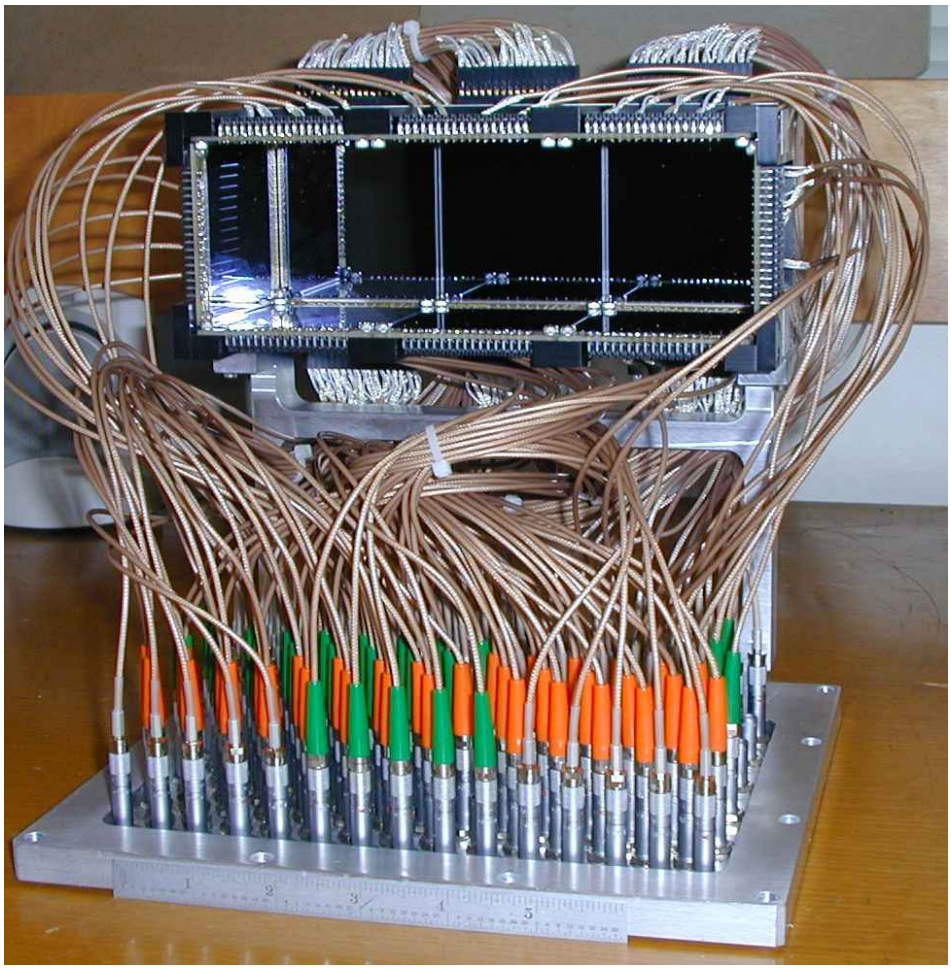

Figure 2.4: BGS focal plane detector array, sitting on its mounting plate. The primary detectors are located across the back of the array. The detectors forming the sides of the box are the upstream detectors. The punchthrough detectors are situated behind the main focal plane chips and are not visible in this image. The scale of the ruler (in front of mounting plate) is in inches.

by the strip number, and the vertical position is determined by resistive charge division.

The charge signals obtained from the top and bottom are treated as follows:

$$\text{absolute position} \cong \left(\frac{Q_t - Q_b}{Q_t + Q_b}\right) 32.2 \text{ mm} \qquad \text{Equation 2.6}$$

The position uncertainty of the events occurring in the BGS FPD has an inverse relationship to the energy (E) deposited and is calculated in a straightforward way [37]:

$$\sigma_{pos} = 2800E^{-1} \text{ keV·mm} \qquad \text{Equation 2.7}$$

There is an additional uncertainty of 1.5 mm added to this calculated value if the signal is from a high-gain amplifier. (Electronics will be discussed further in Section 2.1.5.)

The sides of this five-sided detector box are made of the same type of strip detector, with three cards each on the top and bottom, and one card on each side. These cards are time- and energy- sensitive as well, but instead of the strips being individually wired on the top and bottom these side, or "upstream," detectors are wired in clusters of four strips. This results in the upstream detectors not being position-sensitive. A second TAC signal similar to the MWPC-FPD signal is registered as a FPD-upstream detector signal, further validating upstream data signals in the data analysis process.

In addition, another set of three detector cards is placed immediately behind the main focal plane detector cards to detect light ionizing particles such as protons or scattered beam off of the He fill gas. These are wired similarly to the upstream detectors and they are not position-sensitive. This set of detectors is called the "punchthrough" detectors and serve as an additional veto method. We know that none of the TAN EVRs or their emitted particles could penetrate the detector cards, so any FPD signal coincident with a punchthrough signal is disregarded as a valid decay event.

2.1.5 Electronics and Data Acquisition System

The signals acquired by the BGS detector system are processed in a straightforward way. The component electronics include pre-amplifiers, amplifiers, constant fraction discriminators (CFDs) and analog-to-digital converters (ADCs). Prior to any experiment, noise thresholds are set on the CFDs and ADCs. Both the MWPC and

FPD detectors have a high voltage bias, and signals from each detector first proceed to a pre-amplifier.

Signals from the MWPC then travel to a standard amplifier, and a fast-out signal is sent to a CFD. If the signal is above threshold it continues on to start the TAC clock. The slow-out signal of the MWPC goes to an ADC (threshold conditions apply), then to the data acquisition system (DAQ).

Signals from the FPD proceed in a similar fashion, passing to a pre-amplifier and an amplifier, where there is a fast-out signal, a slow high-gain signal, and a slow low-gain signal. The fast-out signal passes to a CFD, and if above threshold, stops the MWPC-FPD TAC clock, and trigger the ADCs. The high-gain slow signal (typically for EVRs or fission decays) and the low-gain slow signal (typically for alpha decays) from the amplifier travel to ADCs. There, the above-threshold signals are passed on to the DAQ.

The DAQ is comprised of a few key components. The RIO2 computer runs the Multi-Branch System (MBS) developed by Essel *et al.* at GSI [8, 9], which utilizes the LynxOS operating system. LynxOS was chosen because it is a real-time system, minimizing delay to ~12 μs. MBS controls writing of data to disk, readout of scalars, user input commands, and DAQ interrupts. User-supplied programs handle the data readout, event building, and online data analysis. During an experiment, correlation search parameters can be specified, and if a proper match is found within the predetermined energy and time gates, the events of interest are displayed on-screen and a fast beam-shutoff may be employed. This fast shutoff (enabled within approximately 150 μs) is useful so that subsequent decays may be searched for in a low background environment.

2.2 Data Analysis Methods

Many steps are needed to transform the raw data collected using the BGS and its components into finished data in the form of cross sections, excitation functions, and various decay properties. This section of the chapter is dedicated to explaining those processes in more detail.

2.2.1 α-Energy Calibration

α-energy calibrations are very important to determining the proper energies detected, which in turn can affect event or decay chain assignments. Presented here is a brief description of how two types of energy calibrations, the external and internal, are achieved.

2.2.1.1 External Calibration

The name "external" calibration means that the particles detected in the FPD are from a source external to the detector itself. This source consists of four alpha-decaying isotopes: ^{148}Gd, ^{239}Pu, ^{241}Am, and ^{244}Cm. The alpha particle energies, half-lives, and alpha line intensities are presented in Table 2.1 with data from [60]. A sample spectrum is depicted in Figure 2.5. The source is mounted on a sliding arm in the BGS detector box that allows it to be easily inserted or retracted without opening the box itself.

These calibrations are typically performed immediately before and after the experiment. Occasionally the source is inserted during "down-time" in the experiment to check that the energy calibration has not shifted. Once a sufficient amount of data has been collected, the files are run through a low-energy calibration program written by

Nuclide	Half-life (years)	Alpha Particle Energy (MeV) [60]	Intensity of Alpha Peak	Weighted Average of Alpha Particle Energy (MeV)
^{148}Gd	74.6	3.183	100%	3.183
^{239}Pu	24,110	5.144	73.3%	5.152
^{241}Am	432.2	5.486	84.5%	5.482
^{244}Cm	18.1	5.805	76.4%	5.798

Table 2.1: Details of the four-peak alpha source for external FPD calibration. Weighted average energies incorporate fractional lower-intensity peaks and are energies used in low-energy α calibration program.

K. E. Gregorich. This program determines both the energy and position calibration of the events by first creating a top channel (T) vs. bottom channel (B) spectrum. Simply stated, a (T+B) spectrum is integrated over (T-B)/(T+B), and it is assumed the vertical center occurs where the integral reaches half its maximum value. In the end, the relations $E_t = m_t(T-a_t)$ and $E_b = m_b(T-a_b)$ are generated where m represents the slope and a represents the channel intercepts. Gregorich's code conveniently displays the calibration output in a C code cut-and-paste format.

Four-point alpha source spectra as in Figure 2.5 are also useful for determining the energy resolution of the FPD. The data are first processed through the analysis code, and the energies are left uncorrected for alpha decay recoil. The peaks are then fit with Gaussians and the FWHM is determined. The standard deviation (σ) is obtained from this spectrum.

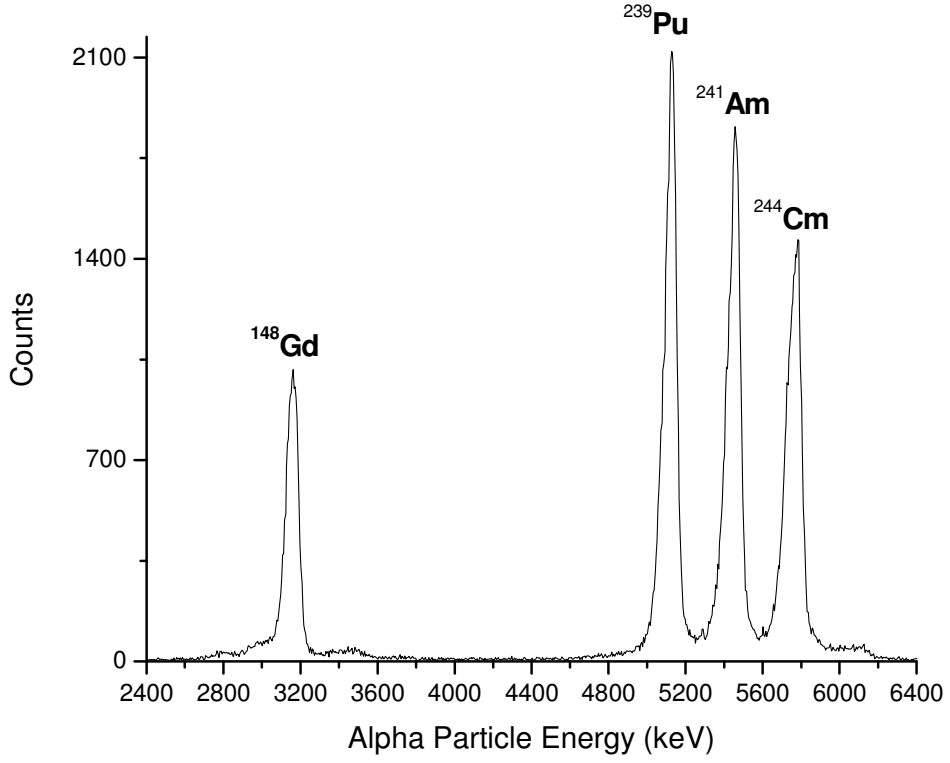

Figure 2.5: Sample spectrum from the four-peak alpha source containing ^{148}Gd, ^{239}Pu, ^{241}Am, and ^{244}Cm.

2.2.1.2 Internal Calibration

Calibrations using implanted EVRs in the FPD are important as well. These can give us information about the energy of the implanted EVRs and their corresponding pulse-height defects [61]. Additionally, data about the subsequent alpha particle energies without the effect of the FPD's dead layer are gained by using implanted activity. In the work presented in this dissertation, the majority of times there was not an adequate combination of stationary target and projectile which would produce desirable short-lived alpha activities. When necessary, internal calibration reactions from different

experiments were used to determine the uncertainty in the external to internal calibrations by fitting Gaussian functions to alpha spectra similar to the method described at the end of Section 2.2.1.1.

2.2.1.3 High-Energy Calibration

Because in a TAN experiment we measure EVRs and fission events in addition to alpha decays, a high-energy calibration is also needed. This is achieved in a similar fashion to the low energy calibration, but actual experimental data are used to determine the calibration. Events between 6 – 20 MeV from the top or bottom of a strip have signals in both the high-gain and low-gain ADCs. Using the known energy from the high-gain branch determined from the low-energy calibration, a linear regression from a plot of energy vs. channel number in the low gain branch is made.

2.2.2 The Data Analysis Code

A computer code written by K. E. Gregorich in C language was used to sort and analyze the data files in this work, and was instrumental to its success. This code is highly flexible and can be modified for various uses. It is with this code that energy gates for the EVRs, parent alpha particle energies, daughter alpha particle energies, and fission energies are defined. Time windows for event acceptance, thresholds for the MWPC as well as the FPD strips can be defined. Various functions can be simply turned on or off, such as enabling/disabling reconstruction of alpha events from upstream detectors, printing detailed information about fission events, or reporting when a beam shutoff has been enabled.

The conditions of the individual decay search are input, the event numbers to look within are defined along with other conditions, and the sorting of data proceeds in a straightforward manner. EVR-α, EVR-α-α, EVR-SF, and other decay chains of interest are identified in a first-round sort, and then the events comprising the decay chains are examined in more detail. Searches beyond these initial events are often conducted to identify decays with longer lifetimes. The searches may include the entire FPD or a single strip. Individual strips may be turned off if necessary. Various spectra are generated and the output is saved as a text file for further inspection.

2.2.3 Calculation of Cross Sections

The measureable quantity of primary interest in this work is the 1*n* (and sometimes 2*n*) cross section. In order to calculate cross sections, there are a few values we must solve for first. When these values have been determined, we may then calculate the resulting cross sections, and from these cross sections excitation functions are constructed. The methods of completing these steps are described in more detail in the following sections.

2.2.3.1 Integrated Dose

Looking back to Equation 1.3 in Chapter 1, one of the variables is *I*, the incident particle flux. In order to calculate this quantity, we must first relate the Rutherford scattered beam detected (discussed in Section 2.1.2) to the beam intensity. Because our detectors are at a fixed angle θ, we require the equation for the differential Rutherford scattering cross section [62]:

$$\frac{d\sigma_{Ruth}}{d\omega} = \left[\frac{e^2 Z_1 Z_2}{4\pi\varepsilon_o (2E_{lab})}\right]^2 \frac{1}{\sin^4\theta} \frac{\left[(\cos\theta) + \sqrt{1-\left(\frac{m_1}{m_2}\right)^2 \sin^2\theta}\right]^2}{\sqrt{1-\left(\frac{m_1}{m_2}\right)^2 \sin^2\theta}} \quad \text{Equation 2.8}$$

where Z_1, m_1 and Z_2, m_2 are the atomic numbers and masses of the projectile and target, respectively, E_{lab} is the lab-frame projectile energy, and e^2 and e_o are the square of the electric charge and permittivity constants, respectively. (In this work we add the cosine term because m_1 is always less than m_2.)

The remaining required variables are determined as follows: The number of Rutherford scattered particles detected (N_{Ruth}) is determined by integrating over the appropriate region of the Rutherford spectra collected during the experiment. The mean number of detected particles from the two Rutherford detectors is used in the calculations. The fraction of 4π subtended by the Rutherford detector collimators is $2.1 \cdot 10^{-4}$. The number of target atoms is determined by the following relation:

$$N_t = \frac{\rho_A N_{Avo}}{m_t} \quad \text{Equation 2.9}$$

where ρ_A is the areal density of the target used, N_{Avo} is Avogadro's number, and m_t is the mass of the target. The dose is then calculated by combining the results from Equations 2.8 and 2.9, our screening factor for the Rutherford detectors, the mean number of Rutherford scattered particles, and the solid angle subtended by the Rutherford detector collimators to yield:

$$\text{dose} = \frac{\overline{N}_{Ruth} \cdot 1398}{\Omega\left(\frac{d\sigma_{Ruth}}{d\omega}\right) N_t} \quad \text{Equation 2.10}$$

A typical dose for a 2-3 day experiment is on the order of $10^{16} – 10^{17}$ ions at a beam intensity of approximately 0.25 particle-μA.

2.2.3.2 Calculation of Decay Chain Detection Efficiencies

Because many of the decay chains of interest in this work are difficult to conclusively assign, an efficiency factor accounting for the reduced number of assigned chains is included in each cross section calculation.

Chain detection efficiencies are calculated by first determining the decay and detection paths that result in *Z* and *A* identification of the chain and their corresponding lengths. Though determined on an individual basis for each EVR of interest, typically this includes an EVR followed by two full-energy or reconstructed alpha decays, or an EVR followed by a full-energy alpha decay, escape alpha decay, and an additional full-energy decay. Once those paths and lengths have been assigned, each path's efficiency is the product of each constituent's branching ratio and probability of observation.

The probability of observation for SF decays is assigned a value of 1.0. From Monte Carlo simulations of "alpha decays" from implanted "events" in the BGS focal plane detector, we know that the probabilities of observing alpha decays are: Full-energy event = 0.541, reconstructed event = 0.224, "visible" escape = 0.082, and "missing" escape = 0.153. Full-energy events are those that have a full signal registered in the focal plane detector. Reconstructed events are those events that have an alpha particle or fission fragment exit the focal plane detector at such an angle that the particle would collide with an upstream detector. The sum of the signal in the focal plane and the signal in the upstream detector is used. An escape event is one where the alpha particle or

fission fragment exits the focal plane detector and misses the upstream detector array, thus leaving a small signal behind that may or may not be over the detection threshold ("visible" and "missing" escapes, respectively).

Once all the paths have had their individual efficiencies calculated, they are summed and a total alpha chain detection efficiency results. To check this method for validity, one "stops" each chain at the same particular stage (isotope) and calculates the efficiency value of every known decay path, whether or not it is an acceptable one for that parent isotope. The sum of all paths ending at the same stage should equal unity. We have calculated alpha chain detection efficiency factors for three different situations: For the 1*n* product when production of the 2*n* product is not possible, for the 1*n* product when production of the 2*n* product is possible, and for the 2*n* product only. Once these chain detection efficiencies have been calculated, they are included as part of the cross section calculation.

2.2.3.3 The Cross Section

After having determined the number of events of interest during the experiment, and calculated the associated chain detection efficiency and beam dose to the target, a cross section can be calculated using a more detailed version of Equation 1.3:

$$\sigma = \frac{N_{obs}\Omega\left(\frac{d\sigma_{Ruth}}{d\omega}\right)}{\varepsilon_{BGS}\varepsilon_{chain}\overline{N}_{Ruth}1398} \qquad \text{Equation 2.10}$$

where most terms originate from Equations 2.8 and 2.9, ε_{chain} is the decay chain detection efficiency factor, and ε_{BGS} is the total efficiency for the BGS. The BGS efficiency is

calculated using a Monte Carlo simulation of EVR transport through the separator which accounts for reaction kinematics, magnet optics, etc. For reactions in this dissertation this efficiency factor is a value between 0.63 – 0.75, and individual values may be found in Table 2.2. For the reactions producing ^{258}Db and ^{262}Bh, the simulations assumed an elliptical collimator with a large vertical target size of 8 mm. For the reaction producing ^{266}Mt, a new collimator was in place, with a smaller vertical dimension of 6 mm. For all simulations it was assumed the target was evenly illuminated by the beam.

Reaction	ε_{BGS}
^{208}Pb(^{51}V,*n*)^{258}Db	0.63 ± 0.02
^{209}Bi(^{54}Cr,*n*)^{262}Bh	0.64 ± 0.02
^{208}Pb(^{55}Mn,*n*)^{262}Bh	0.67 ± 0.02
^{208}Pb(^{59}Co,*n*)^{266}Mt	0.75 ± 0.02

Table 2.2: Transport efficiencies of EVRs through the BGS, calculated with a Monte Carlo simulation. See text for details.

2.2.3.4 Cross Section Uncertainty

When reporting any measurement, it is important to address the associated uncertainty. In the case of rare, statistically independent events like TAN EVRs, this is best described by the Poisson distribution:

$$p(n \mid \mu) = \frac{\mu^n}{n!} \cdot e^{-\mu} \qquad \text{Equation 2.11}$$

where n represents the number of events observed, and μ is the number of events based on the true cross section. For an observed N_{obs} counts (n in Equation 2.11), the following

relations [63] are used to determine the upper and lower limits (Equations 2.12 (a) and (b), respectively) for a defined confidence interval *CI*:

$$\sum_{n=0}^{N_{obs}} \frac{N_{obs}^{\ n}}{n!} e^{-N_{obs}} = \frac{1-CI}{2} \qquad \text{Equation 2.12 (a)}$$

$$1 - \sum_{n=0}^{N_{obs}-1} \frac{N_{obs}^{\ n}}{n!} e^{-N_{obs}} = \frac{1-CI}{2} \qquad \text{Equation 2.12 (b)}$$

All cross sections reported in this work use the 68% confidence interval. In the case of small numbers of events such as these data presented in this work, this method more accurately reproduces error limits than the use of symmetric error bars. A similar treatment of half-life uncertainty may be found in Section 2.2.6.

2.2.4 Calculation of Expected Random Decays

In any heavy element production experiment such as those described in this dissertation, only a few events of interest are generated in comparison to transfer products, scattered target atoms, etc. Though physical separators such as the BGS aid in the removal of these unwanted products, some remain which could interfere with the interpretation of data. There is also the contribution of noise from electronics, background signals from previous implantations in the detector, and similar non-reaction related sources of undesirable signals. The possibility that a combination of these aforementioned interfering signals could be interpreted as a real decay chain exists, and therefore it is important that we look into the probability and expected number of randomly correlated decay events for each experiment. (A more detailed discussion may be found in the Ph.D. dissertation of C. M. Folden III [64].)

2.2.4.1 Background

In pursuing this question, we must keep in mind the requirements that our real decay chains must possess in order to be considered valid. The constituents of the chain must be correlated within a certain amount of time. Each nuclide of interest has an associated half-life, and in the data we naturally observe a distribution of lifetimes. A maximum time of event consideration, Δt_{max}, is chosen so that we constrain the time interval in which we allow these decays to be valid. This value is not made with respect to any one observed lifetime so that the results of these calculations are not influenced by the data in question. This time interval is typically a multiple of five times the half-life of the longest-lived nuclide in an expected decay chain.

Each α-decay of interest possesses an individual decay energy signature, and the energies of interest must be reasonably matched within the known energy resolution. Implantation events preceding decays also have a reasonable expected range of energies, based on the kinematics of the reaction and the energy loss through the BGS, MWPC, and the pulse-height defect for detection of heavy ions [61] in Si-detectors. These quantities are calculated before the experiment is carried out, using the SRIM program [53] and a similar program designed by K. E. Gregorich [65] to model energy loss of very heavy charged EVRs in helium gas.

These implantations and subsequent decays must also be detected within a certain position in the detector, both in the horizontal direction determined by the individual strip it has been implanted in, and in the position-sensitive vertical direction of that single strip. We define the detector to have a number of pixels, denoted as N_{pix}, with a certain acceptable pixel size within which events may decay.

2.2.4.2 Calculation Method

During the run of a BGS experiment, the focal plane detector array records information about implantation events (EVRs) and decays that occur. Each valid decay chain is required to begin with an EVR signal (with no punchthrough or upstream detector signal), and additional decay signals follow. We can estimate rates of these EVRs and alpha decays for each bombarding energy from spectra after the experiment is complete. In the experiments in this dissertation, EVR-like events are required to have a signal in the MWPC detector as well as a focal plane signal, and alpha-like events are required to have a focal plane signal but no MWPC or punchthrough detector signal. By integrating these spectra over a reasonable specified energy range and determining the duration of time these events may have taken place, we may calculate the number of these type of events and rate at which each type of event occurred in the focal plane. The nomenclature N_{EVR} and R_α for the number of EVR-like events and rate of alpha-like events, respectively will be used.

We then consider the number of expected alpha decays per pixel in the detector, R_α/N_{pix}. First, one must determine the number of pixels in the detector by dividing the total position-sensitive area of the detector by our defined pixel size. In this work we have chosen the pixel size to be a generous 1.5 mm within a single strip. Next, we multiply this quantity by the time interval of maximum event consideration, or Δt_{max}. One may now calculate the expected number of alpha decays, or m_α, for a single pixel in the detector:

$$m_\alpha = \frac{R_\alpha \Delta t_{max}}{N_{pix}} \qquad \text{Equation. 2.13}$$

We also define an integer value for the number of alpha decays correlated in one decay chain as n_α. Typically this number will be greater than one, because with events containing only one alpha decay correlated to an EVR, it would be difficult to positively make an assignment of Z and A. Using these quantities, one may then calculate the Poisson probability of observing n_α events given m_α expected events:

$$P_{Poisson}(m_\alpha, n_\alpha) = \frac{m_\alpha{}^{n_\alpha}}{n_\alpha!} e^{-m_\alpha} \qquad \text{Equation. 2.14}$$

By multiplying the probability given as a result of Equation 2.12 by the number of EVR-like decays across the detector (N_{EVR}), we calculate the number of expected random correlations for a given bombarding energy. Variations on this calculation method are used to determine random correlations to escape alpha decays, and decay chains correlated to alpha-like events of a specific narrow energy range.

2.2.5 Maximum Likelihood Fitting of 1*n* Excitation Functions

The basic principle behind the maximum likelihood method allows a defined probability function and a fixed set of data to arrive at the "most likely" parameters of the function [66]. Modeling real data through the estimation of maximum likelihood offers a way of adjusting the free parameters of the model to provide an optimal fit [67].

2.2.5.1 Introduction

A maximum likelihood fit procedure similar in idea to the work of Gregorich [68], adapted for excitation functions by Dragojević [69], was used with the 1*n* data. This function utilizes a Gaussian function on the low-energy side of the excitation

function smoothly joined to an exponential function on the high-energy side. This combination of a Gaussian and exponential function simply yet accurately reproduces the known general shape of excitation functions. The fit incorporates weighting for numbers of events, cross sections, and also energy spread through the target, which correctly accounts for the variation in cross section over the target's energy thickness. The use of such fits allows us to obtain accurate values of cross sections and energies at the peak of the excitation function, instead of relying on discrete data points from which to draw conclusions.

2.2.5.2 Methodology

Because the excitation function is made of a Gaussian function smoothly joined to an exponential function, we must define the functions used:

$$\sigma = \sigma_{\max} e^{\lambda^2\omega^2/2} e^{-\lambda(E^*-c)}, E^* > \lambda\omega^2 + c \qquad \text{Equation 2.15(a)}$$

$$\sigma = \sigma_{\max} e^{-(E^*-c)^2/2\omega^2}, E^* \le \lambda\omega^2 + c \qquad \text{Equation 2.15(b)}$$

where σ_{max} is the amplitude of the Gaussian with width ω and centroid c. The joining point, $\lambda\omega^2 + c$ is determined by setting the two functions and their first derivatives equal with respect to E^*, and solving for the joining point. E^* represents the CN excitation energy in the center of the target, and $-\lambda$ is the exponential slope. By integrating σ over the energy width of the target, we may calculate the expected number of counts μ, expected at a given bombarding energy:

$$\mu_{\text{expected}}(L, E^*, E_w, \sigma_{\max}, \omega, c, \lambda) = \frac{L}{E_w} \int_{E^*-\frac{E_w}{2}}^{E^*+\frac{E_w}{2}} \sigma(\sigma_{\max}, \omega, c, \lambda, E) dE \qquad \text{Equation 2.16}$$

Here, L represents the one-event sensitivity (events/pb), and E_w represents the energy width of the targets. We then use the Poisson distribution to calculate the probability of observing n events when μ are expected at m energies:

$$L(\sigma_{\max}, \omega, c, \lambda) = \prod_{i=1}^{m} \frac{\mu^{n_i}}{n_i!} \cdot e^{-\mu} \qquad \text{Equation 2.17}$$

Taking the natural logarithm of this function changes it to a sum expression (exceeding the dimensions of this page). These functions were entered into a Mathcad program and the resulting fits were determined accordingly. The values of σ_{max} (the peak amplitude), ω (the Gaussian width), c (the peak centroid) and λ (the exponential slope) were allowed to vary within constraints. The parameters of primary interest in this work were σ_{max} and c, and will be discussed in the results sections Chapters 3 and 4.

When possible, the parameters w and λ were allowed to vary freely. On occasion, it was necessary to fix them at values of 1.349 and 0.183, respectively. These two values were obtained from a fit to the ^{208}Pb(^{48}Ti,xn)^{255}Rf reaction [69] which possesses high statistics and multiple bombarding energies with confidence that they are applicable in this work.

We acquire the fit curve from the following expression:

$$f(\sigma'_{\max}, \omega', c', \lambda') = \frac{\mu}{L} \qquad \text{Equation 2.18}$$

where the prime designation indicates the parameters of best fit have been obtained. The value of the goodness of fit is also displayed in the Mathcad program, and is used to not only compare different sets of fit parameters to determine the best fit, but it is used to quickly determine the uncertainty in the fit parameters.

2.2.5.3 Uncertainty in Fit Centroid and Amplitude

Though the values of the resulting amplitude and centroid from this fitting method are important, we also require an understanding of each value's uncertainty. This is achieved by defining σ_{max} and c to have a particular value and recording how the goodness of fit is affected. This is repeated until a distribution of values is obtained, and the results are graphed. This distribution is Gaussian in shape, and a standard Gaussian fit function is used to determine the width, which is then related to the standard deviation, σ (not to be confused with the cross section symbolism), and a symmetric uncertainty is obtained.

2.2.6 Half-life Calculation and Uncertainty

Calculation of the half-life proceeds by the well-known relations:

$$t_{1/2} = \frac{\ln 2}{\lambda}, \lambda = \frac{1}{\bar{\tau}} \qquad \text{Equation 2.19}$$

where λ represents the decay constant for the nuclide, which is inversely proportional to the mean lifetime, τ. Because the lifetimes used to calculate these half-lives are from rare events as described in Section 2.2.3.4, the uncertainty in the half-lives is calculated in a similar way [63]. A confidence interval (*CI*) is defined, and for all half-lives reported in this work is 68%. The relations for the upper and lower limits (Equations 2.20 (a) and (b), respectively) on the lifetimes are:

$$\int_{\bar{\tau}}^{\infty} \frac{n^{n+1}}{n!} \cdot \frac{\tau^{n-1}}{(\bar{\tau} \cdot 1.2)^n} \cdot e^{-n \cdot \frac{\tau}{\bar{\tau} \cdot 1.2}} dt = \frac{1+CI}{2} \qquad \text{Equation 2.20 (a)}$$

$$\int_{\bar{\tau}}^{\infty} \frac{n^{n+1}}{n!} \cdot \frac{\tau^{n-1}}{(\bar{\tau} \cdot 0.8)^n} \cdot e^{-n \cdot \frac{\tau}{\bar{\tau} \cdot 0.8}} dt = \frac{1-CI}{2} \qquad \text{Equation 2.20 (b)}$$

where n is the number of events contributing to the mean lifetime. The limits on the half-lives can be calculated by multiplying these upper and lower limits by ln 2.

Now that the various equipment and methods used to calculate the quantities of interest have been explored, we explore the data they have been applied to.

3. Experimental Results:

Production of Dubnium in the $^{208}Pb(^{51}V,xn)^{259-x}Db$ Reaction

3.1 Previous Work

3.1.1 Dubna Experiments

The first experiments to investigate the fission probabilities of isotopes of elements 103, 105, and 107 were undertaken by Oganessian (also spelled Oganesyan) *et al.* at the JINR in Dubna, Russia, in 1976 [70]. A discussion of the relevant element 105 results follows. Three separate reactions producing a compound nucleus of ^{259}Db were studied in this effort: ^{209}Bi(^{50}Ti,x*n*), ^{208}Pb(^{51}V,x*n*), and ^{205}Tl(^{54}Cr,x*n*). These studies were not sensitive to alpha decay, as they only used mica track detectors to record fission decays. Their beam impinged at a tangential angle on a rotating drum target, and fission fragments exiting the target left tracks in the mica. These mica detectors were etched and then visually examined under magnification to count the number of fission tracks deposited. The rotation speed of the drum was monitored and varied to span a wide range of half-lives. The beam intensity was determined by the activation of a small copper catcher foil installed on the drum. Post-irradiation, the gamma spectra were recorded with a Ge(Li) spectrometer. Experiments using the $^{54}Cr^{8+}$ beam also used the same method to control for co-resonant $^{27}Al^{4+}$ impurities.

Oganessian and coworkers began their pursuit of ^{258}Db with the ^{50}Ti + ^{209}Bi reaction, expecting the largest cross section from this target-projectile combination. A

spontaneously fissioning nuclide was observed with a half-life of $5.6^{+4.0}_{-1.8}$ s. The other selected reactions with ^{54}Cr and ^{51}V produced the same activity, and they concluded they had successfully produced the same compound nucleus three different ways. By compiling the results of the three reactions, they obtained a half-life of $5.0^{+1.7}_{-1.1}$ s for the spontaneous fission activity, and assigned it to the 2*n* evaporation product, ^{257}Db. We now know that this conclusion was not necessarily correct - they may have observed the production of either ^{257}Db or ^{258}Db.

A major issue with their work is that many of their conclusions are drawn from inference rather than direct observation of decays. The non-specific nature of the methods used allowed them to make many erroneous assertions about decay properties and half-lives. However, the IUPAC – IUPAP working group awarded this team of researchers the right to name element 105 as a result of their successful discovery of dubnium as ^{261}Db though a different reaction in earlier years [5].

3.1.2 GSI Experiments

In the attempt to produce the new element bohrium (Bh) in the ^{209}Bi(^{54}Cr,x*n*)$^{263-x}$Bh (x = 1, 2) reaction, Münzenberg *et al.* at GSI in Darmstadt, Germany, also discovered the new isotopes ^{258,257}Db and ^{254}Lr as its decay daughters and granddaughter [7]. (More information about ^{262}Bh can be found in Chapter 4 of this dissertation.) In an effort to observe ^{258}Db and ^{257}Db directly, they also studied the ^{209}Bi(^{50}Ti,x*n*) reaction , and the decay properties compared favorably to those of the daughter decay from Bh. They were able to make *Z* and *A* identification of these new isotopes from observation of decay chains through the known nuclides ^{250}Fm and ^{250}Md.

One year later, the same group at GSI attempted to produce the new element 109, meitnerium (Mt), via a very similar cold fusion-type reaction: ^{209}Bi(^{58}Fe,*n*)^{266}Mt [9]. They observed one correlated alpha decay chain at a ^{58}Fe energy of 5.15 MeV/u, and this chain passed through ^{262}Bh to ^{258}Db as well. The ^{258}Db underwent electron capture decay to ^{258}Rf that subsequently fissioned, and so ^{258}Db was not directly observed. However, the combined lifetimes of ^{258}Db and ^{258}Rf were consistent with those decays. More information about this experiment and consequent follow-up experiments can be found in Chapter 6 of this dissertation.

Additional experiments to study ^{258,257}Db and their daughters exclusively were completed by Heßberger *et al*. in 1985 [35] and 2001 [36]. The reaction ^{209}Bi(^{50}Ti,x*n*)$^{259-x}$Db (x = 1, 2) was used for these investigations. Improved data on the decay properties of these nuclides was gained, as well as information about the cross sections and excitation functions for the 1 and 2*n* exit channels.

^{258}Db is now known to decay by alpha particle emission with branching of $0.67^{+0.05}_{-0.09}$ and by electron capture with branching of $0.33^{+0.09}_{-0.05}$. The alpha decay energies observed were 9.01, 9.08, 9.17, and 9.29 MeV, and the resulting half-life of ^{258}Db is $4.4^{+0.9}_{-0.6}$ s. The maximum observed cross section from this study was 2.9 ± 0.3 nb, at a compound nucleus excitation energy of 16.5 MeV. Their later study reports a maximum 1*n* cross section of 4.3 ± 0.43 nb [36].

Though work in this dissertation is primarily concerned with the study of 1*n* reaction products, we also observed the 2*n* exit channel for reactions involving Db and Bh so we choose to remark on them as well. In Heßberger's studies of ^{209}Bi(^{50}Ti,x*n*)$^{259-x}$Db mentioned previously, the decay properties of the 2*n* de-excitation

product, ^{257}Db, were enriched also. Their 2001 work to explore more neutron-deficient isotopes of Db and Lr used the same reaction, and excitation functions of the 1, 2, and 3*n* exit channels were mapped [36]. From these most recent data, it was established that ^{257}Db possesses both a ground and metastable state. The ground state has a half-life of $1.5^{+0.19}_{-0.15}$ s, and decays by alpha particle emission with energies 9.074 and 8.967 MeV. The upper limit on the spontaneous fission decay branch is less than 0.06. ^{257}Db^{m} has similar decay properties: alpha particle emission with an energy of 9.163 MeV and a half-life of $0.76^{+0.15}_{-0.11}$ s. The maximum cross section for production of ^{257}Db was measured to be 2.4 ± 0.3 nb at a compound nucleus excitation energy of 22.3 MeV.

3.1.3 LBNL 2*n* Experiments

An experiment to study the ^{208}Pb(^{51}V,2*n*)^{257}Db reaction was done at LBNL with the BGS by J. B. Patin. The main goal of the study was to investigate the production of ^{257}Db to establish its usefulness for dubnium chemistry studies. A similar study using the ^{209}Bi(^{50}Ti,2*n*) reaction was done as well. These studies utilized one and two bombarding energies, respectively. Searches were made for correlated decay chains, and the results were consistent with the previously published data on ^{257}Db by Heßberger *et al*. [36]. No excitation functions were produced as a result of the few data points in each experiment. A comparison to predictions from the HIVAP code was made, and the code predicted a higher cross section as was the case with other cold fusion-type reactions studied by Patin. Results from these experiments were not published in the literature, but can be found in the Ph.D. dissertation of J. B. Patin [71].

3.1.4 LBNL ^{50}Ti + ^{209}Bi Experiments

Recently, Gates *et al.* [72] conducted an experiment to measure the ^{209}Bi(^{50}Ti,x*n*)$^{259-x}$Db reaction with the BGS at LBNL. Though this reaction had already been well-studied at GSI, studying it again was of interest so that a reaction with high statistics could be used to compare any systematic energy difference between the two laboratory's results. Five bombarding energies were used during the course of the experiment, and the decay properties appear to be in line with previous findings. The resulting excitation functions from the Gates study may be found in Section 3.5.1, along with a comparison to the GSI work.

3.1.5 Motivation for Additional Studies

Though Patin's study of the ^{51}V + ^{208}Pb reaction was successful, it did not yield information about the 1*n* exit channel. With a relatively high cross section - in the nanobarn range - expected for the 1*n* exit channel, we felt it reasonable to repeat this reaction at various energies to complete a 1*n* excitation function. Our goal was to gain information about the magnitude and peak location of the 1*n* excitation function, and compare it to the similar ^{50}Ti + ^{209}Bi reaction that was so thoroughly studied by GSI.

In addition, investigating the ^{51}V + ^{208}Pb reaction will contribute to the systematic study to investigate what role, if any, the entrance channel plays in compound nucleus formation. The pair of 1*n* reactions lowest in *Z* is: ^{50}Ti + ^{209}Bi, and ^{51}V + ^{208}Pb, producing ^{258}Db. By obtaining information about the ^{51}V + ^{208}Pb reaction, we complete work on the first pair in our study.

3.2 Experimental

The reaction to produce Db studied in this work was the ^{208}Pb(^{51}V,x*n*)$^{259-x}$Db (x = 1, 2) reaction, where six bombarding energies were run. The ideal energy for the evaporation of only one neutron for this reaction was calculated by using the "Optimum Energy Rule" from the "Fusion By Diffusion" model by Świątecki, Siwek-Wilzyńska, and Wilczyński [29, 30, 32]. This energy was determined to be 236.2 MeV in the center of the target and laboratory-frame of reference. It was found that this energy was not at the peak of the excitation function, and at a later time Świątecki determined that there is an additional energy offset of 1-3 MeV required to reach the maximum, determined by these and previous experimental data [33].

The BGS was operated in a standard configuration with MWPC detector in place upstream of the focal plane detector. The magnet currents for the BGS were tuned to first direct only products possessing a $B\rho$ of 2.133 T·m through to the Si-strip focal plane detector. Near the end of the experiment the magnet currents were increased by 2%, resulting in a $B\rho$ of 2.176 T·m, centering the event distribution on the focal plane detector.

Distinguishing decay chains of ^{258}Db from chains of ^{257}Db presented a challenge due to their similar alpha particle energies and lifetimes. Observation of the ^{254,253}Lr granddaughter's alpha decay or the electron capture (EC) decay and subsequent alpha decay of ^{254}No was essential to conclusively assign a decay chain to a particular mass number. For this reason, we have chosen to only assign events fitting the criteria listed in Table 3.1, and have calculated alpha chain detection efficiencies for both the 1 and 2*n* exit channel products by the method described in Section 2.2.3.2 to properly account for

Decay Chain	Accepted Decay Paths	Alpha Chain Detection Efficiency Factor
^{258}Db	^{258}Db–α, ^{254}Lr–α…	0.850
Production of ^{257}Db at this/these energy/energies unfavorable	^{258}Db–α, ^{254}Lr–EC, ^{254}No–α...	
	^{258}Db–EC, ^{258}Rf–SF	
	^{258}Db–EC, ^{258}Rf–α, ^{254}No–α…	
	^{258}Db–esc§, ^{254}Lr–α…	
	^{258}Db–missing esc, ^{254}Lr–α, ^{250}Md–EC, ^{250}Fm–α…	
	^{258}Db–α, ^{254}Lr–esc, ^{250}Md–EC, ^{250}Fm–α…	
	^{258}Db–esc, ^{254}Lr–EC, ^{254}No–α, ^{250}Fm–α…	
	^{258}Db–α, ^{254}Lr–EC, ^{254}No–esc, ^{250}Fm–α…	
	^{258}Db–EC, ^{258}Rf–esc§, ^{254}No–α, ^{250}Fm–α…	
	^{258}Db–EC, ^{258}Rf–α, ^{254}No–esc§, ^{250}Fm–α…	
	^{258}Db–α, ^{254}Lr–esc, ^{250}Fm–α…	
	^{258}Db–esc, ^{254}Lr–α, ^{250}Fm–α…	
^{258}Db	^{258}Db–α, ^{254}Lr–α…	0.623
Production of ^{257}Db at this/these energy/energies favorable	^{258}Db–α, ^{254}Lr–EC, ^{254}No–α...	
	^{258}Db–EC, ^{258}Rf–α, ^{254}No–α…	
	^{258}Db–esc§, ^{254}Lr–α…	
	^{258}Db–missing esc, ^{254}Lr–α, ^{250}Md–EC, ^{250}Fm–α…	
	^{258}Db–α, ^{254}Lr–esc, ^{250}Md–EC, ^{250}Fm–α…	
	^{258}Db–esc, ^{254}Lr–EC, ^{254}No–α, ^{250}Fm–α…	
	^{258}Db–α, ^{254}Lr–EC, ^{254}No–esc, ^{250}Fm–α…	
	^{258}Db–EC, ^{258}Rf–esc§, ^{254}No–α, ^{250}Fm–α…	
	^{258}Db–EC, ^{258}Rf–α, ^{254}No–esc§, ^{250}Fm–α…	
	^{258}Db–α, ^{254}Lr–esc, ^{250}Fm–α…	
	^{258}Db–esc, ^{254}Lr–α, ^{250}Fm–α…	
^{257}Db$^{\#}$	^{257}Db–α, ^{253}Lr–α…	g - g = 0.735
	^{257}Db–α, ^{253}Lr–SF	m - m = 0.691
	^{257}Db–α, ^{253}Lr–esc, ^{249}Md–α…	Mean efficiency = 0.713
	^{257}Db–esc§, ^{253}Lr–α…	
	^{257}Db–missing esc, ^{253}Lr–α, ^{249}Md–α…	
	^{257}Db–esc§, ^{253}Lr–SF	
	^{257}Db–missing esc, ^{253}Lr–α, ^{249}Md–esc, ^{245}Es–α…	

Table 3.1: Accepted decay chains and corresponding chain detection efficiency factors. Symbol § denotes a "visible" escape signal is required. A detailed explanation of the calculations used may be found in Section 2.2.3.2.

the reduced number of assigned events. The ε_{BGS} described in Section 2.2.3.3 was simplified to 0.65 ± 0.02 for calculation of cross sections.

Many alpha particle energies are possible in the isotopes studied in these paired reactions, due to population of different states in the odd-odd daughters. It is important to keep in mind that α-decay of these odd-odd nuclei may also involve emission of conversion electrons, contributing to additional uncertainty in the observed decay energies.

Isomeric states were assigned with the most current literature results in mind, though further work such as α–γ spectroscopy is needed to ensure that these truly are the ground and metastable states. Previous work on these isomers [35] indicates very tentative assignment of these isomers, based on one correlated α–γ signal.

Half-life and cross section uncertainties were treated as a special case of the Poisson distribution [63] as described previously in Sections 2.2.3.4 and 2.2.6 and are reported at the 68% confidence interval. In addition, the uncertainty of the maximum likelihood fits is reported at the 68% confidence interval.

3.3 Observed Decay Chains: ^{208}Pb(^{51}V,x*n*)$^{259-x}$Db

3.3.1 1*n* Exit Channel

3.3.1.1 ^{258}Db, ^{258}Rf

Twenty-nine decay chains originating from the alpha decay of ^{258}Db were observed in this experiment, and more detail can be found in Table 3.2. Because of the requirements on what is assignable to *Z* and *A* values due to the similarity of the 1*n* and 2*n* exit channel products, EVR–SF chains that could be attributed to the EVR→^{258}Db–

Assignment	E_α (MeV)	Number of Events	Number of Correlations			
			To No	To Fission	To Md	To Fm, Es
^{258}Db	9.29	2	-	-	2	2
	9.17	7	3	-	1	2
	9.08	3	3	-	-	1
	9.01	5	1	-	2	2
	Other (see text)	5	1	-	2	2
	escape	7	-	-	3	2
^{257}Db^{m}	9.16	23	n/a	3	17	10
^{257}Db^{g}	9.07	10		-	8	2
	8.97	10		-	5	-
	escape	9		2	4	3

Table 3.2: Summary of decay chains observed in ^{51}V + ^{208}Pb reaction. See main text for more specific information.

EC→^{258}Rf–SF decay path were excluded, as they could also look like the EVR→^{257}Db–SF decay path. Of these twenty-nine ^{258}Db alpha decays, six were escape alphas, and one is inferred to be a "missing" alpha decay. The full-energy or reconstructed alpha particle decay energies observed fit well with those known in the literature [35]. We observe a dominant grouping at 9.17 MeV, consistent with these previous results. There may also be evidence of new alpha decay transitions at 8.91 and 9.13 MeV, each observed by two alpha decays.

In addition, we observed a greater population of the 9.01 MeV state in this work than in the literature [35], and this may be due, in part, to the alpha decay of ^{258}Rf, the EC daughter of ^{258}Db. It has recently been discovered by Gates *et al.* that ^{258}Rf has a much larger alpha decay branch than previously reported, 0.31 ± 0.11, with an alpha particle decay energy of 9.05 ± 0.05 MeV [45]. These two energies compare somewhat well

when the uncertainty in alpha particle energy resolution is factored in. The decay path of ^{258}Db–α→^{254}Lr–EC→^{254}No–α would appear identical to the decay path ^{258}Db–EC→^{258}Rf–α→^{254}No–α, and could skew such things as half-lives and branching ratios. We report a half-life of $4.4^{+1.0}_{-0.69}$ seconds for ^{258}Db, in very good agreement with the reported literature value of $4.4^{+0.9}_{-0.6}$ seconds [35]. Because of the selection rules for defining acceptable alpha chains, we do not make a quantitative assessment of the branching ratios for this isotope.

3.3.1.2 ^{254}Lr

From the alpha decay of ^{258}Db, we observe 22 alpha decays and infer seven EC decays of ^{254}Lr. Most of the alpha particle decay energies fit well to one of the two alpha lines in the literature. There is evidence for possibly a third line as well, due to five decays close in energy that are lower in energy than either the 8.46 or 8.41 MeV transitions [35]. The mean energy of these five decays is 8.34 MeV.

These results fit well with the known alpha and EC branching, as our calculated EC branch is 0.23 ± 0.08, compared to the literature value of 0.22 ± 0.06 [35]. This is quite good in light of the possibility of there being confusion as to which decay path has truly been observed (see 3.3.1.1). The measured total half-life of ^{254}Lr is $16.2^{+4.6}_{-2.9}$ seconds, consistent with previous work that reported 13^{+3}_{-2} seconds.

3.3.1.3 ^{254}No

Eight alpha decays of ^{254}No were observed in this experiment. This isotope could be produced two different ways, either as the EC product of ^{254}Lr, or the alpha decay product of ^{258}Rf. Because of the relatively small EC branch in ^{258}Db and the relatively small α branch in ^{258}Rf, we assume that most ^{254}No results from ^{258}Db – α – ^{254}Lr – EC – ^{254}No. The observed alpha particle decay energies fit well to the known value of 8.09 MeV [35]. We measure no half-life for ^{254}No, as most decays preceding it are the EC of ^{254}Lr, and the lifetime is measured as the sum of the two decays.

3.3.1.4 ^{250}Md

Eight decays of ^{250}Md were recorded, three alpha decays and five EC decays. Because an observable decay such as alpha particle emission or fission is required after an EC to conclusively determine if an EC decay has occurred, it is likely that we have undercounted the number of EC decays of this isotope. This makes it challenging to report its branching ratio, and for that reason we do not suggest one. The EC branching ratio found in the literature is 0.87 [35]. The three α-decays give a half-life of $41.8^{+49.6}_{-14.7}$ seconds, consistent with the newest literature value of 40^{+37}_{-13} seconds [35]. These values are also both consistent with the earlier measured half-life of 52 ± 6 seconds by P. Eskola [46].

3.3.1.5 ^{250}Fm

^{250}Fm is produced two different ways in this experiment, as the alpha decay product of ^{254}No, and as the EC product of ^{250}Md. Four and five decays of each path

were observed, respectively, and the measured alpha particle decay energies agree well with the literature value of 7.43 MeV [47]. We measured a half-life of $25.3^{+23.0}_{-8.1}$ minutes, which compares well to the known value of 30 ± 3 minutes [47, 48].

3.3.1.6 ^{246}Es

Only one alpha decay of ^{246}Es was observed, with an energy of 7.33 MeV, which compares well with the literature value of 7.35 MeV [60]. From the lifetime of 3.79 minutes we calculate a half-life of $2.6^{+12.5}_{-1.2}$ minutes, which compares fairly well to the literature value of 7.7 minutes [60]. This disparity is likely because only one event was used in the half-life calculation, and this quantity would be improved upon observation of more events. Because of background conditions, we did not continue searches beyond ^{246}Es or ^{250}Fm.

3.3.2 2*n* Exit Channel

3.3.2.1 ^{257}Db^{g}, ^{257}Db^{m}

Fifty-six decay chains are attributed to the decay of ^{257}Db in this experiment. Twenty-three are assigned to the metastable state, thirty-one to the ground state, and two we are unable to assign to a particular state. As stated above, there is difficulty in distinguishing the 1*n* and 2*n* exit channels unless the decay chain is observed at a compound nucleus excitation energy below the threshold for the emission of two neutrons (ensuring the product is 1*n* only), or if the decay of the Lr daughter is observed. The alpha particle decay energies of ^{254}Lr and ^{253}Lr^{g,m} differ by approximately 300 keV,

and their half-lives differ by greater than a factor of 10. These substantially different decay properties enable us to conclusively assign *Z* and *A*.

Nearly all the observed alpha particle decay energies match well to known alpha transitions in the literature. The metastable state in ^{257}Db decays at 9.16 MeV, and the ground state has two alpha lines, at 9.07 and 8.97 MeV [35, 36]. Two low energy alpha decays were observed at 8.72 and 8.80 MeV, followed by ^{253}Lr decays of slightly lower energy than the literature values as well. It is possible that these correlated low-energy decays represent a transition previously unseen, but in the absence of spectroscopic data we can not make specific claims.

The literature half-lives for the metastable and ground state of ^{257}Db are 760 milliseconds and 1.5 seconds, respectively [35, 36]. We have measured values of 790^{+210}_{-140} ms and $2.4^{+0.5}_{-0.4}$ seconds, respectively, in fairly good agreement with the previous work. We do not report partial half-lives or branching ratios for SF, because our selection criteria likely alter the value. We observed a higher production of the ground state relative to the metastable state at the higher bombarding energies (251.1 – 254.9 MeV, lab frame, center-of-target), likely indicating a shift in the isomer ratio with higher excitation energies.

3.3.2.2 ^{253}Lr^{g}, ^{253}Lr^{m}

The isotope ^{253}Lr possesses an isomeric state as well, according to Heßberger *et al.* [36]. Their previous work reports a metastable state with an alpha particle energy of 8.72 MeV and a 1.5 second half life. This isomer decays primarily by emission of an alpha particle but also has a small SF branch of <0.08 [36]. The ground state has very

similar decay properties. $^{253}Lr^{g}$ decays mostly by the emission of a 8.79 MeV alpha particle with a half-life of 0.57 seconds and a <0.013 SF branch [36]. An important finding is that there are no cross-correlations between the ground and metastable states in the alpha decay of ^{257}Db – ^{253}Lr – ^{249}Md. A mother-daughter plot illustrates this very well in their work, and we observed a similar result.

Three and two SF decays were observed for the metastable and ground state isomers of ^{253}Lr, respectively, resulting in SF branching ratios of 0.09 ± 0.05 and 0.06 ± 0.05. The measured total half-lives for each are $2.2^{+0.6}_{-0.4}$ seconds and $0.71^{+0.16}_{-0.11}$ seconds, respectively, close to the literature values.

3.3.2.3 ^{249}Md

We observed 36 alpha decays from ^{249}Md during the course of this experiment. We assume that ^{249}Md decays only by alpha particle emission and EC as stated in the literature [35, 46], and because we observed fifty-one alpha decays from ^{253}Lr, we conclude that fifteen decays of ^{249}Md are EC to ^{249}Fm. Because we can not observe the EC decay, and the daughter ^{249}Fm decays via EC with a branching of 0.85, it is difficult to confidently assign these truly as EC decays or calculate a branching ratio for this isotope. However, based on the above assumptions, the alpha branching appears to be consistent with the literature value of >0.60 [35]. The half-life measured from these alpha decays is $24.1^{+5.1}_{-3.9}$ seconds and compares very well with the reported values of 24 ± 4 seconds from earlier work by P. Eskola [46], and 25^{+14}_{-7} seconds from more recent findings by Heßberger *et al* [35].

3.3.2.4 ^{245}Es

^{245}Es is the lightest isotope that we observed during the experiment, by detection of fifteen alpha decays in the focal plane detector. The alpha particle decay energies match well with the known lines of 7.65 – 7.78 MeV [60]. The measured half-life is in marginal agreement with literature values, however. We measure a half-life of $27.3^{+10.2}_{-5.8}$ seconds, but Heßberger *et al.* measured 80^{+96}_{-28} seconds. The half-life of ^{245}Es listed in the *Table of Isotopes* [60] is 66 seconds. We find no outliers in the data, and we are unable to interpret this deviant result further.

3.4 Random Event Analysis for the ^{208}Pb(^{51}V,x*n*)$^{259-x}$Db Reaction

A calculation of the expected number of randomly correlated decays was done for this reaction, using the method described in Section 2.2.4. We chose sixty-five seconds to be the maximum time of event consideration, Δt_{max}, a multiple of five times the longest literature value for the half-life of ^{254}Lr. This isotope was chosen because it is the crucial isotope in the process of identifying whether the decay chain originates from the 1*n* or 2*n* exit channel. The focal plane event rates, R_α and N_{EVR} for the rate of alpha-like events and number of EVR-like events, respectively, were determined by integrating over their spectra. Alpha-like events were required to have energies between 7.0 – 10.0 MeV to cover the range of energies spanned by the Db, Lr, No, and Md products. EVR-like events were required to have energies between 8.0 – 24.0 MeV. The number of random chains expected over the duration of the experiment from an EVR followed by two alpha-like events was fewer than 0.36, and much lower for EVRs followed by greater than two alpha-like events and EVR-SF chains. All values calculated for the correlation of two

and three alpha-like events may be found in Table 3.3. It is unlikely that one of the event chains assigned to formation and decay of Db is due to a random correlation of unrelated events.

$E_{lab,\ COT}$ (MeV)	E* (MeV)	Probability of Random EVR–α–α Correlation	Probability of Random EVR–α–α–α Correlation
236.2	13.2	0.24	$2.2\ 10^{-4}$
239.9	16.2	0.07	$5.2\ 10^{-5}$
243.7	19.2	0.04	$3.3\ 10^{-5}$
247.4	22.2	0.16	$1.7\ 10^{-4}$
251.1	25.2	0.02	$1.2\ 10^{-5}$
254.9	28.2	*0.36*	$4.2\ 10^{-4}$

Table 3.3: Summary of random rate correlation calculations, see Sections 2.2.4 and 3.4 for more information. Highest probability is italicized.

3.5 Excitation Functions and Discussion

A summary of the reactions studied at GSI and LBNL together with their respective bombarding energies, cross sections, and associated uncertainties can be found in Tables 3.4 and 3.5. Detailed information about each excitation function and a comparison is presented below. Values from the FBD prediction are presented and compared to experimental values as well.

3.5.1 Excitation Function for ^{209}Bi(^{50}Ti,x*n*)$^{259-x}$Db

The excitation function measured in the ^{209}Bi(^{50}Ti,x*n*)$^{259-x}$Db reaction by Gates *et al.* [72], previously mentioned in Section 3.1.4, can be seen in Figure 3.1 with a Gaussian-exponential fit from the maximum likelihood fit method described earlier in

Lab	Rxn	E_{cot} (MeV)	E* (MeV)	Target Thickness (mg/cm^2)	Dose (10^{16} ions)	Num. 1*n* Events	^{258}Db σ_{1n} (pb)	Num. 2*n* Events	^{257}Db σ_{2n} (pb)
GSI (1985)	^{50}Ti + ^{209}Bi	232.5	$12.5^{+3}_{-1.5}$	0.5-0.7	0.6	1@	500 ± 300	-	-
		237.5	$16.5^{+3}_{-1.5}$	0.5-0.7	16.2	129@	2900 ± 300	-	300^{+300}_{-150}
		242.5	$21^{+3}_{-1.5}$	0.5-0.7	1.69	10@	-	-	-
		247.5	25^{+93}_{-50}	0.5-0.7	1.45	8@	600 ± 300	-	2100 ± 800
GSI (2001)	^{50}Ti + ^{209}Bi	226.5	10.5	0.450	-	-	120 ± 60	-	2400 ± 300 (max)
		229.0	12.6	0.450	-	-	700 ± 110	-	
		230.7	13.9	0.450	-	-	2100 ± 180	-	
		232.4	15.3	0.450	-	-	4300 ± 430	-	
		234.9	17.3	0.450	-	-	2200 ± 240	-	
		237.3	19.2	0.450	-	-	810 ± 120	-	
		239.5	21.0	0.450	-	-	390 ± 130	-	
		243.0	23.8	0.450	-	-	<180	-	
		245.5	25.9	0.450	-	-	<30	-	
		251.0	30.3	0.450	-	-	0	-	
LBNL (Gates)	^{50}Ti + ^{209}Bi	229.7	13.2	0.47	2.19	1	45^{+210}_{-37}	n/a	n/a
		231.7	14.8	0.47	1.85	23	2100^{+600}_{-500}	0	<140
		233.5	16.2	0.47	1.08	16	4500^{+1400}_{-1100}	0	<230
		235.9	18.2	0.47	0.74	8	3300^{+1600}_{-1100}	3	540^{+530}_{-300}
		239.7	21.2	0.47	1.25	9	2200^{+1000}_{-700}	7	740^{+400}_{-270}

Table 3.4: Summary of ^{50}Ti + ^{209}Bi experimental results from LBNL and GSI. A dash means data was not available. @ symbol denotes sum of 1*n* and 2*n* events.

Section 2.2.5. The filled squares represent the 1*n* data points, the filled circles represent the 2*n* data points, the black arrow on the abscissa represents the location of the barrier from the "Fusion By Diffusion" model [29, 30, 32], and the dashed line represents the fit.

Lab	Rxn	E_{cot} (MeV)	E* (MeV)	Target Thickness (mg/cm^2)	Dose (10^{16} ions)	Num. 1*n* Events	^{258}Db σ_{1n} (pb)	Num. 2*n* Events	^{257}Db Cross Section (pb)
LBNL (this work)	^{51}V + ^{208}Pb	236.2	13.2	0.44	2.02	2	130^{+170}_{-90}	-	n/a
		239.9	16.2	0.44	1.54	10	1200^{+500}_{-370}	2	210^{+270}_{-130}
		243.7	19.2	0.44	3.99	11	500^{+200}_{-150}	9	360^{+160}_{-120}
		247.4	22.2	0.44	2.31	4	310^{+250}_{-150}	29	2000^{+400}_{-370}
		251.1	25.2	0.44	1.34	1	140^{+310}_{-110}	13	1500^{+600}_{-400}
		254.9	28.2	0.44	4.20	1	40^{+100}_{-40}	5	190^{+130}_{-80}

Table 3.5: Summary of ^{51}V + ^{208}Pb experimental results, see Table 3.4 for more information.

A maximum 1*n* cross section of $4.2^{+1.1}_{-0.9}$ nb was observed, comparing somewhat well to the maximum of 5.83 ± 0.77 nb obtained with the fitting procedure. The centroids of these maxima are similar in value also, with a compound nucleus excitation energy of 16.2 MeV from our observed point and 16.8 ± 0.2 MeV from the fit. The position of the barrier from the FBD model is 19.6 MeV and indicates that the peak of this excitation function is 2.8 MeV below the barrier.

The 2*n* exit channel was also observed at the higher bombarding energies studied in this work. The lowest energy used in this experiment is below the threshold for the production of the 2*n* exit channel, therefore an upper limit is not assigned to this point. The two upper limits in the 2*n* data are reasonable values, consistent with the low-energy side of this partial excitation function, at 250 and 470 pb. The maximum observed 2*n* cross section is at 740^{+400}_{-270} pb. It is unclear where the maximum of this function is, and additional work may be warranted.

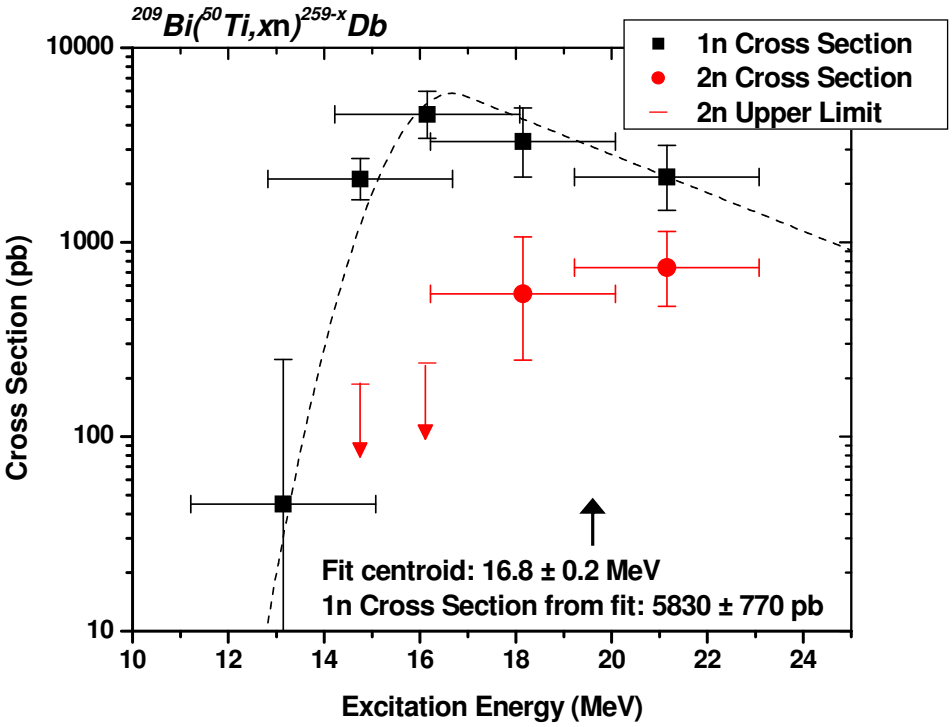

Figure 3.1: Results of the ^{209}Bi(^{50}Ti,xn)$^{259-x}$Db reaction. Filled squares and the dashed line represent the 1n exit channel, filled circles represent the 2n exit channel. The arrow on the abscissa represents the location of the barrier, calculated using the "Fusion By Diffusion" model [29, 30, 32].

3.5.2 Excitation Function for ^{208}Pb(^{51}V,xn)$^{259-x}$Db

Similarly to Section 3.5.1, we present in Figure 3.2 an excitation function for the other reaction in this pair which produces ^{258}Db. The maximum observed 1n cross section is $1.18^{+0.50}_{-0.37}$ nb, comparing well with the fit value of 1.30 ± 0.24 nb. The compound nucleus excitation energy centroid corresponding to the maximum is 16.0 ± 0.4 MeV, respectively. The location of the barrier is at 21.9 MeV, considerably higher in energy than that of ^{50}Ti + ^{209}Bi reaction. The centroid is 5.9 MeV below the FBD barrier.

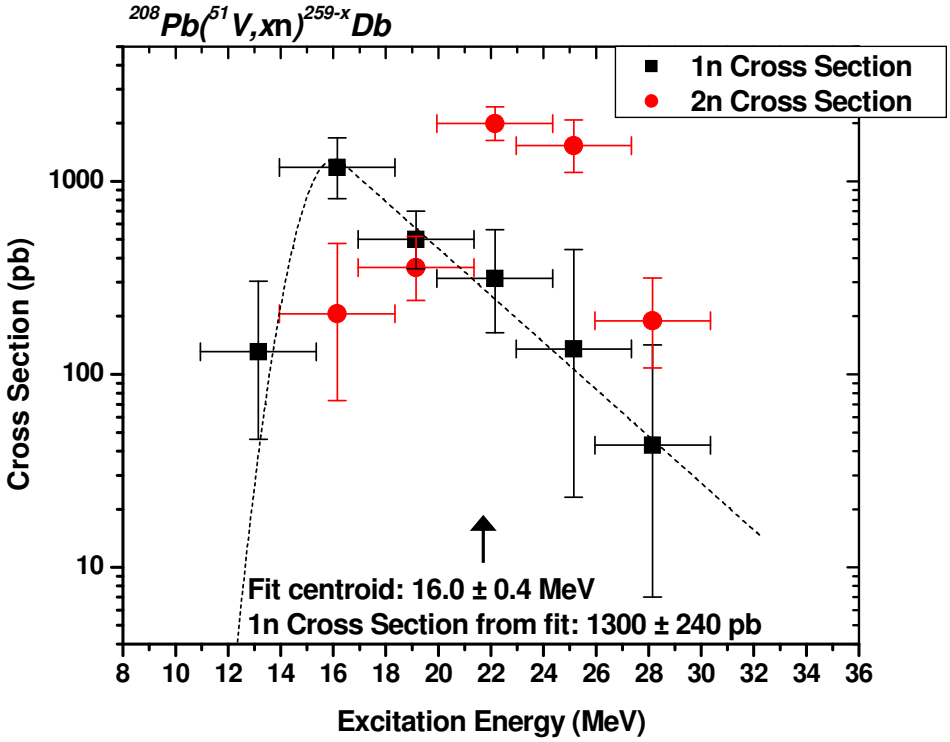

Figure 3.2: Results of the ^{208}Pb(^{51}V,x*n*)$^{259-x}$Db reaction. Filled squares and the dashed line represent the 1*n* exit channel, filled circles represent the 2*n* exit channel. The arrow on the abscissa represents the location of the barrier, calculated using the "Fusion By Diffusion" model [29, 30, 32].

We observed events corresponding to the 2*n* exit channel at all five above-2*n*-threshold bombarding energies in this experiment. The peak of these five points is 2.0 nb, at a compound nucleus excitation energy of 22.2 MeV, higher than the maximum observed 1*n* cross section. We observe what appears to be a more symmetric shape for the excitation function of the 2*n* product, possibly indicating that the 1*n* excitation function is being "cut off" by the barrier.

3.5.3 Comparison of Excitation Functions

3.5.3.1 LBNL vs. GSI ^{209}Bi(^{50}Ti,*n*) ^{258}Db Excitation Functions

The same fitting procedure used with the LBNL data was used with the GSI data [36]. Upon examining the 1*n* excitation functions for the ^{50}Ti + ^{209}Bi reactions done at LBNL and GSI, seen in Figure 3.3, we see that the maxima are not close in peak magnitude. The peaks from the fits are 5.83 ± 0.77 and 4.19 ± 0.20 nb for the LBNL and GSI results, respectively. Systematic errors in cross section determination may account for this difference.

Though the measured maximum cross sections differ by about 20%, the centroids of the fits vary more than 20%. The centroid of the LBNL fit is located at a compound nucleus excitation energy of 16.8 ± 0.2 MeV, and our fit to the GSI data is at a compound nucleus excitation energy of 15.6 ± 0.1 MeV. This represents a difference greater than 1 MeV between the two reactions, where there really should be at most a small difference. This causes one to wonder what phenomena are contributing to this result, and if experimental findings from these two laboratories may be fairly compared. The shapes of the excitation functions on the low energy side are comparable, but the shapes on the high-energy side appear different. This could be a result of the GSI data having additional high-energy points included in the fitting procedure.

3.5.3.2 Comparison of LBNL ^{208}Pb(^{51}V,*n*) Vs. ^{209}Bi(^{50}Ti,*n*) Excitation Functions

The first pair of reactions in this systematic study to investigate any role that the entrance channel plays in compound nucleus formation is the pair to produce ^{258}Db. A plot of the ^{208}Pb(^{51}V,*n*) and ^{209}Bi(^{50}Ti,*n*) excitation functions is shown in Figure 3.4. The

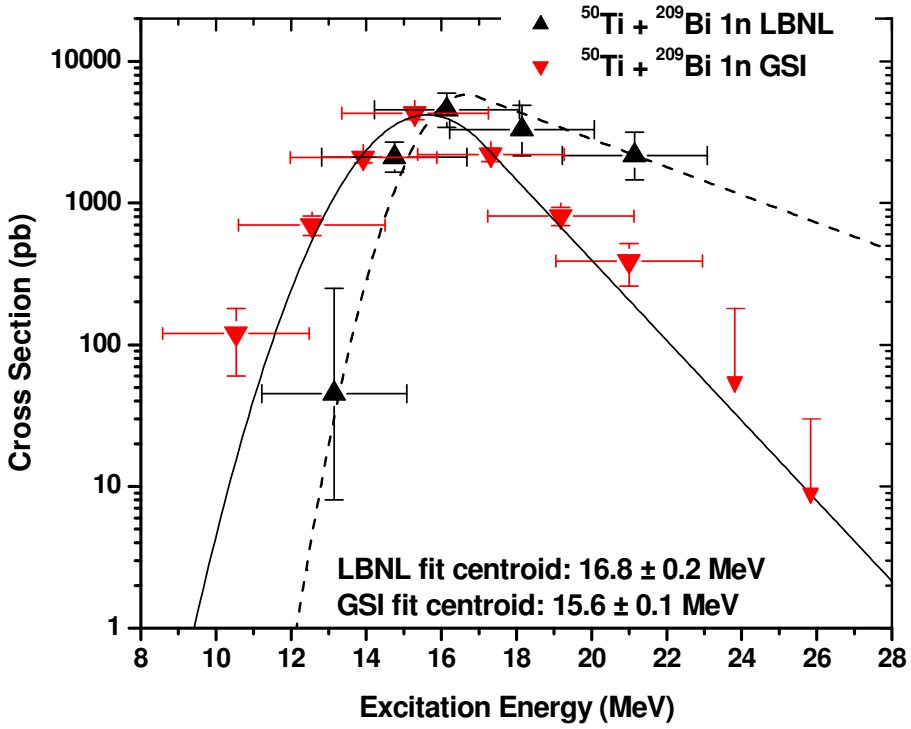

Figure 3.3: Comparison of LBNL and GSI ^{209}Bi(^{50}Ti,*n*)^{258}Db reactions. Upward-pointing filled triangles and the dashed line represent the work done at LBNL [72], downward-pointing filled triangles and the solid line represent the work done in 2001 at the GSI [36].

filled diamonds and solid line represent the ^{50}Ti + ^{209}Bi excitation function and its fit, and the upward-pointing filled triangles and dashed line represent the ^{51}V + ^{208}Pb excitation function and its fit.

We see that the ^{50}Ti-based reaction's cross section is more than a factor of four larger than the ^{51}V-based reaction. This result agrees with what one would expect from the standpoint of effective fissility [23], with the reaction possessing a lower effective

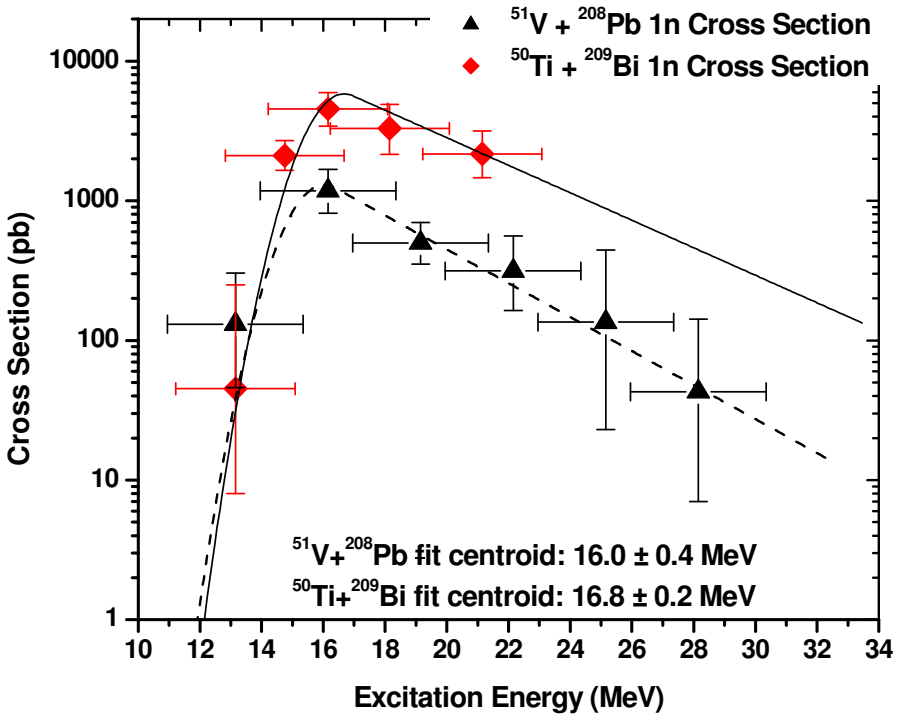

Figure 3.4: Comparison of ^{209}Bi(^{50}Ti,*n*)^{258}Db and ^{208}Pb(^{51}V,*n*)^{258}Db reactions, both performed at LBNL. Filled triangles and the dashed line represent the ^{50}Ti + ^{209}Bi reaction [72], filled diamonds and the solid line represent the ^{51}V + ^{208}Pb reaction.

fissility having a higher cross section. Whether this argument holds true for successive pairs of reactions in this study will be of interest. It is possible that because the ^{51}V + ^{208}Pb reaction is more sub-barrier than the ^{50}Ti + ^{209}Bi reaction by 3.1 MeV, the reaction could be hindered, or "cut-off", on the low energy side of the excitation function, resulting in a lower cross section.

The centroids of these reactions' maxima are fairly close in location to one another, at 16.8 ± 0.2 and 16.0 ± 0.4 MeV for the ^{50}Ti + ^{209}Bi and ^{51}V + ^{208}Pb reactions,

respectively. We would expect the energies to be nearly identical, given that the same compound nucleus is being produced, which should have the same second-chance fission threshold. It is also possible that the slight discrepancy is due to the fitting procedure and does not represent a significant difference in reaction energetics.

3.5.4 Comparison to Model Predictions

FBD model predictions of the maximum 1*n* cross sections for these two reactions and their corresponding maxima were provided by W. J. Świątecki. The prediction for the ^{50}Ti + ^{209}Bi reaction is 3.1 nb. This is smaller but within a factor of two of the fit maxima of 5.83 ± 0.77 and 4.19 ± 0.20 nb for the LBNL and GSI results, respectively. Similarly, the prediction for the ^{51}V + ^{208}Pb reaction is 2.0 nb, also within a factor of two of the 1.30 ± 0.24 nb resulting from the fit to the excitation function.

The predicted centroids of the ^{50}Ti + ^{209}Bi and ^{51}V + ^{208}Pb reactions are at compound nucleus excitation energies of 14.2 and 14.5 MeV, respectively. These are 2.6 and 1.5 MeV lower in energy than the experimental values of 16.8 ± 0.2 and 16.0 ± 0.4 MeV for the ^{50}Ti + ^{209}Bi and ^{51}V + ^{208}Pb from the fits of the excitation functions, respectively. This indicates a slight but consistent underestimate of the centroids. This is additional evidence that the 1-3 MeV offset for odd-*Z* CN in the "Optimum Energy Rule" is required to reach the proper optimal bombarding energy for a 1*n* reaction.

4. Experimental Results:

*Production of Bohrium in the ^{209}Bi(^{54}Cr,x**n**)$^{263-x}$Bh and ^{208}Pb(^{55}Mn,x**n**)$^{263-x}$Bh Reactions*

4.1 Previous Work

4.1.1 Dubna Experiments

The first studies done with the ^{209}Bi(^{54}Cr,*n*)^{262}Bh and ^{208}Pb(^{55}Mn,*n*)^{262}Bh reactions were performed at the JINR in Dubna, Russia, in 1976 [70]. The aim of these experiments was to study various fission probabilities of various isotopes of elements 103, 105, and 107. The results relevant to element 107 will now be examined. A focus of their work was to produce and study ^{261}Bh via the ^{208}Pb(^{55}Mn,2*n*) and ^{209}Bi(^{54}Cr,2*n*) reactions, estimating a cross section of approximately 1 nb for the latter reaction. The systematics of transactinide cold fusion type compound nucleus reactions were not as well understood at that time, and the 2*n* exit channel was thought to have a larger cross section. They stated that if ^{261}Bh decayed by spontaneous fission, or decayed via alpha emission to ^{257}Db which then spontaneously fissioned, they would observe it in their track detectors. (The same mica track detector system was used as described in Chapter 3.1.1.) A new spontaneous fission activity with a half-life of 1-2 ms was reported that they attributed to a 0.20 decay branch of ^{261}Bh. We now know that ^{261}Bh decays exclusively by alpha particle emission.

Similar to their work with dubnium detailed in Section 3.1, because these experiments inferred rather than directly observed the alpha decay of ^{261}Bh, they could not conclusively determine the *Z* or *A* of the product. Their reported decay properties and half-lives are now known to be incorrect, and credit for discovery of the new element 107 was not awarded.

4.1.2 GSI Experiments

Because of the JINR's difficulty in conclusively identifying bohrium via the methods described above, Münzenberg *et al.* seized the opportunity at GSI using the ^{209}Bi(^{54}Cr,*n*)^{262}Bh reaction. [7] The use of the physical separator SHIP in combination with a position-, time-, and energy-sensitive detector array was crucial to their success in the discovery of element 107. Their first attempt was successful, and produced six alpha decay chains of ^{262}Bh. An isomeric state also decaying via alpha emission was identified in this first work, and new isotopes of $^{258, 257}$Db and ^{254}Lr were produced as decay daughters. The observation of decays through these unknown nuclides to known ones such as ^{250}Md and ^{250}Fm was important in the assignment of *Z* and *A*. Follow-up experiments using the same reaction at additional bombarding energies [38] led to the production of ten chains of ^{261}Bh as the 2*n* reaction product, and 29 additional decay chains of ^{262}Bh helped to identify additional alpha transitions.

^{262}Bh^{g} is now known to decay by emission of an alpha particle with energies of 9.74, 9.91, or 10.06 MeV with a half-life of 102 ± 26 ms. Similarly, ^{262}Bh^{m} decays by emission of an alpha particle of 10.24 or 10.40 MeV with a half-life of 8.0 ± 2.1 ms. This later work produced excitation functions with maxima of 163 ± 34 pb and 36^{+22}_{-14} pb for

^{262}Bh and ^{261}Bh, respectively, and has become the standard reference for work on these isotopes.

^{262}Bh has also been observed as the decay daughter of ^{266}Mt by GSI [9] and more recently at LBNL. The observed decay properties agree well with the currently accepted literature values. Information about the production and decay of ^{266}Mt can be found in Chapter 6.

4.1.3 LBNL Experiments

In 2004, Folden *et al.* investigated the ^{208}Pb(^{55}Mn,*n*)^{262}Bh reaction [37], the complementary reaction to ^{209}Bi(^{54}Cr,*n*)^{262}Bh. Using the 88-Inch Cyclotron and the BGS at LBNL, three bombarding energies were studied to create an excitation function with a peak 1*n* cross section of 540^{+180}_{-150} pb. This result was unexpectedly large compared to the prediction of approximately 120 pb provided to us by Świątecki from the FBD model [29, 30, 32]. The observed decay properties were in good agreement with the work in [7, 38], and an additional alpha transition at 9.66 MeV was discovered.

4.1.4 Motivation for Additional Studies

Upon examination of these results, a few interesting details arise. The argument that using heavy ion beams with Bi targets would lead to a lower effective fissility, and consequently a higher cross section, is not upheld when Folden's work is compared to that of GSI. Also, the peak 1*n* cross section observed in the GSI results is at a compound nucleus excitation energy of 20 ± 2 MeV, which is significantly higher than the experimental systematics for this reaction type. Additionally, we obtained information

that the targets used in the GSI work were at times faulty with inhomogeneous structure, and the beam energies used were not well known as a result of the UNILAC accelerating multiple charge states simultaneously. For these reasons, we chose to study the ^{54}Cr + ^{209}Bi reaction to gain a better understanding of this reaction pair. In addition, we chose to continue the study of the ^{55}Mn + ^{208}Pb reaction to extend the excitation function of the 1*n* product, and to hopefully observe the ingrowth of the 2*n* excitation function as well.

4.2 Experimental Conditions

The BGS was used in its standard configuration with MWPC installed, similar to the description in Section 3.2. Beams of $^{54}Cr^{12+}$ and $^{55}Mn^{13+}$ passed through the carbon vacuum window and impinged upon the ^{209}Bi and ^{208}Pb target wheels, respectively, described in Section 2.1.1.2. The target wheel rotation speed was approximately 5-10 Hz. Before the experiments, the four-peak alpha source described in Section 2.2.1.1 was used to collect external calibration data. No internal calibration reactions were run due to the lack of suitable target and projectile combinations at the time of the experiments. The alpha particle energy resolution determined by the four-point source data over the course of these experiments has $\sigma = \pm 31$ keV. The systematic error in the calibration for alpha particles in the FPD was ± 5 keV, determined by comparing measured and accepted E_α from implanted activity after correction for the detector's dead layer and the recoil of the daughter product.

Projectile energies expected to be optimal for production of each reaction's 1*n* exit channel were chosen based on calculations from Świątecki *et al.*'s "Fusion by Diffusion" model [29, 30]. Experimental masses were used when available, and

Lab	Reaction	E_{cot} (MeV)	E* (MeV)	Target Thickness (mg/cm^2)	Dose (10^{16} ions)	^{262}Bh σ_{1n} (pb)	^{261}Bh σ_{2n} (pb)
GSI	^{54}Cr + ^{209}Bi	258.9	17	0.66	7	93^{+93}_{-50}	< 51
		263.4	20	0.39	71	163^{+34}_{-34}	36^{+25}_{-16}
		265.9	24	0.40	18	27^{+27}_{-14}	36^{+22}_{-14}
		271.0	28	0.40	14	< 56	24^{+55}_{-19}
LBNL (Folden)	^{55}Mn + ^{208}Pb	260.0	11.1	0.47	5.7	24^{+55}_{-20}	< 41
		264.0	14.3	0.47	4.2	590^{+170}_{-140}	< 56
		268.0	17.4	0.47	7.8	210^{+100}_{-71}	32^{+43}_{-21}
LBNL (this work)	^{55}Mn + ^{208}Pb	273.0	21.4	0.46	8.1	<49	43^{+57}_{-28}
		278.0	25.3	0.46	7.1	<56	< 46
		283.0	29.3	0.46	7.2	30^{+68}_{-24}	< 44
LBNL (this work)	^{54}Cr + ^{209}Bi	253.5	11.3	0.44	3.1	48^{+110}_{-40}	-
		257.1	14.2	0.44	2.3	260^{+200}_{-120}	-
		260.9	17.2	0.44	1.5	440^{+430}_{-240}	< 210
		264.7	20.2	0.44	23	60^{+35}_{-24}	8^{+18}_{-7}
		268.4	23.2	0.44	6.3	36^{+82}_{-30}	28^{+65}_{-23}
		272.3	26.3	0.44	8.3	< 50	67^{+65}_{-36}

Table 4.1: Energies, integrated beam doses, target thicknesses, and cross sections for each reaction. Data from [37, 38] are presented for comparison.

tabulated mass defects from the Thomas-Fermi model [73] were used for those nuclides with unknown masses. Table 4.1 contains a summary of the beam energies, integrated beam doses, and resulting cross sections for this work as well as for previous studies. The evaporation residues recoiled out of the target with the momentum of the beam and into the BGS. The BGS magnet settings were chosen to guide only products with a

magnetic rigidity of 2.16 T·m for both the 1*n* and 2*n* exit channels to the Si-strip focal plane detector (FPD). The magnetic rigidity was determined with data from [37]. Monte Carlo simulations of EVR trajectories through the BGS [55] described in Section 2.2.3.3 indicate a total separator efficiency of 0.64 ± 0.02 and 0.67 ± 0.02 for the ^{54}Cr + ^{209}Bi and ^{55}Mn + ^{208}Pb reactions, respectively. The ε_{BGS} was simplified to 0.65 ± 0.02 for calculation of cross sections.

During the irradiations, the rate of "EVR-like events" ($8.0 < E_{EVR} < 24.0$ MeV coincident with MWPC signals and anticoincident with punchthrough or upstream signals) was 1.1 – 3.2 Hz. The rate of "alpha decay-like events" ($7.0 < E_{alpha} < 11.0$ MeV, in the focal plane only, or reconstructed from a focal plane plus an upstream signal, anticoincident with the MWPC and punchthrough signals) was 0.04 – 0.10 Hz. ^{262,261}Bh decay chains were identified by time- and position-correlated decays after an EVR implantation event. A fast beam-shutoff system was implemented to reduce the likelihood of random correlations. (See Section 2.2.4 for a discussion of random correlations) Upon the detection of an EVR correlated to an alpha-like event (within 3σ of position and 30 sec of the EVR), the beam was automatically switched off for 180 s to enable registration of any subsequent daughter- or granddaughter-like decays under strongly reduced background conditions. The data files were sorted offline, searching for EVR- and alpha-like events with the same energy gates as listed above, and >80 MeV spontaneous fission (SF) –like events ($80 < E_{fission} < 300$ MeV, no MWPC signal). Once potential decay chains were identified through the offline searches, more specific searches were carried out to lifetimes of 10^4 seconds to try to identify Z = 99-100 decays with long half-lives.

Distinguishing decay chains of ^{262}Bh from chains of ^{261}Bh presented a challenge due to the strikingly similar alpha particle energies and lifetimes of ^{262m}Bh and ^{261}Bh, similar to that of ^{258,257}Db in Chapter 3. We have chosen to only assign events fitting the criteria in Table 4.2, and have calculated alpha chain detection efficiencies using the same method as described in Section 2.2.3.2.

4.3 Observed Decay Chains: ^{208}Pb(^{55}Mn,x*n*)^{262}Bh^{g,m} and ^{209}Bi(^{54}Cr,x*n*)^{262}Bh^{g,m}

It is important to keep in mind that the decays of many of these odd-odd nuclei may involve the emission of conversion electrons, which can sum with alpha particle energies. Previous work [38] indicates uncertainty in the true nature of the ground- or metastable state assignments of ^{262}Bh, ^{257}Db, and ^{253}Lr. Our results are unable to clarify this challenging situation further, so isomeric states were assigned with the most current literature results in mind. Assignments were primarily based on the alpha particle energy (for full energy or reconstructed events), and secondarily on the alpha decay lifetimes. In the case of an escaped alpha particle with a lifetime that could be reasonably assigned to either state, or when the energies and values could be potentially assigned to either state, we have chosen to not assign a state. Only six decays in the 23 chains were left unassigned. Because of the high degree of selectivity and difficulty in conclusively identifying mass numbers and isomers, it is possible that we have introduced a slight bias to our half-life values concerning ^{262}Bh^{g,m}, ^{261}Bh, ^{257}Db^{g,m}, and ^{253}Lr^{g,m}.

Decay Chain	Accepted Decay Paths	Alpha Chain Detection Efficiency Factor
$^{262}Bh^{m,g}$	$^{262}Bh–\alpha,^{258}Db–\alpha…$	0.801
Production of ^{261}Bh unfavorable	$^{262}Bh–\alpha,^{258}Db–EC,^{258}Rf–SF$	
	$^{262}Bh–\alpha,^{258}Db–EC,^{258}Rf–\alpha…$	
	$^{262}Bh–esc,^{258}Db–\alpha,^{254}Lr–\alpha…$	
	$^{262}Bh–\alpha,^{258}Db–esc,^{254}Lr–\alpha…$	
	$^{262}Bh–esc^{\S},^{258}Db–EC,^{258}Rf–SF$	
	$^{262}Bh–esc,^{258}Db–EC,^{258}Rf–\alpha,^{254}No–\alpha…$	
$^{262}Bh^{m,g}$	$^{262}Bh–\alpha,^{258}Db–\alpha,^{254}Lr–\alpha…$	0.540
Production of ^{261}Bh and ^{262}Bh favorable	$^{262}Bh–\alpha,^{258}Db–\alpha,^{254}Lr–EC,^{254}No–\alpha…$	
	$^{262}Bh–\alpha,^{258}Db–EC,^{258}Rf–\alpha,^{254}No–\alpha…$	
	$^{262}Bh–esc,^{258}Db–\alpha,^{254}Lr–\alpha…$	
	$^{262}Bh–\alpha,^{258}Db–esc,^{254}Lr–\alpha…$	
	$^{262}Bh–esc,^{258}Db–\alpha,^{254}Lr–EC,^{254}No–\alpha…$	
	$^{262}Bh–\alpha,^{258}Db–esc,^{254}Lr–EC,^{254}No–\alpha…$	
	$^{262}Bh–\alpha,^{258}Db–\alpha,^{254}Lr–EC,^{254}No–esc,^{250}Fm–\alpha…$	
	$^{262}Bh–esc,^{258}Db–EC,^{258}Rf–\alpha,^{254}No–\alpha…$	
$^{261}Bh^{\#}$	$^{261}Bh–\alpha,^{257}Db^{x}–\alpha,^{253}Lr^{x}–\alpha…$	g-g = 0.704
(x = m or g state)	$^{261}Bh–\alpha,^{257}Db^{x}–\alpha,^{253}Lr^{x}–SF$	m-m = 0.656
	$^{261}Bh–esc,^{257}Db^{x}–\alpha,^{253}Lr^{x}–\alpha…$	Mean efficiency = 0.680
	$^{261}Bh–\alpha,^{257}Db^{x}–esc,^{253}Lr^{x}–\alpha…$	
	$^{261}Bh–\alpha,^{257}Db^{x}–\alpha,^{253}Lr^{x}–esc^{\S},^{249}Md–\alpha…$	
	$^{261}Bh–\alpha,^{257}Db^{x}–esc^{\S},^{253}Lr^{x}–SF$	
	$^{261}Bh–esc^{\S},^{257}Db^{x}–\alpha,^{253}Lr^{x}–SF$	
	$^{261}Bh–\alpha,^{257}Db^{x}–\alpha,^{253}Lr^{x}–$missing esc, $^{249}Md–\alpha,\ ^{245}Es–\alpha…$	

Table 4.2. Accepted decay paths for $^{262}Bh^{g,m}$ and ^{261}Bh, and their corresponding alpha chain detection efficiencies. § symbol denotes where a detected escape signal is required. # symbol denotes decay chains containing isomers with different decay properties and branching ratios, and efficiencies are calculated for the metastable and ground-state paths individually. "x" denotes where either the ground state or metastable state is possible, but only ground state-to-ground state or metastable state-to-metastable state transitions are possible.

4.3.1 1*n* Exit Channel

4.3.1.1 $^{262}Bh^{g}$, $^{262}Bh^{m}$

Sixteen decay chains corresponding to the alpha decay of ^{262}Bh were identified, fifteen of which were from the six energies studied in the $^{54}Cr + ^{209}Bi$ reaction, and one event from the highest energy studied in the $^{55}Mn + ^{208}Pb$ reaction. These decay chains may be viewed in detail in Tables 4.3 and 4.4. Of these sixteen ^{262}Bh decay chains, four were classified as escapes, exiting the front of the focal plane detector and leaving no signal in an upstream detector; one event was missing, leaving a signal below our detection threshold and thus was not discernible over the noise peak; and one event we consider "shallow escapes", where the energy of the detected decay is too low for a standard full-energy or reconstructed alpha decay, yet too high for a typical escape alpha signature. We believe that these high energy escapes result from the alpha particle escaping at a shallow angle in the focal plane detector, presumably passing through the gap between the FPD and upstream detectors, thereby leaving a large fraction of the available energy as a signal.

The ten full-energy or reconstructed $^{262}Bh^{g,m}$ alpha decays that we observed fit well to previously reported alpha decay energies [37, 38]. It is possible that the 9.39 MeV decay observed in Event 8 of Table 4.4 is a new, low-energy transition, the result of an alpha decay to an excited state of the daughter. The short lifetime of 10 ms may indicate decay from the metastable state. In addition, the 10.13 MeV decay in Event 20 has not been observed before, also possibly evidence of a new alpha decay transition.

We have conservatively re-examined the event assignments from the work of Folden *et al.* [37] and applied the same decay chain restrictions as in Table 4.2 to enable

Reaction	E_{COT} (MeV)	E* (MeV)	Event #	Strip #	E_{EVR} (MeV)	Position (mm)	Decay Energy (MeV)	Position (mm)	Lifetime	^{A}Z
$^{55}Mn + ^{208}Pb$	273	21.4	1	27	18.787	-5.5 ± 0.1	10.054	-7.0 ± 0.3	0.00353 s	^{261}Bh
							1.457	-6.8 ± 1.9	0.98428 s	^{257g}Db
							190.7= [15.7+175.0]	-5.2 ± 0.2	0.03931 s	^{253g}Lr
			2	24	22.452	13.1 ± 0.1	10.331	12.9 ± 0.3	0.00135 s	^{261}Bh
							3.086	12.9 ± 0.9	2.90143 s	^{257g}Db
							8.778	12.9 ± 0.3	0.48863 s	^{253g}Lr
	283	29.3	3	12	17.873	18.2 ± 0.2	Missing			^{262}Bh
							9.024	18.6 ± 0.3	3.59708 s*	^{258}Db
							8.394	18.2 ± 0.3	7.73227 s	^{254}Lr
							EC			^{250}Md
							7.409	18.3 ± 0.4	70.07670 m*	^{250}Fm

Table 4.3. Decay chains from the $^{208}Pb(^{55}Mn, xn)^{263-x}Bh$ reaction: Reconstructed energies are listed with the focal plane energy listed first, followed by the calculated energy from a missing signal from either the top or bottom of the strip in parentheses, ending with the energy deposited in the upstream detector. Boldface type indicates decay was observed during a beam-off interval. Lifetimes of decays following EC are the sum of the two lifetimes and indicated with an asterisk (*). Decay chains that could include the alpha decay of ^{258}Rf are denoted by a dagger symbol (†).

E_{COT} (MeV)	E* (MeV)	Event #	Strip #	E_{EVR} (MeV)	Position (mm)	Decay Energy (MeV)	Position (mm)	Lifetime	^{A}Z
253.5	11.3	4	13	17.121	13.1 ± 0.2	9.762= [0.639+(0.234)+8.889]	>0.0	0.08917 s	^{262g}Bh
						8.216= [1.292+6.924]	14.3 ± 2.2	0.16206 s	^{258}Db
						8.384	13.2 ± 0.3	13.60693 s	^{254}Lr
257.1	14.2	5	22	17.77	14.5 ± 0.2	9.648= [1.023+8.625]	16.2 ± 2.7	0.28408 s	^{262g}Bh
						EC			^{258}Db
						187.2= [17.8+169.4]	14.2 ± 0.2	0.46444 s*	^{258}Rf
		6	29	19.223	-4.3 ± 0.1	9.735= [0.742+8.993]	-14.0 ± 3.8	0.02422 s	^{262g}Bh
						9.067	-4.4 ± 0.3	11.31248 s	^{258}Db
						8.376	-4.2 ± 0.3	2.55264 s	^{254}Lr
						EC			^{250}Md
						7.368	-4.3 ± 0.4	66.8496 m*	^{250}Fm
		7	11	16.081	9.0 ± 0.2	0.652	4.4 ± 4.3	0.11001 s	^{262g}Bh
						9.106	8.6 ± 0.3	5.25444 s	^{258}Db
						8.420	8.9 ± 0.3	2.75003 s	^{254}Lr
		8	15	17.151	-25.6 ± 0.2	9.387	-25.6 ± 0.3	0.01048 s	^{262m}Bh
						8.959	-25.5 ± 0.3	0.02439 s	^{258}Db
						EC			^{254}Lr
						8.034	-25.7 ± 0.3	34.20462 s*	^{254}No
260.9	17.2	9†	3	18.33	-0.2 ± 0.2	10.067= [1.054+9.013]	0.8 ± 2.7	0.00077 s	^{262m}Bh
						9.025	-0.3 ± 0.3	0.89196 s	^{258}Db
						EC			^{254}Lr
						8.075= [0.804+7.270]	-4.1 ± 3.5	108.04668 s*	^{254}No
						7.373	-0.6 ± 0.4	30.3652 m	^{250}Fm
		10	31	18.198	-14.2 ± 0.2	0.388 [0.255+(0.133)]	<0.0	0.05295 s	^{262g}Bh
						9.020	-13.3 ± 0.3	0.19778 s	^{258}Db
						8.351	-12.9 ± 0.3	0.74263 s	^{254}Lr
						EC			^{250}Md
						7.403	-13.1 ± 0.4	41.07386 m	^{250}Fm
		11	15	18.518	-2.4 ± 0.2	1.679	-2.7 ± 1.7	0.02931 s	^{262}Bh
						8.626	-2.2 ± 0.3	4.97932 s	^{258}Db
						8.405	-5.9 ± 0.3	38.86903 s	^{254}Lr
						EC			^{250}Md
						7.340	-2.3 ± 0.4	15.63662 m*	^{250}Fm

Table 4.4: Decay chains from the ^{209}Bi(^{54}Cr,x*n*)$^{263-x}$Bh reaction. Symbolism is identical to that listed Table 4.3. (Continued on next page.)

E_{COT} (MeV)	E* (MeV)	Event #	Strip #	E_{EVR} (MeV)	Position (mm)	Decay Energy (MeV)	Position (mm)	Lifetime	^{A}Z
264.7	20.2	12	22	21.868	-4.8 ± 0.1	7.995	-4.6 ± 0.4	0.12400 s	^{262g}Bh
						9.160= [1.811+7.349]	-3.2 ± 1.5	0.30739 s	^{258}Db
						8.483= [1.362+7.121]	-3.1 ± 2.1	47.79007 s	^{254}Lr
						EC			^{250}Md
						7.453	-5.1 ± 0.4	40.27928 m*	^{250}Fm
		13	40	18.568	-10.5 ± 0.2	1.336	-15.1 ± 2.1	0.56130 s	^{262g}Bh
						9.307	-10.7 ± 0.3	3.99282 s	^{258}Db
						8.579	-10.7 ± 0.3	17.94719 s	^{254}Lr
		14	38	20.637	-20.4 ± 0.1	10.096	-20.3 ± 0.3	0.10066 s	^{262g}Bh
						9.307	-20.6 ± 0.3	5.42953 s	^{258}Db
						8.477	-20.3 ± 0.3	31.91871 s	^{254}Lr
		15†	39	22.379	-5.6 ± 0.1	9.540= [1.017+8.523]	-11.9 ± 2.8	0.03042 s	^{262m}Bh
						9.115= [1.278+7.837]	-9.0 ± 2.2	8.42168 s	^{258}Db
						EC			^{254}Lr
						8.115= [1.204+6.911]	-9.0 ± 2.3	89.97279 s*	^{254}No
		16	29	21.647	-2.4 ± 0.1	10.383	-2.8 ± 0.3	0.04972 s	^{262m}Bh
						Missing			^{258}Db
						8.506	-2.4 ± 0.3	5.19473 s*	^{254}Lr
						EC			^{250}Md
						7.476	-2.8 ± 0.4	42.39381 s*	^{250}Fm
		17†	37	17.965	-8.8 ± 0.2	10.025= [1.072+8.953]	-14.8 ± 2.6	0.29517 s	^{262g}Bh
						9.116	-9.8 ± 0.3	21.25798 s	^{258}Db
						EC			^{254}Lr
						8.001	-9.0 ± 0.3	45.87513 s*	^{254}No
		18	23	19.176	-26.9 ± 0.1	10.285= [0.960+(0.087)+9.238]	<0.0	0.01954 s	^{261}Bh
						9.198	-27.3 ± 0.3	0.32093 s	^{257m}Db
						8.753	-26.8 ± 0.3	2.31608 s	^{253m}Lr
						8.016	-26.8 ± 0.3	74.32252 s	^{249}Md
						7.797= [1.878+(0.171)+5.748]	<0.0	56.81931 s	^{245}Es

Table 4.4, continued: Observed ^{262}Bh^{g,m} and ^{261}Bh decay chains from the ^{209}Bi(^{54}Cr,x*n*)$^{263-x}$Bh reaction. (Continued on next page.)

E_{COT} (MeV)	E* (MeV)	Event #	Strip #	E_{EVR} (MeV)	Position (mm)	Decay Energy (MeV)	Position (mm)	Lifetime	^{A}Z
268.4	23.2	19	30	17.176	18.1 ± 0.2	0.602= [0.469+(0.133)]	>0.0	0.01239 s	^{261}Bh
						9.081	17.7 ± 0.3	0.71889 s	^{257g}Db
						8.825	18.1 ± 0.3	1.10995 s	^{253g}Lr
		20	27	20.038	-1.8 ± 0.1	10.125	-2.1 ± 0.3	0.13698 s	^{262g}Bh
						9.070	-1.8 ± 0.3	0.18633 s	^{258}Db
						8.445= [0.731+7.714]	-4.9 ± 3.8	12.14193 s	^{254}Lr
						EC			^{250}Md
						7.480	-0.3 ± 0.4	126.90816 m*	^{250}Fm
272.3	26.3	21	36	18.969	-24.0 ± 0.1	10.113	-24.2 ± 0.3	0.01133 s	^{261}Bh
						9.285= [1.202+(0.175)+7.908]	<0.0	0.21316 s	^{257m}Db
						159.9	-23.7 ± 0.0	2.82369 s	^{253m}Lr
		22	35	19.978	1.7 ± 0.1	10.165	1.2 ± 0.3	0.00588 s	^{261}Bh
						9.292	1.1 ± 0.3	0.42672 s	^{257m}Db
						169.0	1.5 ± 0.0	1.23191 s	^{253m}Lr
		23	29	15.408	12.1 ± 0.2	9.989	11.9 ± 0.3	0.01337 s	^{261}Bh
						Missing			^{257m}Db
						8.845= [1.867+6.978]	9.8 ± 1.5	7.59331 s*	^{253m}Lr
						8.116	11.7 ± 0.3	38.92526 s	^{249}Md
						7.637	11.6 ± 0.4	3.73605 m	^{245}Es

Table 4.4, continued: Observed $^{262}Bh^{g,m}$ and ^{261}Bh decay chains from the $^{209}Bi(^{54}Cr,x\textit{n})^{263-x}Bh$ reaction.

a consistent comparison of all the results. The re-calculated cross sections with the appropriate efficiency factors can be seen in Table 4.1, and remain largely unchanged from the original values. We discuss the resulting updated and expanded excitation function in Section 4.5.

The measured half-lives of $^{262}Bh^{m}$ and $^{262}Bh^{g}$ from totals of seven and thirteen alpha decay events are 14^{+8}_{-4} ms and 110^{+41}_{-24} ms, respectively. Both values compare fairly

well to current literature values of 8.0 ± 2.1 ms and 102 ± 26 ms [7, 37, 38]. Our larger error intervals are the result of lower counting statistics than in the GSI studies.

4.3.1.2 ^{258}Db

Fifteen decays of ^{258}Db were observed, and in addition we infer the decay of another one as EC (see Event 16, Table 4.4). The full energy or reconstructed alpha decay energies observed correspond well to the known alpha lines, with few exceptions. Of these sixteen ^{258}Db events only one decayed by EC. This initially surprising result is readily explained by the difficulty in conclusively assigning the EVR-alpha-SF chains produced at bombarding energies above the 2*n* exit channel threshold. These events could be the 1*n* product EVR→^{262}Bh-α→^{258}Db-EC→^{258}Rf-SF, or the 2*n* product EVR→^{261}Bh-α→^{257}Db^{g,m}-α→^{253}Lr^{g,m}-SF. Only the decay chains containing the decay path EVR-alpha-SF produced at bombarding energies below the threshold for the 2*n* product were accepted as assignable decay chains, and the remainder were left unassigned. Because of the low statistics resulting from our selection process, the branching ratio is anomalously small, and we do not report a value. The literature value for the EC branching in ^{258}Db is 0.33. [35] Using seventeen events that are considered decays of ^{258}Db, we calculate a half-life of $3.3^{+1.0}_{-0.6}$ s, consistent with the value of $4.4^{+0.9}_{-0.6}$ s from [35].

4.3.1.3 ^{258}Rf

Only one SF attributed to the decay of ^{258}Rf was identified as an EC daughter of ^{258}Db. Again, because most of the beam energies studied in this work were sufficiently

high to make both the 1*n* and 2*n* products, we have chosen to be conservative in our decay chain assignments in the absence of more conclusive data. It is likely that many SF events we have left unassigned are in fact decays of ^{258}Rf, as mentioned above in the ^{258}Db discussion. This event of ^{258}Rf was produced at a compound nucleus excitation energy of 14.2 MeV, below the threshold for 2*n* exit channel production. No half life is presented here because the lifetime was measured as the sum of the ^{258}Db and ^{258}Rf lifetimes.

In light of the new information about the larger ^{258}Rf alpha decay branch of 0.31 [45] we searched for decay chains involving the EC of ^{258}Db to ^{258}Rf, followed by alpha decay to ^{254}No. This decay path would appear identical to the ^{262}Bh α-^{258}Db α-^{254}Lr EC-^{254}No α decay path, and we indicate the decay chains that could belong to either path in Tables 4.3 and 4.4 with a dagger. This ambiguity in decay path does not affect the cross sections, assignment of *Z* and *A*, or validity of any decay chain.

4.3.1.4 ^{254}Lr

Eleven alpha decays of ^{254}Lr were recorded, and an additional four EC decays are inferred from the decay data. The difference in alpha decay energies between ^{254}Lr (E_α = 8.41, 8.46 MeV) [35] and ^{253}Lr^{m,g} (E_α: ^{253}Lr^{m} = 8.72, ^{253}Lr^{g} = 8.79 MeV) [36] is the most effective way to discern between the 1*n* and 2*n* exit channels in these reactions. Six of the eleven alpha particle energies fit well with the two known alpha transitions. Of the remaining five alpha particle energies, three are of lower energy (decay chains 4, 5, and 10) and two are of higher energy (chains 13 and 16) than these known alpha energies. The mean alpha particle energy is 8.37 MeV for the lower energy group, and 8.54 MeV

for the higher energy group. It is possible that the higher energy group is a result of conversion electron summing.

Using lifetimes from eleven decays that we associate with the alpha decay of ^{254}Lr, we measure a half-life of 11^{+5}_{-3} s, consistent with the literature value of 13^{+3}_{-2} s. [35] We observe EC decay branching of 0.24 ± 0.11, consistent with the literature value of 0.22 ± 0.06. Because of the inability in determining if the decay chain contains the alpha decay of ^{258}Rf, we have made a calculation for the probability of one of our decay chains passing through ^{258}Rf, including the ^{258}Db b_{EC} of 0.33 and the ^{258}Rf b_{α} of 0.31. This results in an expectation that less than one of the four ^{254}Lr EC decays we have assigned is truly an alpha decay of ^{258}Rf.

4.3.1.5 ^{250}Md

Zero alpha decays of ^{250}Md were observed in this work, which is consistent with the large EC branching ratio of 0.93 ± 0.03 [60] for this isotope. However, we were able to infer that ^{250}Md was produced in these reactions because seven of the decay chains contain alpha decays of both ^{254}Lr and ^{250}Fm. No half-life was measured for this isotope, as its lifetime is summed with the next decay in the chain.

4.3.1.6 ^{250}Fm

Eight alpha decays of ^{250}Fm were observed in this work, seven from the EC decay of ^{250}Md, and one from the alpha decay of ^{254}No. The mean alpha particle energy of our eight events is 7.41 MeV, in excellent agreement with the reported alpha particle energy of 7.43 MeV reported in the literature [47]. Because seven of the eight decays of ^{250}Fm

are preceded by an EC decay, we are left with only one lifetime (event 9, Table 4.4) that is not measured as the sum of and EC and alpha decay. The lifetime is 30.37 min. We did not search for decays beyond ^{250}Fm in these 1*n* decay chains of ^{262}Bh.

4.3.2 2*n* Exit Channel

4.3.2.1 ^{261}Bh

Seven decay chains corresponding to the decay of ^{261}Bh were observed in this work. All chains but one contained full-energy events for the decay of ^{261}Bh. The alpha particle energies match well with known lines, with the exception of event 23 of Table 4.4, at 10.29 MeV. The half life calculated from twelve decays is $9.2^{+3.6}_{-2.0}$ ms, corresponding well to the values of $11.8^{+5.3}_{-2.8}$ ms and 10^{+14}_{-5} ms [37, 38]. No SF events or decay chains resembling the EC of ^{261}Bh to ^{261}Sg were observed.

4.3.2.2 ^{257}Db^{g}, ^{257}Db^{m}

Seven alpha decays of ^{257}Db were observed in this work: three of the ground state isomer, and four of the metastable state isomer. The alpha decays of ^{257}Db^{g} consist of a full-energy signal fitting the known ground state alpha particle energy, and two escapes. Three of the four ^{257}Db^{m} alpha decays are either full energy or reconstructed events in the focal plane detector, and the fourth is a "missing" escape. One of the three metastable state alpha decay energies matches well with the known alpha line from the literature [36], and the two remaining alpha decay energies (events 21 and 22 in Table 4.4) may represent a new transition. They are identical in energy, at 9.29 MeV and have very similar lifetimes. The half-lives for the ground and metastable states are $1.8^{+1.0}_{-0.5}$ s and

$0.31^{+0.28}_{-0.10}$ s, calculated from seven and four alpha decays, respectively, and they are in somewhat good agreement with the literature values of $1.5^{+0.19}_{-0.15}$ s and $0.76^{+0.15}_{-0.11}$ s.

Both the ground and metastable states of ^{257}Db have small SF branches of 0.013 and 0.08, respectively [36]. Because of our conditions on decay chain event assignments, we have excluded the ^{261}Bh-α-^{257}Db^{g,m}-SF decay path options, as they would be easily confused with the ^{262}Bh^{g,m}-α-^{258}Db-EC-^{258}Rf-SF decay path. For this reason, we do not report on the branching ratios of ^{257}Db^{g,m}.

4.3.2.3 ^{253}Lr^{g}, ^{253}Lr^{m}

The alpha decay granddaughter of ^{261}Bh, ^{253}Lr^{g,m}, was observed in these experiments as well. As was the case with ^{257}Db, we observed three ground state and four metastable state decays. Two of the three ground state decays were alpha decays, one with a previously known energy of 8.79 MeV, and one with a new, slightly higher energy of 8.83 MeV. The third of the three decays was a reconstructed SF of 190.7 MeV. Two of the four metastable state decays were alpha decays, again one of a known energy of 8.73 MeV, and one at a slightly higher energy of 8.85 MeV. These two decays of higher energies than the literature values could also be attributed to additional energy from summed conversion electron signals. The remaining two decays were SF of 159.9 and 169.0 MeV. In contrast to the decay of ^{257}Db, we have chosen to accept SF decays that were preceded by an EVR and alpha decay since there is not a similar decay path in ^{262}Bh, making conclusive assignment possible.

From three events each of the ground and metastable states we calculate half-lives of $0.38^{+0.45}_{-0.13}$ s and $1.47^{+1.75}_{-0.52}$ s, respectively. These values compare well with the literature

values of $0.57^{+0.07}_{-0.06}$ s and $1.49^{+0.30}_{-0.21}$ s [36]. We observe that the alpha decay of ^{257}Db to ^{253}Lr proceeds from ground state to ground state or metastable state to metastable state with no cross-correlations. Heßberger *et al*. proposed this decay scheme in [36], and our results agree.

4.3.2.4 ^{249}Md, ^{245}Es

Two of the seven decay chains attributed to ^{261}Bh extended as far as ^{245}Es. Events 18 and 23 in Table 4.4 show these chains passing from ^{253}Lr^{m} via alpha decay to ^{249}Md, which has $b_\alpha = 0.20 \pm 0.10$ and a half-life of 24 s [60]. These decay chains continue via alpha particle emission to ^{245}Es, with has $b_\alpha = 0.40 \pm 0.10$ and a half-life of 1.1 min [60]. Our measured ^{249}Md and ^{245}Es half-lives are $39.5^{+71.0}_{-15.4}$ s and $1.6^{+2.9}_{-0.6}$ min, respectively, in agreement with the literature. The observed alpha particle energies of our ^{249}Md and ^{245}Es events agree fairly well with the literature values [60]. The only discrepancy is one ^{249}Md alpha decay at an energy ~90 keV greater than previously reported. The suggestion of an alpha-decaying isomer in ^{249}Md was made in [36]. Our two alpha decays seem to support that hypothesis, but more data would be needed to certify it.

4.3.3 Spontaneous Fission of ^{262}Bh

There was also one EVR-SF correlation observed in this work. The decay occurred at a beam energy corresponding to a compound nucleus excitation energy of 17.2 MeV, in focal plane strip number eighteen which is near the center of the detector. The event consisted of an EVR pulse height (uncorrected for pulse height defect) of 17.78 MeV followed 737 μs later by a 203 MeV SF registering signals of 176 + 27 MeV

(FPD and upstream detectors, respectively). The relatively low excitation energy indicates ^{262}Bh because a) E^* = 17.2 MeV, only 2.4 MeV over the threshold for the ^{209}Bi(^{54}Cr,2n)^{261}Bh reaction, and b) production of ^{262}Sg via ^{209}Bi(^{54}Cr,p) is unlikely because of the Coulomb barrier against proton emission. This EVR-SF could indicate direct fission of ^{262}Bh. However, we have calculated an SF hindrance factor of ≤ 26 from an interpolation of the partial SF half-lives for ^{260}Sg and ^{264}Hs [74]. This value is several orders of magnitude smaller than what would be expected based on the two odd particles in ^{262}Bh. A more speculative interpretation of this event could be electron-capture delayed-fission (ECDF) in ^{262}Bh^{m}. The Q-value for the EC is approximately 5.9 MeV [73], corresponding to a large probability for delayed fission (see Fig. 4 of [75]). Because of the uncertainty in the nature of this chain, we have excluded it from cross section and half-life calculations.

4.4 Random Event Analysis

A random event correlation analysis was conducted for this work, similar in method to the one described in Section 3.4. Again, 65 seconds, five times the literature half-life value of ^{254}Lr, was chosen to be the maximum time of decay chain consideration because ^{254}Lr is crucial to distinguishing the 1n and 2n exit channel products. This time interval covers the decay of Bh, Db, Lr, and No. Alpha-like events were required to have energies between 8.0 – 11.0 MeV, and EVR-like events were required to have energies between 8.0 – 24.0 MeV. The defined pixel size was the same as defined in Section 2.2.4, 1.5 mm between two events in a single strip. Since no decay chains were identified by an EVR correlated to only two alpha decays, the calculations were carried out for

EVR–α–α–α correlations. The number of random chains expected over the duration of each experimental beam energy over both experiments from an EVR followed by three alpha-like events was fewer than $1.3 \cdot 10^{-3}$, and much lower for EVRs followed by greater than three alpha-like events. Individual values for each energy are listed in Table 4.5.

Reaction	E_{COT} (MeV)	E* (MeV)	Probability of Random EVR–α–α–α Correlation
$^{55}Mn + ^{208}Pb$	273.0	21.4	$7.29 \cdot 10^{-4}$
	278.0	25.3	$8.78 \cdot 10^{-4}$
	283.0	29.3	$6.64 \cdot 10^{-4}$
$^{54}Cr + ^{209}Bi$	253.5	11.3	$3.14 \cdot 10^{-5}$
	257.1	14.2	$1.85 \cdot 10^{-5}$
	260.9	17.2	$1.53 \cdot 10^{-4}$
	264.7	*20.2*	*$1.33 \cdot 10^{-3}$*
	268.4	23.2	$1.77 \cdot 10^{-4}$
	272.3	26.3	$3.56 \cdot 10^{-4}$

Table 4.5: Calculated random rate probabilities for $^{55}Mn + ^{208}Pb$ and $^{54}Cr + ^{209}Bi$ experiments. Highest probability of all results italicized.

4.5 Excitation Functions and Discussion

4.5.1 Excitation Function for $^{208}Pb(^{55}Mn,xn)^{263-x}Bh$

The excitation function measured in the $^{208}Pb(^{55}Mn,xn)^{263-x}Bh$ reaction can be seen in Figure 4.1, with a Gaussian-exponential fit from a maximum likelihood fit method as described in Section 2.2.5. This combination of a Gaussian and exponential function simply yet accurately reproduces the known general shape of excitation functions. The fit incorporates weighting for numbers of events, cross sections, and also energy spread through the target, which correctly accounts for the variation in cross

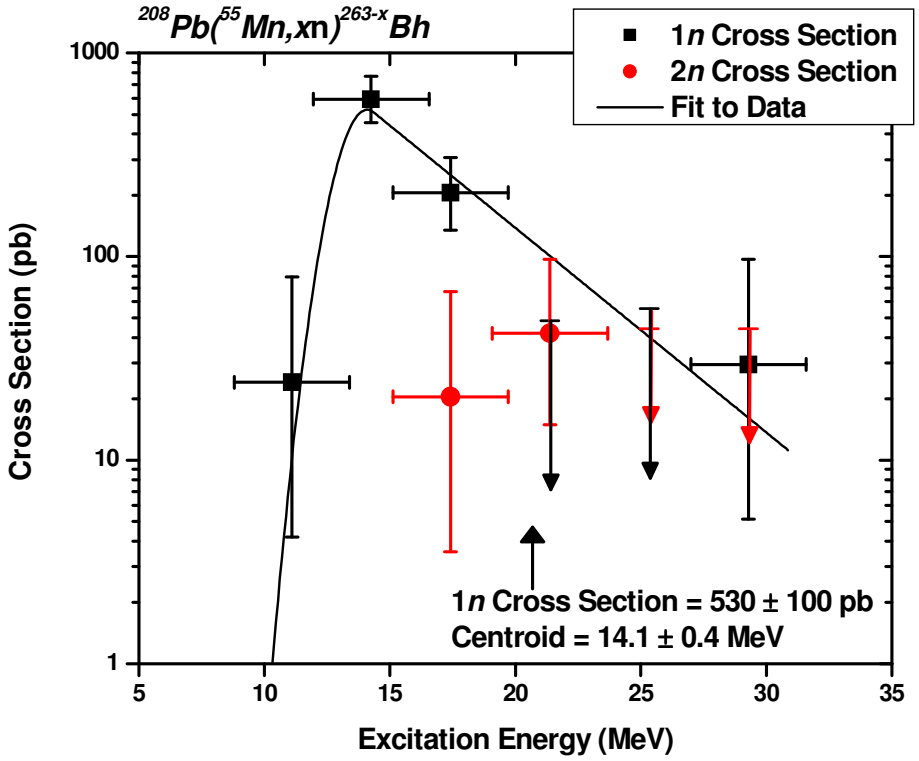

Figure 4.1: Measured excitation function for the ^{208}Pb(^{55}Mn,xn)$^{263-x}$Bh reaction. Points from the 1n and 2n exit channels are indicated by filled black squares and filled red circles, respectively. A fit to the data as in [69] is indicated by the solid black line.

section over the target's energy thickness. The use of such fits allows us to obtain accurate values of cross sections and energies at the peak of the excitation function.

For the fit to the ^{55}Mn + ^{208}Pb data, parameters w (Gaussian width) and λ (exponential slope) were fixed at values of 1.349 and 0.183, respectively. These two values were obtained from a fit to the ^{208}Pb(^{48}Ti,n)^{255}Rf reaction in [69] that possessed high statistics and multiple bombarding energies. We are confident that they are applicable in this work, and enabled a better fit to the data than when all parameters were allowed to vary. In the fit to the ^{54}Cr + ^{209}Bi reaction data, Figure 4.2, the parameters w

and λ were allowed to vary, settling at 2.34 and 0.43, respectively. The values for *w* and λ have little effect on the centroid and amplitude in the fits.

In Figure 4.1 the filled black squares represent data points for the 1*n* exit channel, filled red circles the 2*n* exit channel. Upper limits for each exit channel are denoted by a downward facing arrow. The black arrow on the abscissa indicates the location of the Coulomb barrier as calculated by the FBD model [29, 30, 32]. The vertical error bars represent statistical counting error, the horizontal error bars indicate the energy loss in the beam as it traverses the target.

The three points lowest in energy in Figure 4.1 represent the re-evaluated data from Folden [37], with new alpha chain detection efficiency factors applied. It is interesting to note the large cross section in the three points at the lowest energies, followed by two upper limits, and then one decay chain at the highest energy. The maximum observed 1*n* cross section for this reaction is 590^{+170}_{-140} pb at 264.0 MeV ($E_{lab, COT}$), which corresponds to a compound nucleus excitation energy of 14.3 MeV. The fit yields a similar but slightly reduced cross section of 530 ± 100 pb at an excitation energy of 14.1 ± 0.4 MeV. The location of the FBD barrier for this reaction is 20.6 MeV, approximately 6.3 MeV higher than the peak of the excitation function fit.

We begin to see the onset of the 2*n* exit channel around a compound nucleus excitation energy of 17 MeV. This is where one would expect the ingrowth of the 2*n* excitation function, but we were only able to observe this product at two of the experimental beam energies. Additional experiments with higher bombarding energies would be required to observe the turnover and determine a maximum 2*n* cross section.

At this time it appears there may be a maximum 2*n* cross section of approximately 40 pb, but in the absence of additional data this number is speculation only.

4.5.2 Excitation Function for ^{209}Bi(^{54}Cr,x*n*)$^{263-x}$Bh

The excitation function for the other reaction of this pair, ^{209}Bi(^{54}Cr,x*n*)$^{263-x}$Bh is shown in Figure 4.2, and has the same symbolism as shown in Figure 4.1. In the fit to these reaction data, the parameters *w* and λ were allowed to vary within constraints, settling at 2.34 and 0.43, respectively.

A maximum observed cross section of 440^{+430}_{-240} pb at 260.9 MeV ($E_{lab,\,COT}$) or a compound nucleus excitation energy of 17.2 MeV was observed when data from the three experimental runs were combined. The fit of these 1*n* data points yields a cross section of 430 ± 110 pb at a compound nucleus excitation energy of 15.7 ± 0.5 MeV. The location of the barrier from the FBD model is at 18.7 MeV, approximately 3 MeV greater than the maximum of the fit.

The partial excitation function for the 2*n* exit channel of the ^{54}Cr + ^{209}Bi reaction has no clear maximum based on our observations at this time. The three data points corresponding to the 2*n* product continue to increase in magnitude with an increase in beam energy. Though we have not observed a peak, we can say that it is unexpectedly large; likely a minimum of twice the magnitude of the maximum observed 2*n* cross section in the ^{55}Mn + ^{208}Pb reaction, based on current data.

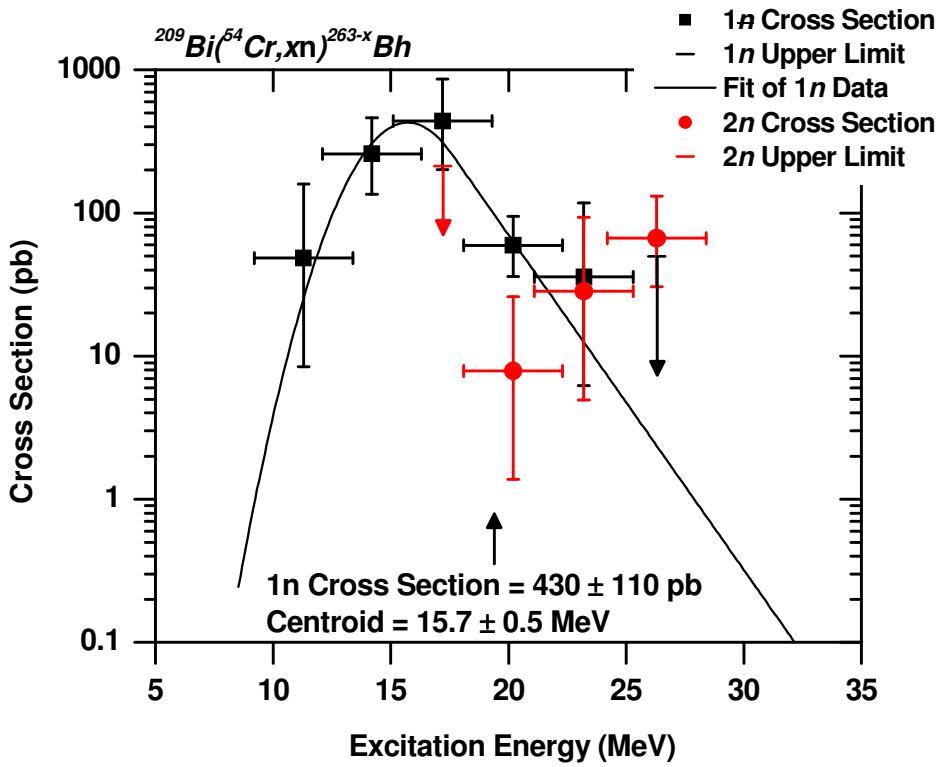

Figure 4.2: Measured excitation function for the ^{209}Bi(^{54}Cr,x*n*)$^{263-x}$Bh reaction Symbolism is identical to Figure 4.1.

4.5.3 Comparisons of Excitation Functions

The 1*n* excitation functions for the ^{55}Mn + ^{208}Pb and ^{54}Cr + ^{209}Bi reactions can be seen together in Figure 4.3. It is interesting to note that the ^{208}Pb(^{55}Mn,*n*)^{262}Bh reaction has a slightly higher cross section (errors notwithstanding) than the ^{209}Bi(^{54}Cr,*n*)^{262}Bh reaction, which is the opposite of what would be expected based on the long-standing effective fissility rationale and the predictions from the "Fusion By Diffusion" model. We have calculated the values for the effective fissility of these reactions, and they are $x = 0.847$ and 0.849 for the ^{54}Cr + ^{209}Bi and ^{55}Mn + ^{208}Pb reactions, respectively, with

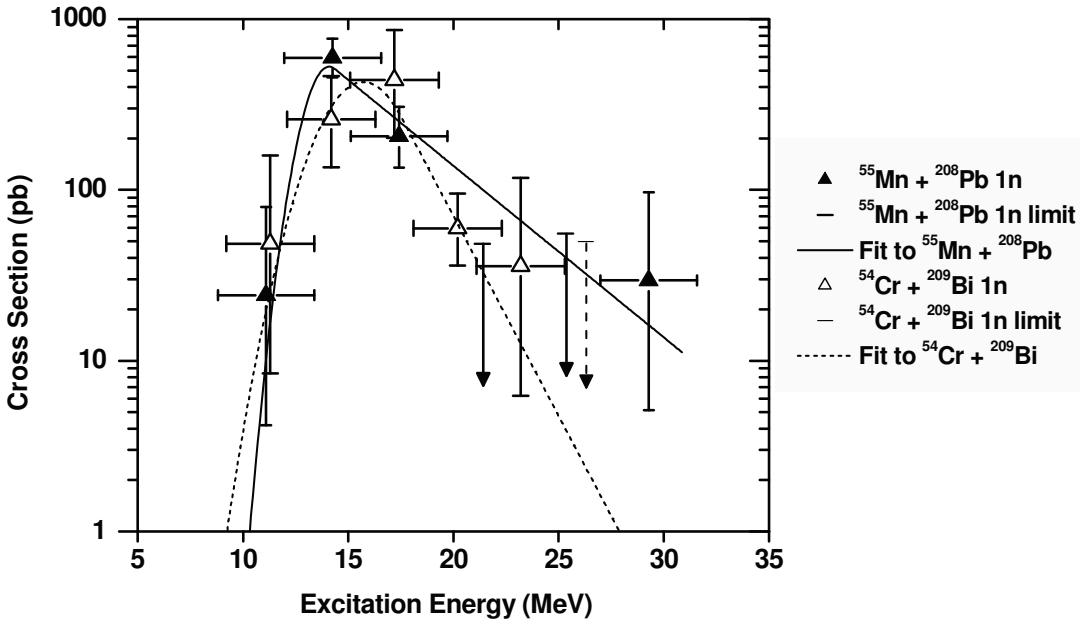

Figure 4.3: A side-by-side comparison of the 1*n* excitation functions from the ^{208}Pb(^{55}Mn,*n*)^{262}Bh and ^{209}Bi(^{54}Cr,x*n*)^{262}Bh reactions. Filled and open triangles represent the measured ^{55}Mn + ^{208}Pb and ^{54}Cr + ^{209}Bi 1*n* cross sections, respectively. The solid and dashed lines represent each reaction's respective fit.

$\Delta x = 0.002$. Though the fissility values might suggest that the Bi-based reaction should have a higher cross section because of the lower effective fissility, they are so close in value that we assert no real conclusion may be drawn from this argument alone.

The ratio of the ^{55}Mn/^{54}Cr 1*n* cross sections' fit maxima is 1.2 ± 0.4, a small number. These data and the results of our fits suggest that the effect of the entrance channel on cross section magnitudes may not be as great as initially thought. Compared directly, the large overlap of vertical statistical error bars suggests there is no difference in cross section. With longer irradiation times and more observed decay chains the

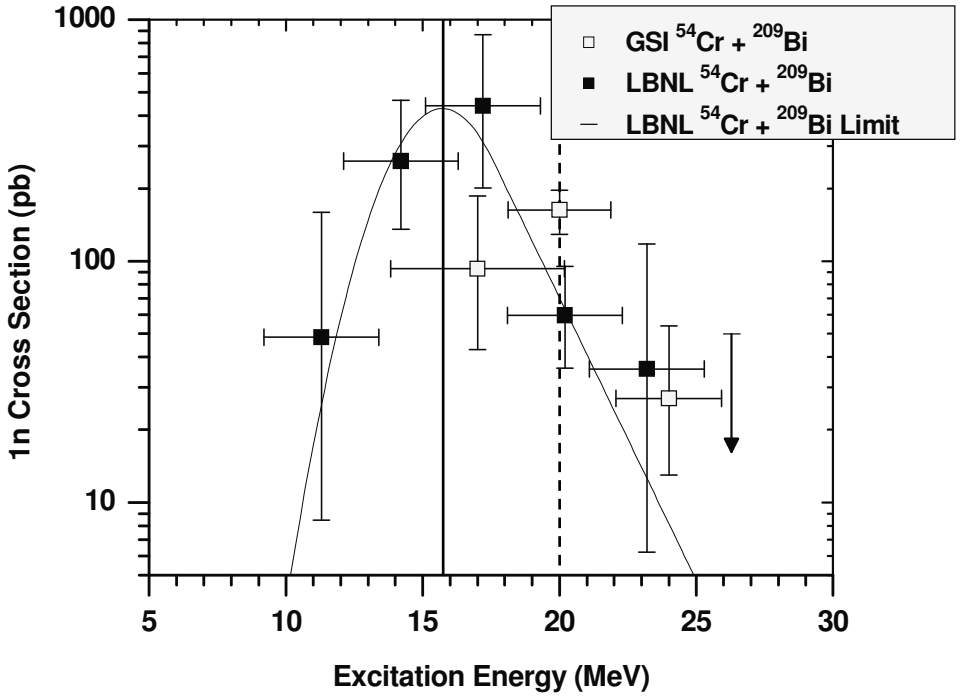

Figure 4.4: Measured excitation functions for the ^{209}Bi(^{54}Cr,*n*)^{262}Bh reaction, studied at LBNL and GSI [7, 38] . Open squares represent data from GSI, filled squares from this work, a horizontal dash represents our upper limit, and the solid line along the filled squares is the fit from the maximum likelihood method. Vertical solid and dashed lines indicate position of each reaction's peak for comparison.

statistical error would be reduced, potentially identifying one of the reactions as having a higher cross section.

A plot of our 1*n* excitation function for the ^{54}Cr + ^{209}Bi reaction alongside the previous work from GSI is presented in Figure 4.4. The filled squares represent the data from our study, and the open squares represent the GSI data. Error bars are as discussed previously. The solid and dashed vertical lines represent the peaks of the 1*n* exit channel for our work and the GSI work, respectively. The GSI data generally agree with that from the present work.

4.5.4 Comparisons to Model Predictions

We also compare our results to the FBD model [29, 30, 32] predictions provided to us by W.J. Świątecki. The ^{55}Mn + ^{208}Pb reaction was predicted a few years earlier to have a cross section of approximately 100 pb, which has been recently updated to 400 pb based on a re-parameterized model [32]. We find that this value compares well to the 530 ± 100 pb observed in this work. The centroids of the experiment and prediction compare well also, with our fit yielding a peak at an excitation energy of 14.1 ± 0.4 MeV, compared to the 14 MeV from the prediction. Similarly, we compare the results of our ^{54}Cr + ^{209}Bi reaction to predictions, and we see a peak cross section of 430 ± 110 pb at 15.7 ± 0.5 MeV, comparing somewhat well to the prediction of 500 pb at ~13.5 MeV. While the cross sections are fairly close, the centroid of the predicted value is approximately 2 MeV too low. Overall, we find that the FBD model predictions reproduce peak 1*n* cross sections well within a factor of two.

It is also interesting to compare the large differences in 1*n* cross sections in reaction systems differing only by two neutrons in the projectile. The ^{209}Bi(^{54}Cr,*n*)^{262}Bh / ^{209}Bi(^{52}Cr,*n*)^{260}Bh is one such reaction pair. The FBD model predicts the reaction with the heavier projectile is expected to exhibit the larger cross section. A cross section of 59 pb in the ^{209}Bi(^{52}Cr,*n*)^{260}Bh reaction was measured and more detailed information can be found in Chapter 5. The 430 pb measured in this work results in a ^{209}Bi(^{54}Cr,*n*)^{262}Bh / ^{209}Bi(^{52}Cr,*n*)^{260}Bh cross section ratio of $7.3^{+0.8}_{-0.6}$. This supersedes an earlier report of this ratio of 8.2 in a previous paper and we now present finalized results here. Previously no such ratios had been measured in an odd-*Z* TAN system, and this experimental cross section ratio is close to the cross section ratio of 10 predicted by

Świątecki [32]. The resulting lower cross section in the lighter reaction is likely an entrance channel effect due to the lighter reaction being more sub-Coulomb barrier than the heavier reaction, and we look forward to additional results on these reactions differing only by two projectile neutrons to see if this effect is observed elsewhere [69].

5. Production of the New Isotope ^{260}Bh in the ^{209}Bi(^{52}Cr,n) Reaction

The majority of the work in this dissertation is concerned with a systematic study of paired reactions to produce odd-*Z* transactinide elements in an attempt to determine any preference of entrance channel. The work in this chapter is an exception, as it studies the production of a new transactinide isotope and its previously unknown decay properties.

5.1 Previous Work

5.1.1 Dubna Experiment

The only previous work known on the isotope ^{260}Bh was done in 1983 by Oganessian and coworkers at the JINR in Dubna, Russia [76]. They used a cold fusion-type reaction of ^{206}Pb(^{55}Mn,*n*)^{260}Bh with the same cylindrical mica track detector as described in Chapter 3.1.1. They claimed a half-life of 2.6 seconds for the alpha decay of ^{260}Bh to ^{256}Db, which then electron captured to ^{256}Rf and decayed by spontaneous fission. They also reported a 500 pb cross section based on these SF observations. We know from separate experiments that ^{256}Db does undergo EC [36] and ^{256}Rf does decay mostly by SF [35, 77], and the sum of these half-lives is nearly 2.6 seconds, so they may have indeed produced and observed this lightest bohrium isotope. However, these data could not conclusively identify the *Z* or *A* of the product, and these results were only available

as a JINR internal report and not in the peer-reviewed literature. The existence of ^{260}Bh has, until now, been accompanied with a question mark.

5.1.2 Motivation for Additional Studies

The uncertainty of this only work on ^{260}Bh led to curiosity about what would be observed if another experiment were conducted. Our study would be greatly benefited by the advances in technology such as magnetic rigidity separators and charged-particle detectors. During the course of one experiment to study the ^{209}Bi(^{54}Cr,x*n*)$^{263-x}$Bh reaction for the work in Chapter 4, extra experimental beam time was made available. This beam time was far in excess of what had been planned for when the enriched ^{54}Cr isotope was purchased, and therefore we could not run that experiment for the duration of the additional time. It was decided that we would leave the ^{209}Bi target wheel in place, and use the most naturally abundant chromium isotope, ^{52}Cr, in a search for ^{260}Bh.

The results of this new study were recently published in the peer-reviewed literature [51].

5.2 Experimental Conditions

Masses from the 2003 Atomic Mass Evaluation by Audi *et al.* [78] were used to estimate the *Q*-values for various decay modes. ^{260}Bh should decay by alpha emission and possibly by SF or electron capture (EC). The predicted ground-state to ground-state alpha decay *Q*-value is 10.46 MeV, resulting in an expected alpha particle energy of 10.30 MeV and an unhindered half-life of 490 μs [79]. The known decay properties of

the subsequent ^{256}Db [36], ^{256}Rf [35, 77], ^{252}Lr [36], ^{248}Md [46], and ^{248}Fm [60] daughter products are illustrated in Figure 5.1(a).

The beam energy was chosen based on the optimum energy rule by Świątecki *et al.* [29, 30]. Using tabulated mass defects from Audi *et al.* [78] and an additional experimentally determined offset between 1-3 MeV for odd-*Z* compound nuclei [33] (chosen to be 1.8 MeV for this experiment), the center-of-mass beam energy in the center of the target was calculated to be 202.4 MeV. This corresponds to a compound nucleus excitation energy of 15.0 MeV, and is below the threshold for production of ^{259}Bh via the 2*n* evaporation channel.

The BGS was used in its standard configuration with the MWPC installed, similar to the configuration described in Section 3.2 and 4.2. The LBNL 88-Inch Cyclotron accelerated a 257.0 MeV beam of $^{52}Cr^{12+}$ with an average intensity of 0.4 pμA. The beam first passed through the thin carbon foil used for vacuum separation. The beam then impinged upon our rotating ^{209}Bi target wheel. Energy loss of the ions through the system was calculated using the program SRIM-2003 [53]. The target wheel rotation speed was approximately 5-10 Hz. The alpha particle energy resolution for implanted nuclei was 55-keV FWHM, determined from a ^{173}Yb(^{30}Si,6*n*)^{197}Po reaction run two weeks prior to this experiment.

The reaction products recoiled out of the thin targets with the momentum of the beam and into the 67 Pa He gas of the BGS. The average evaporation residue (EVR) charge state was calculated to be 7.8 [55]. The BGS magnet currents were chosen to direct the ^{260}Bh recoils with a magnetic rigidity of 2.15 T·m [55] to the FPD. Monte

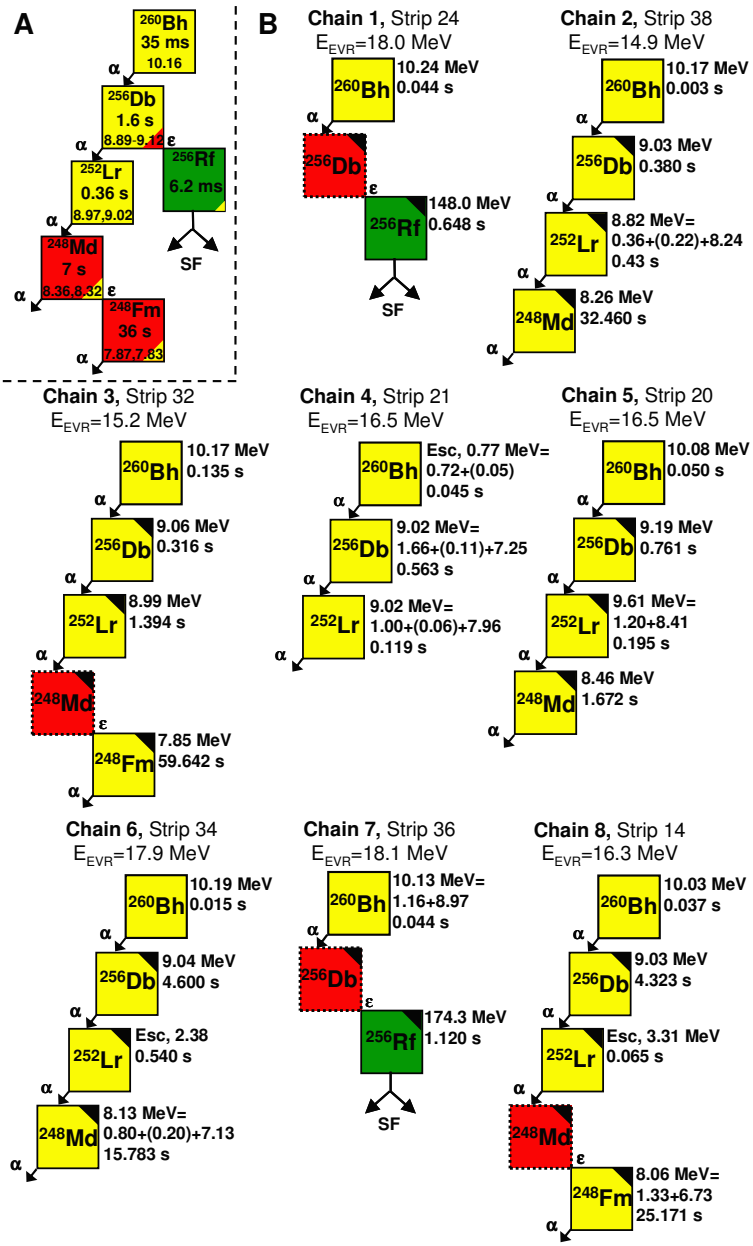

Figure 5.1(a) - Decay properties of ^{260}Bh and its previously known daughter nuclides [35, 36, 46, 77]. (b) - Observed ^{260}Bh decay chains. Reconstructed energies are listed with the focal plane energy listed first, followed by the calculated energy from a missing signal from either the top or bottom of the strip in parentheses, ending with the energy deposited in the upstream detector (see text). A black triangle in the upper right corner indicates decay was observed during a beam-off interval. Lifetimes of decays following EC are the sum of the two lifetimes. Energies are given in MeV.

Carlo simulations of EVR trajectories in the BGS, as in [55], indicate a total separator efficiency of 0.65 ± 0.06.

During the irradiations, the rate of "EVR-like events" (8.0 < E(MeV) < 24.0, coincident with MWPC signals and anticoincident with upstream or punchthrough detectors) was 0.3 Hz. The rate of "α-decay like events" (8.0 < E(MeV) < 11.0, focal plane only or reconstructed from focal plane plus upstream detector, anticoincident with punchthrough detector and MWPC) was $4.9 \cdot 10^{-3}$ Hz. ^{260}Bh was identified by detection of time- and position- correlated event chains corresponding to EVR implantation followed by the α-decay of ^{260}Bh and ^{256}Db (and possibly ^{252}Lr), or α-decay of ^{260}Bh followed by the SF of ^{256}Rf, the EC daughter of ^{256}Db. To minimize the contribution of random correlation of unrelated events, a fast beam-shutoff scheme was employed. Upon detection of an EVR-like event followed by a position- and time-correlated (within 3σ and 10 s, respectively) ^{260}Bh-α-decay-like event, the beam was switched off for 180 s to allow a background-free search for any daughter-like decays.

During the irradiations, the rate of "EVR-like events" (8.0 < E(MeV) < 24.0, coincident with MWPC signals and anticoincident with upstream or punchthrough detectors) was 0.3 Hz. The rate of "α-decay like events" (8.0 < E(MeV) < 11.0, focal plane only or reconstructed from focal plane + upstream detector, anticoincident with punchthrough detector and MWPC) was $4.9 \cdot 10^{-3}$ Hz. ^{260}Bh was identified by detection of time- and position- correlated event chains corresponding to EVR implantation followed by the α-decay of ^{260}Bh and ^{256}Db (and possibly ^{252}Lr), or α-decay of ^{260}Bh followed by the SF of ^{256}Rf, the EC daughter of ^{256}Db.

5.3 Observed Decay Chains of ^{260}Bh

5.3.1 ^{260}Bh

Figure 5.1(b) contains the eight observed decay chains attributed to the decay of ^{260}Bh. Some focal plane events had below-threshold energies from either the top or bottom of the strip. If these "single-ended" events are part of a decay chain, the missing energy from the below-threshold signal can be calculated from the signal from the above-threshold end of the strip by assuming the vertical position is the same as other members of the event chain. These calculated missing energies are denoted by parentheses in Figure 5.1(b).

Full energy alpha decays were recorded for seven of the eight ^{260}Bh alphas. The remaining ^{260}Bh decay, in chain number 4, was an "escape," registering only 770 keV in the focal plane. In addition, a ninth chain was observed as an implantation followed by two escapes, an alpha decay of 9.04 MeV, and another escape. This chain could be attributed to the decay of ^{260}Bh but is not included in these results because of its uncertain nature. Half-life and cross section errors were treated as a special case of the Poisson distribution as in [63]. Using the eight alpha decay lifetimes, the half-life of ^{260}Bh was found to be 35^{+19}_{-9} ms. No direct spontaneous fissions or SF resulting from the EC decay of ^{260}Bh to ^{260}Sg were observed, and we assign an upper limit of <0.18 at the 84% confidence level for the sum of SF and EC branches.

There is evidence of a grouping of four alphas (from chains 2, 3, 6, and 7) between 10.13-10.19 MeV, with a mean alpha particle energy of 10.16 MeV. There is also one event each at 10.24, 10.08, and 10.03 MeV. Many alpha particle energies are feasible due to possible population of different states in the odd-odd ^{256}Db daughter. The

corresponding alpha decay hindrance factor for the 10.16 MeV group based on the four decays comprising that group is approximately 53 [79].

5.3.2 ^{256}Db

Six alpha decays of ^{256}Db were observed and two electron capture decays were inferred in this experiment. The observed data are in good agreement with decay data previously reported [36]. A weighted mean of the alpha branch from previous work and our current findings results in a ^{256}Db alpha decay branch of 0.70 ± 0.11.

5.3.3 ^{256}Rf

The two spontaneous fissions observed in this experiment were the result of production of ^{256}Rf, the EC daughter of ^{256}Db (chains 1 and 7). ^{256}Rf decays by SF with a branching of >0.98 [35, 77]. No half-life is presented because the lifetime is measured as the sum of the ^{256}Rf spontaneous fission and the preceding ^{256}Db electron capture.

5.3.4 ^{252}Lr

Six alpha decays of ^{252}Lr were observed as the granddaughter decay of ^{260}Bh. The half-life of these events is $0.27^{+0.18}_{-0.08}$ s. The ^{252}Lr alpha particles in chains 6 and 8 escaped the focal plane detector, registering 2.39 and 3.31 MeV, respectively. The 8.99 and 9.02 MeV decays in chains 3 and 4 fit well to the known alpha decay groups at 8.974 MeV and 9.018 MeV, respectively [36]. The remaining decays at 8.82 and 9.61 MeV (chains 2 and 5, respectively) have different energies than any group previously observed in the alpha decay of ^{252}Lr, and may represent new alpha lines. It is important to note that

the highest energy decay, 9.61 MeV, in decay chain 5, is 0.5 MeV higher than that from the expected *Q*-value for this decay [15]. Careful examination of the data supports that it is a valid alpha decay of ^{252}Lr and a member of a ^{260}Bh decay chain, but at this time we are unable to explain this high energy further. No SF decays or alpha decays resembling ^{252}No were observed, supporting earlier claims [17] contending ^{252}Lr decays by alpha emission only.

5.3.5 ^{248}Md, ^{248}Fm

^{248}Md, the alpha decay great-granddaughter of ^{260}Bh, was observed to decay both by electron capture to ^{248}Fm and through alpha emission to ^{244}Es in this experiment. Five of the six alpha decay chains passed through ^{248}Md. Three of these five events decayed by emission of alpha particles of 8.26, 8.46, and 8.13 MeV (chains 2, 5, and 6, respectively). The total ^{248}Md half-life from the three alpha events is 13^{+15}_{-4} s, consistent with 7 ± 3 s [46]. This results in a 0.58 ± 0.20 alpha decay branch in contrast to the 0.20 branch reported in previous work, the apparent discrepancy may be due to the low counting statistics in our study. The relatively high ^{248}Md alpha energy of 8.46 MeV was observed to follow the 9.61 MeV decay of ^{252}Lr. These correlated high-energy transitions could be interpreted in terms of isomerism in ^{252}Lr and ^{248}Md, however, in the absence of data such as gamma spectra, we do not suggest any level schemes. Two events correlating to the alpha decay of ^{248}Fm were observed in this work (chains 3, 7), following the EC decay of ^{248}Md. The two events registered alpha decay energies of 7.85 and 8.06 MeV. The half-life for this isotope cannot be determined directly because its lifetimes were measured as the sum of the ^{248}Md and ^{248}Fm lifetimes.

5.4 Random Event Analysis

A random event correlation analysis was conducted for this work, similar in method to the one described in Section 2.2.4. The maximum time of event consideration was chosen to be 35 seconds, a multiple of five times the longest literature value for the half-life of ^{248}Md. The focal plant event rates, R_α and N_{EVR} for the rate of alpha-like events and number of EVR-like events, respectively, were determined by integrating over their spectra. The total time of experimental data acquisition was 123,980 seconds. Alpha-like events were required to have energies between 7.5 - 11 MeV, and EVR-like events were required to have energies within the same energy gates used in the online shutoff conditions. The number of random chains expected over the duration of the experiment from an EVR followed by two alpha-like events was $1.2 \cdot 10^{-3}$, and much lower for EVR-SF chains or EVRs followed by greater than two alpha-like events. Therefore, we conclude that the multiple sequential alpha decay chains observed in this work are true events of the new isotope ^{260}Bh and not random correlations.

5.5 Discussion

We found the experimental magnetic rigidity of the EVRs to be 2.14 T·m and the corresponding charge state to be 7.8, close to our predicted values. The total integrated beam dose was $1.7 \cdot 10^{17}$ ions. The measured cross section from these eight decay chains of ^{260}Bh is 59^{+29}_{-20} pb. This cross section calculation includes a 0.97 efficiency for detection of a decay chain, calculated using the same method as described in Section 2.2.3.2. We have defined these decay chains as an EVR correlated in time and position to a minimum of two full-energy alpha decays or an SF decay.

5.5.1 Comparison to Model Prediction

This cross-section is nearly a factor of four greater than a theoretical prediction by W. J. Świątecki from the FBD model [29, 30] of 15 pb at an energy of approximately 202 MeV in the center-of-mass frame. Very recently, a new prediction utilizing a re-parameterized model was provided to us with a theoretical cross section of 48 pb at a center-of-mass energy of 202.5 MeV [32], comparing very well to the experimental data point. Because only one bombarding energy was studied in this work, it is not known if 59^{+29}_{-20} pb is the peak of the ^{209}Bi(^{52}Cr,*n*) excitation function. Therefore, it would be beneficial to continue this study by exploring the same reaction at additional energies to map the entire excitation function.

5.5.2 Evidence of Shell Effects

There is also evidence for the influence of the deformed $N = 152$ shell on the alpha decay energies in this region of the Bh isotopes. Among the $N = 153$-155 isotones, the $N = 154$ isotones possess the largest alpha decay energies as a result of decaying into the $N = 152$ shell. This value is approximately 150-340 keV greater than the $N = 153$ or $N = 155$ members' alpha decay energies. The isotopes of Bh follow this trend as well, with the ^{260}Bh major alpha group decaying with an energy of 10.16 MeV, ^{261}Bh with 10.40 MeV, and the ground state isomer of ^{262}Bh with 10.06 MeV, for the $N = 153$-155 isotopes, respectively. This effect can also be observed in Figure 5.2, as the ^{260}Bh data point drops in alpha energy compared to its heavier neighboring isotopes. In the absence of the $N = 152$ shell a smooth decrease in Q_α with increase in N is expected. Prior to this

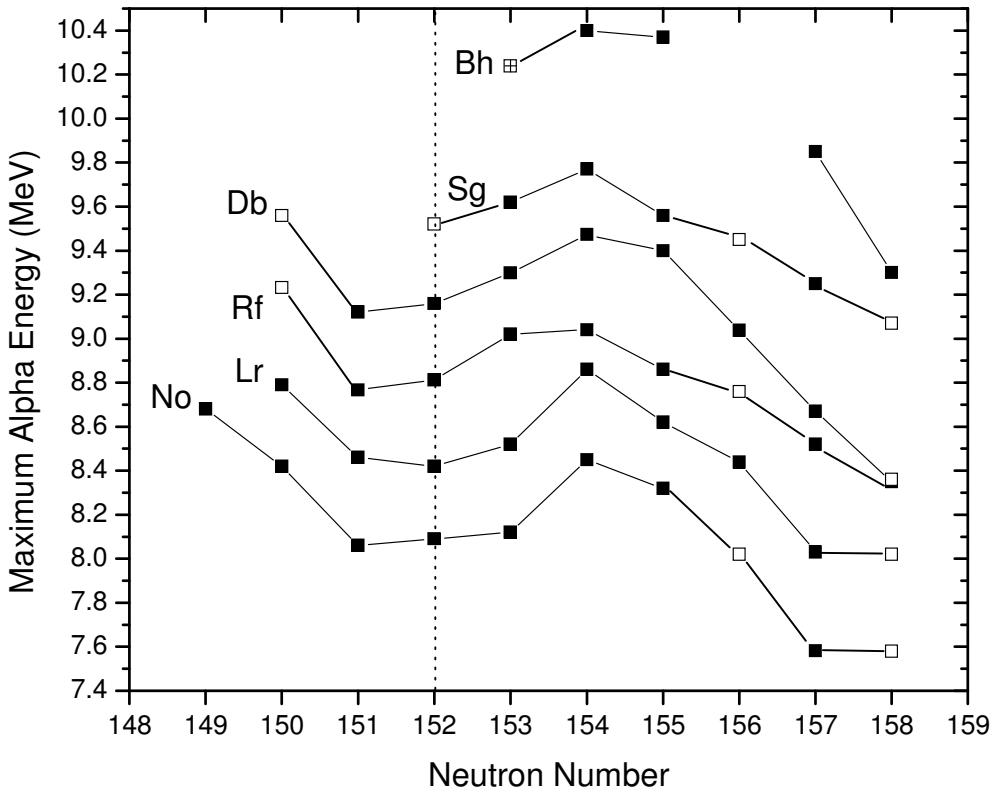

Figure 5.2: Plot of maximum alpha energies as a function of neutron number. Open squares are calculated energies using *Q*-values with masses from [78], filled squares are experimental energies [60, 80], and the gridded square represents this work. The dotted line guides the eye along the $N = 152$ isotones.

work, the effect of the $N = 152$ shell on alpha particle energies had only been observed in systems up to Sg ($Z = 106$).

6. Experimental Results:

Production of ^{266}Mt in the ^{208}Pb(^{59}Co,n) Reaction

6.1 Previous Work

6.1.1 GSI Experiments

Meitnerium was discovered as ^{266}Mt with the use of SHIP in 1984 by Münzenberg *et al*. [9] Encouraged by the results of their 1981 ^{262}Bh discovery [7], they chose to study the ^{209}Bi(^{58}Fe,*n*)^{266}Mt reaction, utilizing three bombarding energies with a total beam dose of $7 \cdot 10^{17}$ ions. One correlated alpha decay chain was observed. The ^{266}Mt decay chain was produced at the highest irradiation energy, and the alpha particle energy was 11.10 MeV. This decay chain passed through two other isotopes of interest in this dissertation, ^{262}Bh and ^{258}Db, and ended in the fission of ^{258}Rf. The observed decay lifetimes of those nuclides correspond well to the currently known values. Alpha particle energies of the daughter products were not available for comparison, as the ^{262}Bh alpha decay escaped their detector, and ^{258}Db underwent EC decay. The cross section corresponding to this one event of ^{266}Mt was 16^{+37}_{-13} pb. They suggest a "most probable" half-life of 3.5 ms from a lifetime of 5 ms.

A later study of the same reaction using the bombarding energy where they observed their first ^{266}Mt event was successful as well [40]. This second experiment resulted in the observation of two more alpha decay chains of ^{266}Mt, confirming their earlier discovery. Both decay chains pass through known nuclides, allowing confident

assignment of Z and A. Unfortunately, neither alpha decay of ^{266}Mt was observed with full energy because one event was an escape, and the other was an escape registering a signal below their detection threshold. They report an additional one-event half-life (from the first escape) of $3.4^{+16.0}_{-1.6}$ ms, and a cross section from the two events of 9^{+11}_{-6} pb. When combined with the one decay chain observed in the first experiment their values change to a ^{266}Mt half-life of $3.4^{+6.1}_{-1.3}$ ms and a cross section of 10^{+10}_{-6} pb.

More recent work on ^{266}Mt led by Hofmann *et al.* in 1997 [39] resulted in a three-point excitation function. Interestingly, they commented that the beam energies reported in their second experiment were not well-known (similar to some results on ^{262}Bh, see Chapter 4) and they did not use previous decays for cross section calculations. In this most recent study, they used three bombarding energies corresponding to 13.4, 15.4, and 16.8 MeV compound nucleus excitation energy. Twelve decay chains correlated to the decay of ^{266}Mt were observed. The alpha particle energies of ^{266}Mt vary between 10.48 - 11.74 MeV, which is not unexpected because of multiple states available in the odd-odd daughter nuclide. Though no γ-spectroscopic work has been done to-date on ^{266}Mt, it is fairly certain that like other odd-odd TAN nuclides, there is a complex level structure. From the two decays in earlier work and twelve decays in this recent work, a half-life of $1.7^{+0.6}_{-0.4}$ ms was reported.

The authors state a maximum cross section of $7.4^{+4.8}_{-3.3}$ pb at a compound nucleus excitation energy of 13.4 MeV. It is interesting to note that this is the lowest energy studied in their work. They also fit these three data points with a Gaussian function, obtaining a peak cross section of 7.5 ± 2.7 pb, very close to the measured maximum. Their fit used the same centroid and width as the function for ^{265}Sg (also measured in

[39]), because the decrease on the high-energy side of the excitation function of ^{266}Mt closely resembled that of ^{265}Sg. On the low-energy side they used the same slope as in the ^{265}Sg excitation function because their neutron binding energies are similar.

6.1.2 Motivation for Additional Studies

Though the ^{209}Bi(^{58}Fe,*n*)^{266}Mt reaction has been well-studied by GSI, no work has been done on the complementary reaction ^{208}Pb(^{59}Co,*n*)^{266}Mt. It is of interest to study this reaction in an attempt to determine if one of the reactions' cross sections is greater in magnitude, similar to our investigations of ^{258}Db and ^{262}Bh. Continuation of this systematic study of paired reactions producing odd-*Z* TANs is crucial to understand any trend in these reactions, not just the individual experimental pairs.

6.2 Experimental Conditions

Three experiments were made to produce ^{266}Mt in the ^{59}Co + ^{208}Pb experiment. The BGS was operated in the same configuration as in all other experiments in this dissertation. The MWPC was in position, and the ^{208}Pb target wheel was installed, though with some different target segments. In earlier experiments some of these individual targets were damaged, and had to be replaced with different ones. The overall areal density of the new ^{208}Pb target wheel was estimated to be ~400 μg/cm^2, only slightly different than the wheel previously in use. The target wheel rotation speed was again approximately 5-10 Hz.

Before the experiments, the four-peak alpha source described in Section 2.2.1.1 was used to collect external calibration data. No internal calibration reactions were run

due to the lack of suitable target and projectile combinations at the time of the experiments. The alpha particle energy resolution determined by the four-point source data over the course of these experiments was $\sigma = \pm 26$ keV. The systematic error in the calibration for alpha particles in the Si-strip detector was ± 5 keV, determined by comparing measured and accepted E_α from implanted activity after correction for the detector's dead layer and the recoil of the daughter product.

The projectile energy expected to be optimal for production of ^{266}Mt was chosen based on calculations from the FBD model [29, 30]. Experimental masses were used when available, and tabulated mass defects from the Thomas-Fermi model [73] were used for those nuclides with unknown masses. Predictions from Świątecki suggested a small cross section (discussed in Section 6.5.2) and only one bombarding energy was used in this work, corresponding to a compound nucleus excitation energy of 14.9 MeV. Table 6.1 contains a summary of the beam energy, integrated beam dose, and resulting cross section for this work as well as the most recent study by GSI. The evaporation residues recoiled out of the target with the momentum of the beam and into the BGS. The BGS magnet settings were chosen to guide only products with a magnetic rigidity of 2.143 T·m to the Si-strip FPD. After the first event of ^{266}Mt was detected in strip 45 (near one edge of the FPD), the magnetic rigidity was decreased to 2.098 T·m in an effort to shift the distribution of products toward the center of the detector. Monte Carlo simulations of EVR trajectories through the BGS [55] as described in Section 2.2.3.3 indicate a total separator efficiency of 0.75 ± 0.02.

During the irradiations, the rate of "EVR-like events" ($15.0 < E_{EVR} < 30.0$ MeV coincident with MWPC signals and anticoincident with punchthrough or upstream

Lab	Reaction	E* (MeV)	Target Thickness (mg/cm^2)	Dose (10^{18} ions)	Number of Events	^{266}Mt Cross Section (pb)
GSI	^{58}Fe + ^{209}Bi [39]	13.4	0.450	1.26	5	$7.4^{+4.8}_{-3.3}$
		15.4	0.450	1.27	4	$6.1^{+4.9}_{-2.9}$
		16.8	0.450	2.24	3	$2.5^{+2.5}_{-1.4}$
LBNL	^{59}Co + ^{208}Pb	14.9	~0.400	0.41	5	$7.7^{+5.2}_{-3.3}$

Table 6.1: Summary of observed results in the study of ^{266}Mt by the ^{209}Bi(^{58}Fe,*n*) and ^{208}Pb(^{59}Co,*n*) reactions.

signals) was 0.26 s^{-1}. The rate of "alpha decay-like events" ($7.0 < E_{alpha} < 12.0$ MeV, in the focal plane only, or reconstructed from a focal plane plus an upstream signal, anticoincident with the MWPC and punchthrough signals) was 0.04 s^{-1}. ^{262,261}Bh decay chains were identified by time- and position-correlated decays in coincidence after an EVR implantation event. A fast beam-shutoff system was implemented to reduce the likelihood of random correlations (See Section 2.2.4 for a discussion of random correlations). Upon the detection of an EVR correlated to an alpha-like event (within 3σ of position and 1 s of the EVR), the beam was automatically switched off for 240 s to enable registration of any subsequent daughter- or granddaughter-like decays under strongly reduced background conditions. The data files were sorted offline, searching for EVR- and alpha-like events with the same energy gates as listed above, and >80 MeV spontaneous fission (SF) –like events ($80 < E_{fission} < 300$ MeV, no MWPC signal). As in the cases of ^{258}Db and ^{262}Bh^{g,m}, once potential decay chains were identified through the offline searches, more specific searches were carried out to lifetimes of 10^4 seconds to try to identify Z = 99-100 decays with long half-lives.

The known decay properties of ^{266}Mt and its associated daughter products are presented in Figure 1.7 in Chapter 1. Conclusive identification of the decay chains did not present the same challenge as in the direct production of ^{258}Db and ^{262}Bh^{g,m}, because the beam energy used in this study was energetically unfavorable to produce the 2*n* product, ^{265}Mt. In the event that the beam energy was increased to one that would be favorable to produce ^{265}Mt, it would still be unlikely that it would have a cross section large enough to be observable in a reasonable amount of experimental time. The chain detection efficiency for conclusive identification of ^{266}Mt was calculated to be 0.922, using the method described in Section 2.2.3.2.

6.3 Observed Decay Chains: ^{208}Pb(^{59}Co,*n*)^{266}Mt

Five decay chains attributed to the decay of ^{266}Mt were observed, and they are depicted in Figure 6.1. Half-life and cross section errors were treated as a special case of the Poisson distribution [63] (see Sections 2.2.3.4 and 2.2.6), and our reported error values are at the 68% confidence interval.

6.3.1 ^{266}Mt

Of the five alpha decays of ^{266}Mt observed in these experiments, only two registered a full-energy signal in the FPD. These decays in chains 1 and 4 registered alpha particle energies of 11.26 and 10.67 MeV, respectively, which match the range of alpha energies observed previously [39]. No EC or SF decays attributable to ^{266}Mt were observed in this work, and we report a half-life of $3.3^{+2.5}_{-1.0}$ ms, agreeing with the previously reported value of $1.7^{+0.6}_{-0.4}$ ms [39].

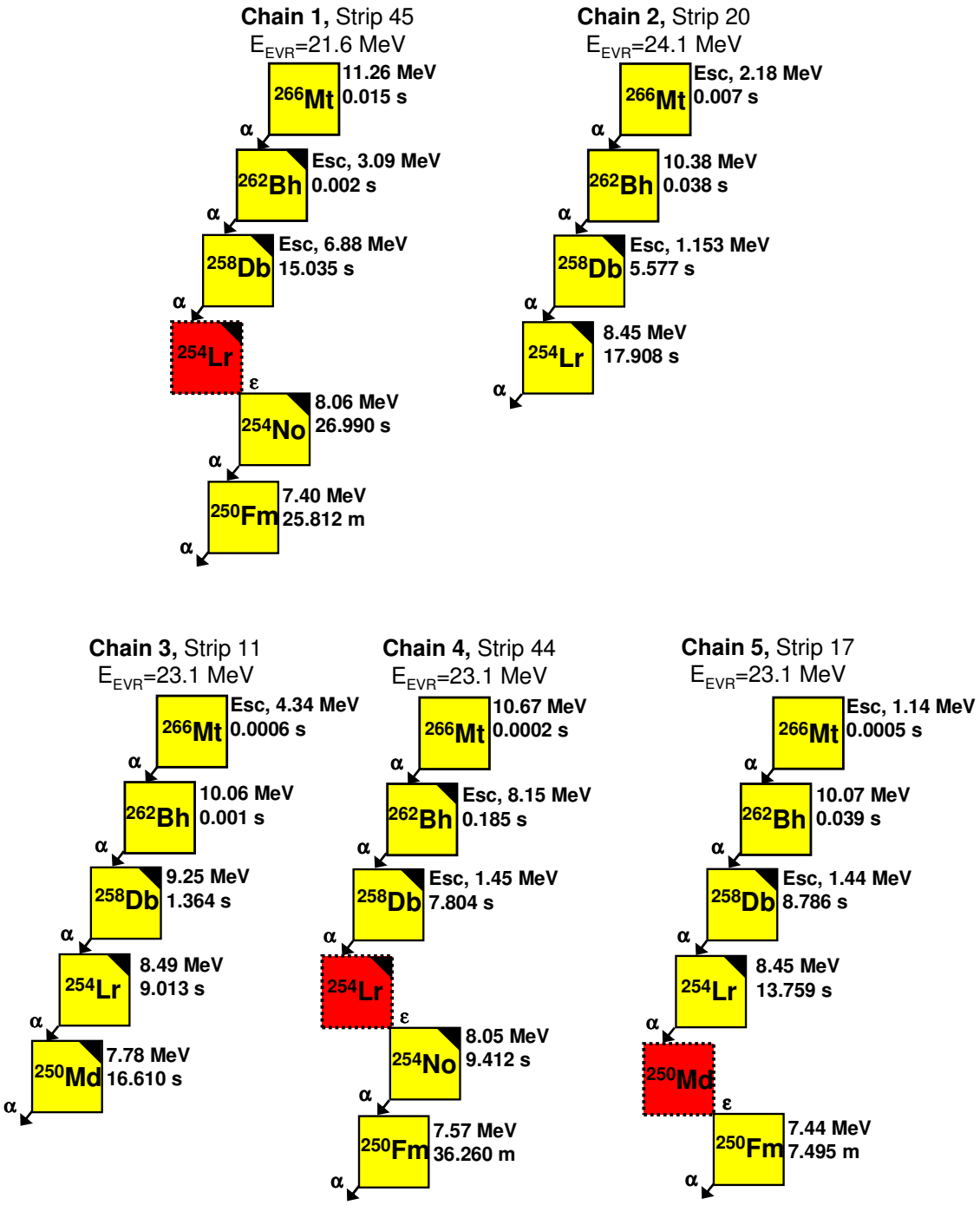

Figure 6.1: Decay chains attributed to the decay of ^{266}Mt. Black triangles in the upper right corner indicate the beam was turned off. Lifetimes following EC decay are the sum of the two decays.

6.3.2 $^{262}Bh^{g,m}$

Five alpha decays of ^{262}Bh were observed as the daughter of ^{266}Mt. Three of these alpha particles were fully stopped in the FPD, registering energies of 10.38, 10.06, and 10.07 MeV in chains 2, 3, and 5, respectively. The alpha particle in chain 4 appears to be a shallow angle escape, depositing 8.15 MeV in the FPD. Isomeric states were assigned as described in Chapter 4, with primary consideration given to the alpha particle energy and secondary consideration given to the observed lifetime. Three decays were assigned to the metastable state (chains 1-3), one to the ground state (chain 4), and no assignment could be conclusively made for one (chain 5). The measured half-lives are $9.4^{+11.0}_{-3.3}$ and 130^{+610}_{-60} ms for the metastable and ground states, respectively. These values compare well with the current literature values of 8.0 ± 2.1 and 102 ± 26 ms [38].

6.3.3 ^{258}Db

Only alpha decay was observed in the five ^{258}Db events detected in these experiments. One full energy alpha particle, three escapes, and one shallow escape were observed. The 9.25 MeV alpha particle in decay chain 3 fits fairly well with the reported alpha line of 9.30. The observation of 100% alpha decay in this nuclide is a somewhat unexpected result in light of the b_{EC} of 0.33 [35], but is likely due to our low counting statistics. A half-life of $5.3^{+4.0}_{-1.6}$ s was measured, comparing well with the $4.4^{+0.9}_{-0.6}$ s half-life from the literature [35].

6.3.4 ^{254}Lr

Two EC decays were inferred and three alpha decays were observed for ^{254}Lr, the alpha decay great-granddaughter of ^{266}Mt. The three alpha particles were all observed with full energy and correspond well to the reported transition at 8.46 MeV [35]. The measured half-life from the three alpha decays is $9.4^{+11.1}_{-3.3}$ s, comparing well with the literature value of 13^{+3}_{-2} s [35].

6.3.5 ^{254}No

^{254}No was made as the EC decay daughter of ^{254}Lr, and two alpha decays were observed in this work. The alpha particle energies observed match well with the literature value [35], and no half-life was measured because its lifetimes are registered as the sum of the ^{254}Lr and ^{254}No lifetimes.

6.3.6 ^{250}Fm

Three alpha decays corresponding to the decay of ^{250}Fm were observed as either the EC decay product of ^{250}Md or the alpha decay product of ^{254}No. The alpha particle energies match well with what has been reported in the literature [47]. The measured half-life of 22^{+39}_{-8} m from the two events not a result of EC decay compares well with the literature value of 30 ± 3 m [47, 48]. Searches for decays beyond ^{250}Fm were not conducted.

6.4 Random Event Analysis

A calculation of the expected number of randomly correlated decays was made for this reaction, using a similar method to the one described in Section 2.2.4. Because the lifetimes of the ^{266}Mt and ^{262}Bh are short compared to the lifetimes of the decays including ^{258}Db and beyond, we chose two times of event decay consideration. This calculation method multiplied the number of EVR-like events by the Poisson probability of observing one alpha within one second and the Poisson probability of observing one alpha within 240 seconds. Alpha-like events were required to have energies between 7.0 – 12.0 MeV to cover the range of energies spanned by all products. EVR-like events were required to have energies between 15.0 – 30.0 MeV. The duration of the experiment was 720,887 seconds. The number of random chains expected over the duration of the experiment from one short alpha-like event and one longer-lifetime alpha-like event was 0.095, and on the order of 10^{-5} and lower for EVRs followed by greater than two alpha-like events. The five alpha decay chains observed in this work are true events and not random correlations.

6.5 Discussion

6.5.1 Summary of Results on ^{266}Mt

A cross section of $7.7^{+5.2}_{-3.3}$ pb was measured at an excitation energy of 14.9 MeV in the ^{59}Co + ^{208}Pb reaction. Figure 6.2 represents the data available on ^{266}Mt, from the ^{58}Fe + ^{209}Bi excitation function reported by Hofmann *et al*. and the complementary ^{59}Co + ^{208}Pb reaction. The energy loss through the targets had to be estimated for the GSI data, as those data were not reported in the literature. We do not fit the GSI data with the same

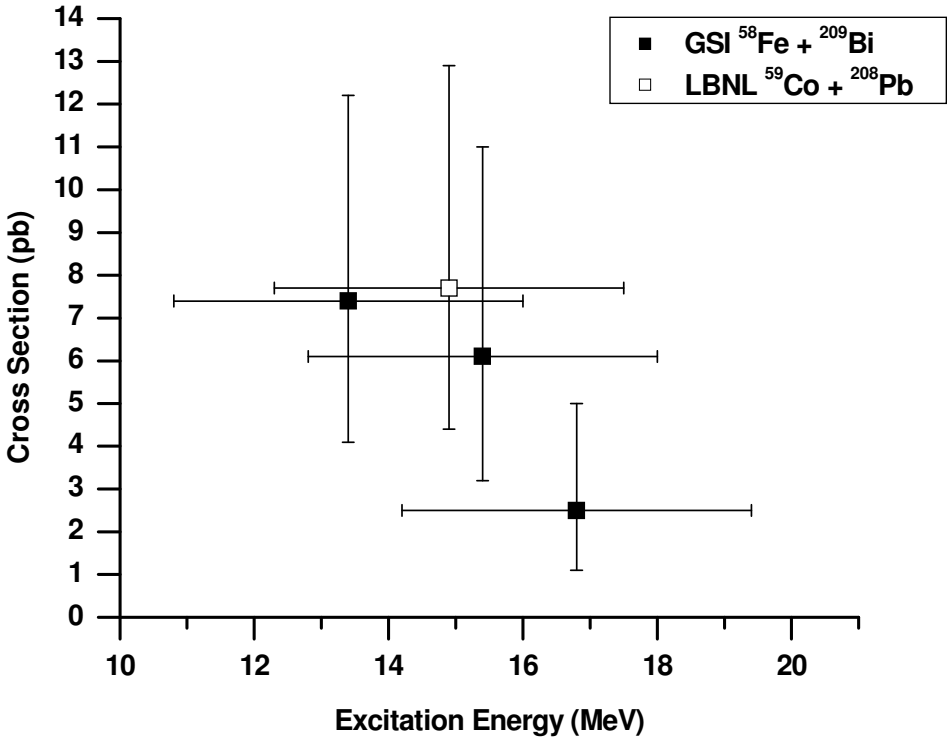

Figure 6.2: Experimental results on ^{266}Mt. Filled squares represent GSI data from the ^{209}Bi(^{58}Fe,*n*) reaction [39]; the open square represents LBNL results with the ^{208}Pb(^{59}Co,*n*) reaction. Horizontal error bars represent the energy width of the target.

Gaussian function joined to an exponential function as done in previous chapters. Three data points are too few to obtain a meaningful fit via this method, and we instead rely on the authors' reported fit value of 7.5 ± 2.7 pb. The two cross section values are identical within statistical error bars, and we cannot say if there is a preferred reaction entrance channel at this time.

Overall, the decay properties of ^{266}Mt and its daughters fit well with the previously reported values by GSI.

6.5.2 Comparisons to Model Predictions

As is the case with all the reactions in this dissertation, W.J. Świątecki provided us with 1*n* cross section predictions from the FBD model [29, 30]. For the ^{58}Fe + ^{209}Bi reaction, the prediction of 12.8 pb at a compound nucleus excitation energy of ~13.5 MeV is relatively close to the 1*n* peak value of 7.5 ± 2.7 pb at approximately 13.4 MeV from GSI's fit of their data. The correlation in excitation energies at the peak is excellent. The predicted location of the barrier for this reaction is 16.9 MeV, or approximately 3.5 MeV higher in energy than the peak of their excitation function.

For the ^{59}Co + ^{208}Pb reaction, Świątecki predicts 7.1 pb at ~14.1 MeV compound nucleus excitation energy. Both values compare very well to the one data point obtained in this reaction, at $7.7^{+5.2}_{-3.3}$ pb and 14.9 MeV excitation energy. The estimated location of the barrier for this reaction is at 19.6 MeV, higher in energy than the data point by approximately 4.7 MeV.

7. Related Studies: ^{272}Rg

7.1 Previous Work

7.1.1 GSI Experiments

The element roentgenium (Z = 111) was discovered as ^{272}Rg as the product of the ^{209}Bi(^{64}Ni,n) reaction at GSI in 1994 [11]. Three projectile energies were studied and three decay chains unambiguously correlated to the known isotopes ^{260}Db and ^{256}Lr were observed. Decay also proceeded through new isotopes of ^{268}Mt and ^{264}Bh, and the decay scheme of ^{272}Rg is depicted in Figure 7.1. This first report of ^{272}Rg indicated it decayed exclusively by alpha particle emission at an energy of 10.82 MeV with a half-life of $1.5^{+2.0}_{-0.5}$ ms. The maximum cross section of $3.5^{+4.6}_{-2.3}$ pb was measured at a compound nucleus excitation energy of 12.5 MeV.

This reaction was repeated at GSI in 2000 and the group observed three more decay chains of ^{272}Rg [42]. Thirteen days of beam time were devoted to the study of one bombarding energy in an effort to improve the statistical error bars. A dose of $2.2 \cdot 10^{18}$ ions was collected in this time. The energy chosen was 320 MeV, corresponding to 12.5 MeV excitation energy, as used in the first experiment. The observed decay properties fit well with those discovered in their earlier work, and an additional alpha decay line for ^{272}Rg at 11.03 MeV was observed. They report a mean cross section value for the two decay chains observed in the first experiment and the three in this experiment as $2.9^{+1.9}_{-1.3}$ pb.

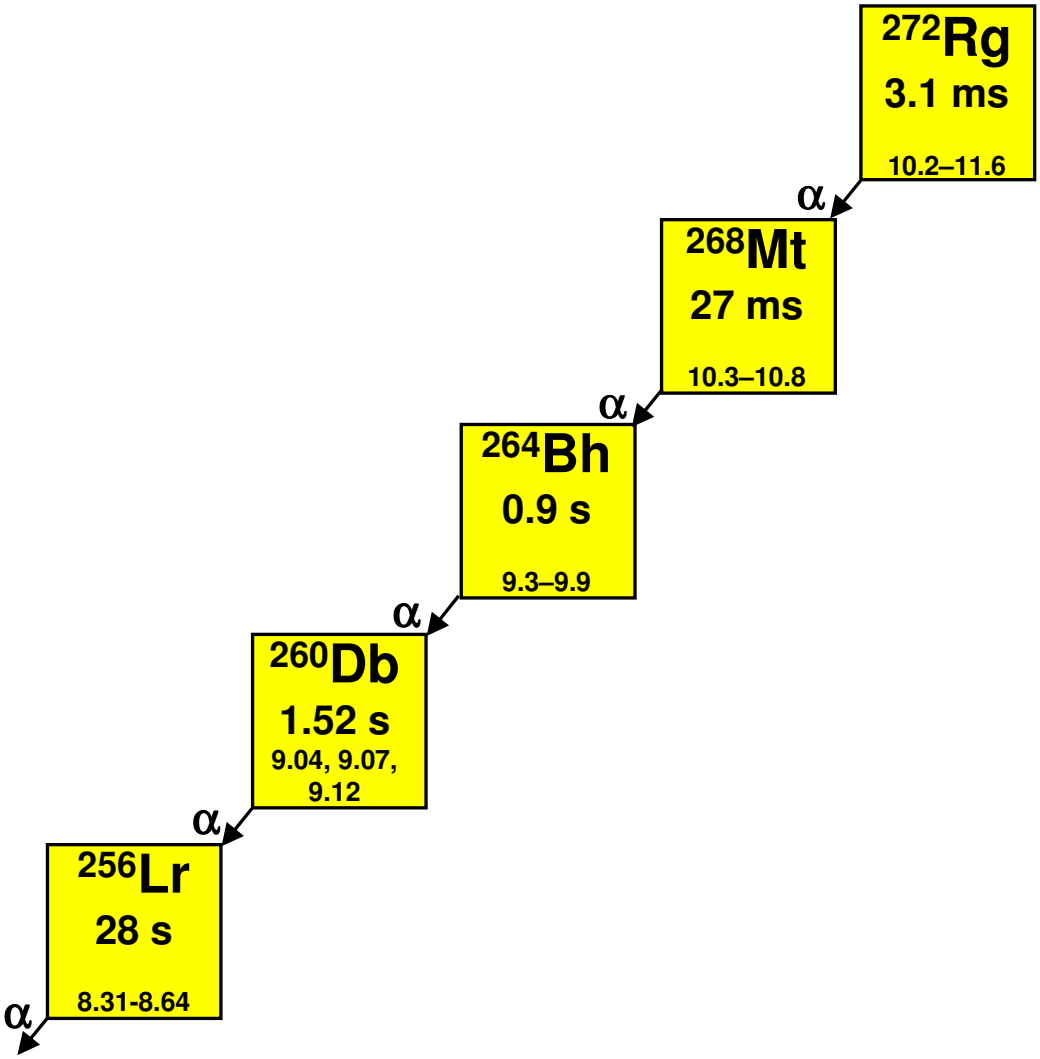

Figure 7.1: Decay scheme of ^{272}Rg. All energies listed in MeV. Half-lives for ^{272}Rg, ^{268}Mt, and ^{264}Bh are weighted means of data from [42] and [43]. Data from [81] and [82] used for ^{260}Db and ^{256}Lr, respectively.

In addition to improving upon their first work on this isotope, this second study would satisfy the IUPAC Transfermium Working Group's requirement that claims on new elements must be reproduced before they are officially recognized. Their success in this second experiment allowed the group to be awarded discovery credit of element 111, and the name roentgenium was chosen in honor of W. C. Röntgen, discoverer of x-rays.

7.1.2 RIKEN Experiments

Outside confirmation of the GSI work on the ^{209}Bi(^{64}Ni,*n*)^{272}Rg reaction was accomplished in the first half of 2003 by the heavy element research group led by K. Morita at the RIKEN laboratory in Japan [43]. Their gas-filled GARIS separator [83], similar in principle to the BGS, was used in that work and the team observed the decay of fourteen alpha decay chains originating from ^{272}Rg. Three bombarding energies correlating to compound nucleus excitation energies of 15.4, 17.5 and 19.8 MeV were studied, and intentionally span higher energies than GSI. Cross sections of $2.6^{+2.3}_{-1.5}$ and $2.5^{+1.2}_{-0.9}$ pb were measured for the first two energies, respectively, and an upper limit of 1.1 pb was measured for the third energy.

The observed alpha particle energies agree somewhat with the previous work from GSI. They observed additional alpha particle decays with energies of 11.37 and 10.40 MeV, which was not unexpected due to their longer irradiation time and observation of many more decay chains than GSI. It is also important to keep in mind ^{272}Rg and its decay products are all odd-odd nuclides (as is the case with most nuclides in this dissertation) and will have complex alpha decay structure. The measured half-life of $3.8^{+1.4}_{-0.8}$ ms does not compare well with the $1.6^{+1.1}_{-0.5}$ ms half-life measured (as the mean of six decay chains) by the GSI group. Isomeric states in ^{272}Rg and its daughters ^{268}Mt and ^{264}Bh have been suggested but more compelling data would be needed to certify such states.

7.1.3 LBNL Experiments

Folden *et al*. performed the complementary reaction ^{208}Pb(^{65}Cu,*n*)^{272}Rg in 2003 using the BGS at LBNL [41]. This reaction utilized an odd-*Z* projectile on an even-*Z* target instead of an even-*Z* projectile on an odd-*Z* target, and was the first confirmation of element 111 via a reaction other than ^{64}Ni + ^{209}Bi. A single bombarding energy was run in this experiment, corresponding to a compound nucleus excitation energy of 13.2 MeV. One decay chain correlated to the decay of ^{272}Rg was observed, and the decay properties of the chain members agree well with the previous studies. The cross section attributed to the one event is $1.7^{+3.9}_{-1.4}$ pb.

7.2 Summary

A table detailing the four experiments studied at the three laboratories is presented in Table 7.1, and graphically depicted in Figure 7.2. These data illustrate that the cross section in the production of ^{272}Rg by either the ^{64}Ni + ^{209}Bi or ^{65}Cu + ^{208}Pb reaction is small, less than 10 pb. The error bars on both the statistical uncertainty and the energy width of the target overlap to a large extent. Additional studies would be required to improve the statistical uncertainty so that we may obtain a clearer understanding of the cross sections, and any preference of entrance channel.

7.2.1 Excitation Function for the ^{209}Bi(^{64}Ni,*n*)^{272}Rg Reaction

An excitation function from GSI and RIKEN data is presented in Figure 7.3, with a maximum likelihood fit by the method described in Section 2.2.5. The data presented a challenge to fit, and the parameter values of $\omega = 1.348$ and $\lambda = 0.183$ were used [69].

Lab	Reaction	E* (MeV)	Target Thickness (mg/cm^2)	Dose (10^{17} ions)	Number of Events	^{272}Rg Cross Section (pb)
GSI	^{64}Ni + ^{209}Bi [11, 42]	9.4	0.450	10	0	<2.9
		11.0	0.450	11	1	$1.7^{+3.3}_{-1.4}$
		12.5	0.450	11	2	$3.5^{+4.6}_{-2.3}$
		12.5	0.450	22	3	$2.5^{+2.5}_{-1.4}$
RIKEN	^{64}Ni + ^{209}Bi [43]	15.4	0.252	20.2	3	$2.6^{+2.3}_{-1.5}$
		17.5	0.285	49.4	8	$2.5^{+1.2}_{-0.9}$
		19.8	0.298	25.0	0	<1.1
LBNL (Folden)	^{65}Cu + ^{208}Pb [41]	13.2	0.470	6.6	1	$1.7^{+3.9}_{-1.4}$

Table 7.1: Summary of observed results in the study of ^{272}Rg by the ^{209}Bi(^{64}Ni,*n*) and ^{208}Pb(^{65}Cu,*n*) reactions.

Allowing these parameters to vary freely resulted in a fit that was not physically meaningful in light of the experimental data points. Assuming the energies reported at each facility may be compared to each other, we see that a cross section of 5.0 ± 1.2 pb is expected at the peak of this function at a compound nucleus excitation energy of 13.2 ± 0.7 MeV. Here using the fit is quite advantageous, because no clear peak point has been measured to-date.

7.2.2 Comparisons to Model Predictions

As in other sets of reaction pairs, Świątecki provided us with predictions of the maximum 1*n* cross section and its corresponding energy from the FBD model. The prediction for the ^{65}Cu + ^{208}Pb reaction is 1.5 pb at an excitation energy of approximately 14.1 MeV. The location of the barrier from the FBD model is at an excitation energy of

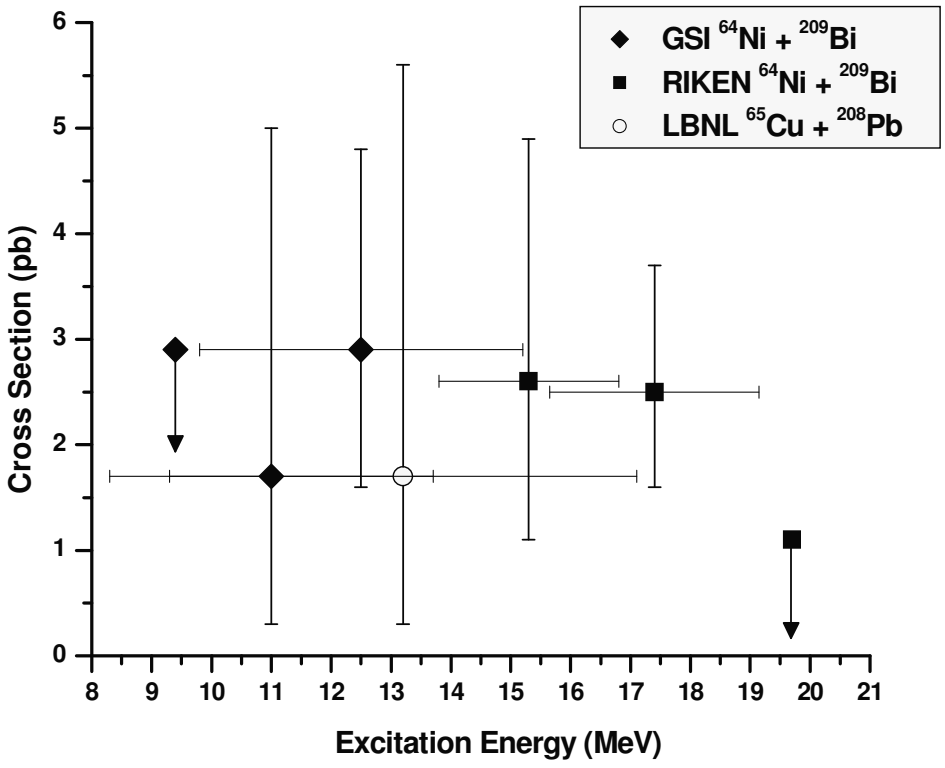

Figure 7.2: Data from GSI, RIKEN, and LBNL studies of the production of ^{272}Rg in the ^{209}Bi(^{64}Ni,*n*) and ^{208}Pb(^{65}Cu,*n*) reactions [11, 41-43].

15.6 MeV. The single data point measured by Folden *et al*. was at a cross section of 1.7 pb and 13.2 MeV excitation energy. It is not possible to determine whether this experimental data point is at or near the peak of the excitation function for this reaction without further study.

The prediction for the cross section of the ^{64}Ni + ^{209}Bi reaction is 1.8 pb and an excitation energy of approximately 14.2 MeV. This model predicts the location of the barrier for this reaction to be at 13.4 MeV. The cross section value obtained from the fit of the data suggests a larger cross section than the FBD model by approximately a factor

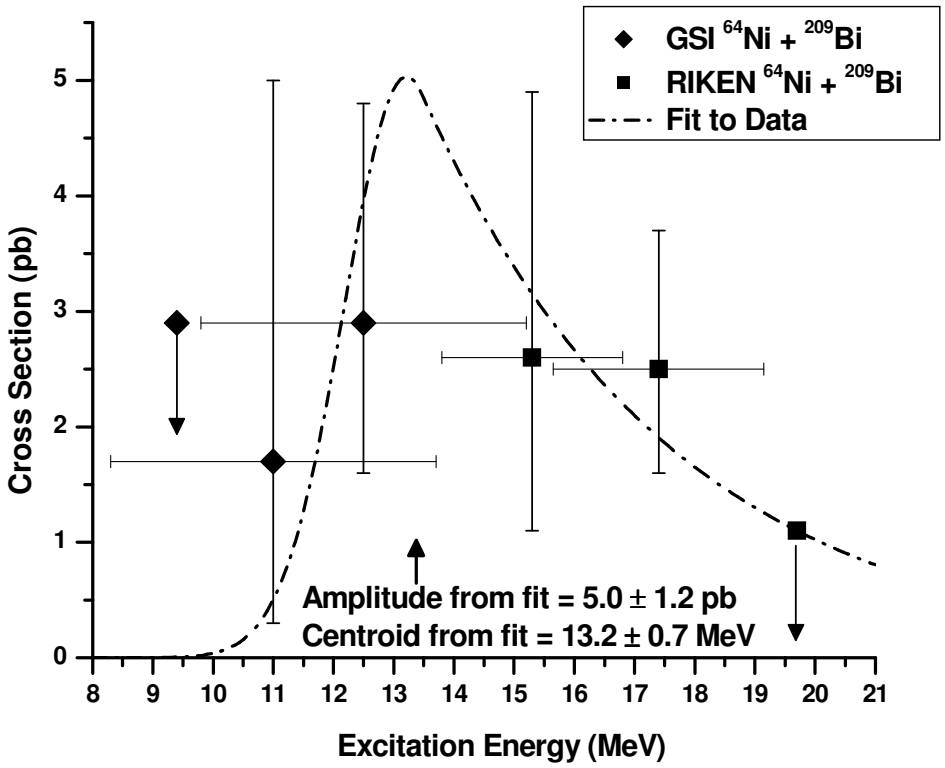

Figure 7.3: Excitation function for the ^{209}Bi(^{64}Ni,*n*)^{272}Rg reactions comprised of results from GSI [11, 42]and RIKEN [43]. Filled diamonds represent the GSI data, filled squares represent the RIKEN data. Dotted-dashed line is the line of best fit from the maximum likelihood method described in Section 2.2.5. Arrow near abscissa represents the location of the barrier from the FBD model [29, 30, 32]. See main text for additional discussion.

of three. However, it is not known if a comparison of the beam energies used to obtain these data at GSI and RIKEN may be made. If these energies are not directly comparable, the fit loses its meaning. The peak of the fit and the predicted peak from the model are fairly close, within 1 MeV. The peak of the fit is also very close to the predicted location of the barrier by the FBD model. By comparing the two sets of data, it does not appear that there is any difference in cross section within error bars.

8. Discussion, Conclusions, and Future Research

In this work, numerous compound nucleus reactions producing odd-*Z* transactinides were studied. This chapter presents a summary of these results, beginning with a discussion of the series of paired reactions producing the same compound nucleus by changing only the location of one proton between the reactions' target and projectile (e.g.: ^{50}Ti + ^{209}Bi vs. ^{51}V + ^{208}Pb).

8.1 Discussion of Systematic Study Results

The results of the eight reactions in the study of reaction pairs producing the same compound nucleus are listed in Table 8.1. This table also contains the values of the effective fissility for each reaction, computed using the formulae from Section 1.3. When these 1*n* cross sections are graphed as a function of the *Z* of the produced compound nucleus, we see a distinct trend as observed in Figure 8.1. Squares represent the ^{208}Pb-based reactions and triangles represent the ^{209}Bi-based reactions. Filled points represent a maximum cross section obtained via a fit to an excitation function. The filled point for ^{266}Mt from the ^{58}Fe + ^{209}Bi reaction is the value of the fit reported by GSI [39]. The filled point for ^{272}Rg from the ^{64}Ni + ^{209}Bi reaction is from the maximum likelihood fit method described in Section 2.2.5. Open points represent the maximum observed cross section for a reaction where no fit was feasible or where only one data point was measured. Error bars represent the uncertainty in the fit or the uncertainty on the individual data

Nuclide	Reaction	Work Completed By	Peak 1*n* Cross Section (pb)	Effective Fissility (*x*)
^{258}Db	^{50}Ti + ^{209}Bi	LBNL [72]	5830 ± 770	0.824
	^{51}V + ^{208}Pb	***This work***	1300 ± 240	0.826
^{262}Bh	^{54}Cr + ^{209}Bi	***This work***	430 ± 110	0.847
	^{55}Mn + ^{208}Pb	LBNL [37], ***this work***	530 ± 100	0.849
^{266}Mt	^{58}Fe + ^{209}Bi	GSI [39]	7.5 ± 2.7	0.870
	^{59}Co + ^{208}Pb	***This work***	$7.7^{+5.2}_{-3.3}$	0.872
^{272}Rg	^{64}Ni + ^{209}Bi	GSI [42], RIKEN [43]	5.0 ± 1.2	0.892
	^{65}Cu + ^{208}Pb	LBNL [41]	$1.7^{+3.9}_{-1.4}$	0.894

Table 8.1: Summary of all reactions contributing to the systematic study of paired odd-*Z* TAN compound nucleus reactions, with calculated effective fissility values.

point, whichever is applicable. In some cases the error bars are smaller than the symbol. The data points are offset slightly in *Z* for clarity.

This exponential decrease in cross section with increase in *Z* has been known for quite some time. The new information gained from this figure is the striking overlap of the data points representing each pair of reactions. This suggests that there is no preferred entrance channel when the paired reactions producing the same compound nucleus differ by only one proton between the target and projectile. Though some of the cross sections could be improved with better counting statistics, a large difference in cross section would be apparent at this time. At most there is a small entrance channel effect.

The lack of a preferred entrance channel indicates that in most cases there is no clear advantage in choosing the ^{209}Bi-based reaction for reasons of decreased effective fissility. In examining the effective fissility values calculated for these reactions in

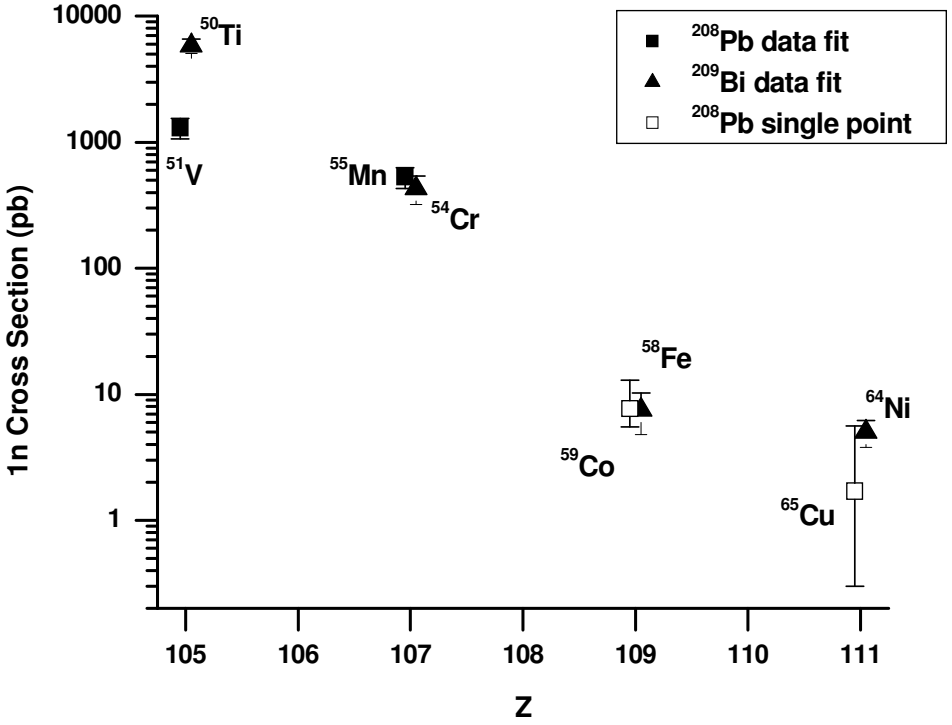

Figure 8.1: 1*n* cross section as a function of the *Z* of the compound nucleus. Squares represent ^{208}Pb-based reactions and triangles represent ^{209}Bi-based reactions. Filled points represent a maximum cross section obtained via a fit method and open points represent the maximum observed cross section. Error bars on filled points arise from the uncertainty in the fit. Error bars on open points are the uncertainty of the individual data point. In some cases the error bars are smaller than the symbol. Points are offset slightly in *Z* for clarity. (see text for more discussion)

Table 8.1, there is an insignificant difference in effective fissility, between the members of a single reaction pair, with $\Delta x = 0.002$. Additionally, the Δx between the isotopes studied (e.g.: ^{258}Db and ^{262}Bh) is approximately 0.02, still a small value. The only pair of reactions in this study that exhibits a large difference in 1*n* cross section is the pair producing ^{258}Db: ^{50}Ti + ^{209}Bi, and ^{51}V + ^{208}Pb. The 5.83 nb cross section of the ^{50}Ti +

^{209}Bi reaction is a factor of ~4.5 greater than that of the ^{51}V + ^{208}Pb reaction. This is an interesting result suggesting further study.

It has been suggested in the literature that cross sections of transactinide (TAN) elements decrease "by a factor of 3.7 per element *Z* at a fixed isospin of the reacting system [39]." By examining the cross sections of the reactions producing the same-isospin products ^{258}Db, ^{262}Bh, and ^{266}Mt, we find this assertion to not hold entirely true. There seems to not be a constant factor such as 3.7 which can easily and accurately estimate the peak magnitude of a cross section.

Capture cross sections for all eight reactions were calculated using the method described in [29] with updated parameters [32]. The center-of-target, center-of-mass energy at the peak of the excitation function was used in the calculations. When no excitation function was measured, the best data available were used. These values are presented in Table 8.2, along with the peak 1*n* reaction cross sections for comparison. Ratios of the capture cross sections and 1*n* reaction cross sections are included. We observe that the capture cross sections for the reactions generally increase as the *Z* of the CN increases. This result is as expected, because as the reaction products increase in *Z* the peak of the excitation function becomes less sub-barrier. It is interesting to note that the ratio of the capture cross sections stay within a factor of five (from 1.6 – 3.9) while the cross sections themselves span three orders of magnitude (from 1.7 – 5830 pb).

In discussions with W. J. Świątecki, it has been suggested that the cross sections in these paired reactions are similar due to the effect of charge equilibration on the fusing dinuclear system. Hartmann and Gross [84] have shown that in asymmetric nuclear reactions, there is a charge transfer from the lighter to the heavier nucleus immediately

Reaction	$\sigma_{capture}$ (mb)	Ratio of $\sigma_{capture}$ (^{209}Bi/^{208}Pb)	Peak 1*n* Cross Section (pb)	Ratio of Peak 1*n* Cross Sections (^{209}Bi/^{208}Pb)
^{209}Bi(^{50}Ti,*n*)^{258}Db	14.1	3.5	5830 ± 770	4.5 ± 0.2
^{208}Pb(^{51}V,*n*)^{258}Db	4.0		1300 ± 240	
^{209}Bi(^{54}Cr,*n*)^{262}Bh	21.6	3.9	430 ± 110	0.8 ± 0.3
^{208}Pb(^{55}Mn,*n*)^{262}Bh	5.5		530 ± 100	
^{209}Bi(^{58}Fe,*n*)^{266}Mt	17.0	1.7	7.5 ± 2.7	1.0 ± 0.7
^{208}Pb(^{59}Co,*n*)^{266}Mt	10.1		$7.7^{+5.2}_{-3.3}$	
^{209}Bi(^{64}Ni,*n*)^{272}Rg	37.7	1.6	5.0 ± 1.2	2.9 ± 1.6
^{208}Pb(^{65}Cu,*n*)^{272}Rg	23.9		$1.7^{+3.9}_{-1.4}$	

Table 8.2: Capture cross sections for all experiments used in the systematic study of paired reactions, calculated by the method described in [29] with updated parameters [32]. Peak 1*n* cross sections and ratios for these values are included for comparison.

prior to fusion. The resulting reduction in barrier potential leads to an increased cross section. This process would allow the ^{51}V + ^{208}Pb reaction to proceed as ^{51}Ti + ^{208}Bi reaction, for example. Though this effect is not seen in this individual reaction pair, it is likely the cause for the great similarity of the other paired reactions' cross sections.

The possible influence of the barrier on the peak 1*n* cross sections was examined as well. By subtracting the energy of the calculated location of the barrier by the FBD model from the energy at the maximum of the excitation function (either from a fit or the best data available) we can see how sub-barrier the reaction is. The data for the eight reactions in this systematic study were treated in this way, and the result is depicted in Figure 8.2. The filled diamonds represent ^{209}Bi-based reactions, and the open diamonds represent ^{208}Pb-based reactions. The error bars represent the uncertainty in the centroid of the fit used to obtain the cross section, or in the cases of the ^{208}Pb-based ^{266}Mt and

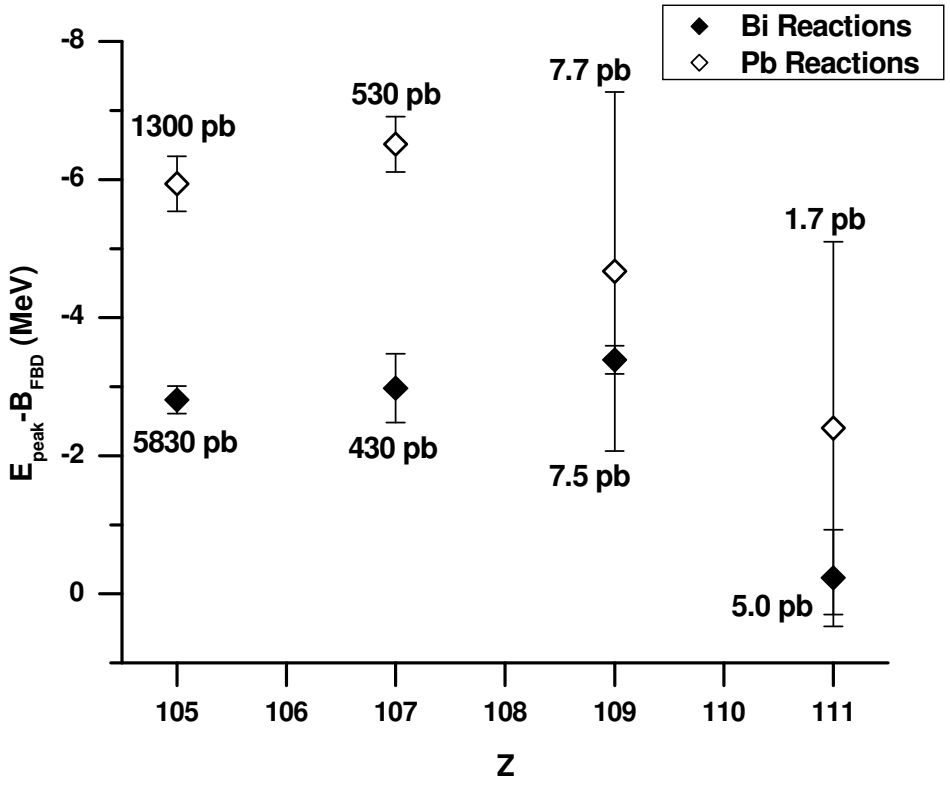

Figure 8.2: The difference in barrier energy between the "Fusion By Diffusion" model [29, 30, 32] and the location of the peak of the eight reactions' 1*n* excitation functions as a function of the *Z* of the compound nucleus. Error bars represent uncertainty in the fit's centroid, or when a fit was not possible (^{208}Pb-based ^{266}Mt and ^{272}Rg points) the uncertainty in the projectile energy was used. Corresponding cross section values for each data point are presented for comparison.

^{272}Rg reactions, the uncertainty in the projectile energy. There is a clear trend in which the Pb-based reactions are approximately 1.5-3.0 MeV more sub-barrier than the Bi-based reactions. However, the cross sections do not appear to be affected by this, because there is no observed trend in their magnitudes with respect to how sub-barrier the reaction is. This effect is also likely due to charge equilibration in these asymmetric reactions.

8.2 Conclusions

Several compound nucleus reactions producing odd-*Z* transactinides were studied to measure their cross sections, using the 88-Inch Cyclotron and the Berkeley Gas-Filled Separator at the Lawrence Berkeley National Laboratory. The main objective of these studies was to examine any role the entrance channel, or unique target and projectile combination, would have on the cross sections when the same compound nucleus was produced via different reaction pathways differing by only one proton between the target and projectile. It is proposed that the effect of charge equilibration between the projectile and target nucleus led to the cross sections for each reaction within a pair being identical within statistical uncertainty, except in the case of the reactions producing ^{258}Db.

The absence of a difference in cross section in the reactions producing ^{262}Bh, ^{266}Mt, and ^{272}Rg suggests that more affordable, monoisotopic beams such as ^{55}Mn or ^{59}Co could be used instead of costly separated isotopes like ^{54}Cr and ^{58}Fe. With no added gain in cross section these expensive and at times difficult to obtain beam materials are not necessary.

The new TAN isotope ^{260}Bh was also produced in the ^{209}Bi(^{52}Cr,*n*) reaction. It was conclusively identified by the observation of eight correlated alpha decay chains. The synthesis and identification of new TAN isotopes and measurements of their decay properties are essential to an understanding of nuclear stability, as well as improving the prospects of producing higher-*Z* elements and more isotopes in this region of the chart of nuclides. By investigating these isotopes, we will also gain a better understanding of nuclear masses and be able to determine the location and strength of both spherical and deformed shells in this region. ^{260}Bh was observed to have a major alpha decay line at

10.16 MeV, decaying 100% by alpha particle emission with a half-life of 35^{+19}_{-9} ms. The measured cross section from these eight decay chains of ^{260}Bh is 59^{+29}_{-20} pb, at a compound nucleus excitation energy of 15.0 MeV.

In both the systematic study of paired reactions and the production of ^{260}Bh we have compared our experimental results to model predictions by W. J. Świątecki from the "Fusion By Diffusion" model. In all cases, the magnitude of the peak 1*n* cross section was within a factor of two of the predicted values, indicating that this model is indeed a reliable tool for predicting these maxima. In most cases, the energy at the peak of the excitation function was within 1 MeV of the predicted values, also.

8.3 Future Work

Many of the excitation functions studied could benefit from more work. It would be of interest to obtain full 2*n* excitation functions for the reactions producing ^{258}Db and ^{262}Bh. By doing so the shape of the excitation function could be determined, and the magnitude of the 1*n* vs. 2*n* excitation functions could be compared to gain information about the barrier.

In order to determine if the cross section measured in the ^{59}Co + ^{208}Pb reaction is truly at or very near the peak of the 1*n* excitation function, a full excitation function would need to be measured. An additional 3-4 bombarding energies should be adequate to acquire the data needed for a more complete picture. Additionally, studying the ^{58}Fe + ^{209}Bi reaction at low bombarding energies could help better determine the shape of the low-energy side of the excitation function measured by GSI.

It is also of interest to study the ^{208}Pb(^{59}Co,n)^{266}Mt, ^{209}Bi(^{64}Ni,n)^{272}Rg, and ^{208}Pb(^{65}Cu,n)^{272}Rg reactions in more detail, with additional bombarding energies and higher counting statistics so the systematic study of paired reactions may be enhanced. It is possible that with more information a difference in cross sections may be uncovered which is not observable with the current data. If it can be established that the energies at GSI and RIKEN are directly comparable, this will further benefit these studies.

By studying additional bombarding energies and completing the excitation function for ^{260}Bh we can compare these results to what is predicted by the FBD model. In addition to the intrinsic scientific interest of producing a new TAN isotope and determining its decay properties, increasing the beam energy sufficiently to produce ^{259}Bh is of interest so we may investigate what effect the $N = 152$ shell has on alpha decay. With the discovery of ^{260}Bh we have already observed that this shell affects alpha decay energies in nuclides with Z up to 107, and continuing that effort would be of interest in determining the strength of this deformed neutron shell.

Spectroscopic study of K-isomers in this region of the chart of nuclides is an emerging area of research in the field of heavy element physics [35, 36]. More information about the isomeric states via α–γ or α-e^--γ coincidences is vital in determining these nuclides' level structures and providing insight into complicated decay schemes, including the actual number of isomers present. It may be of interest to conduct experiments to produce ^{258}Db and ^{262}Bh below the 2n exit channel threshold to eliminate the confusion between the 1n and 2n products.

The use of more sensitive detection equipment such as double-sided Si-strip detectors and Ge clover detectors would enable observation of both conversion electrons

and gamma signals, capabilities not in place at the time of these experiments. In light of the observation of SF from ^{262}Bh, it would also be interesting to try to carry out the same experiment for a longer time to try and observe additional decays of this nature, potentially benefited by the same advances in detection equipment. The challenge in achieving better data in this study is the relatively low 1*n* reaction cross section. Future work to increase beam intensities and efficiencies could make studies of these higher-*Z* TANs a reality.

The superconducting ion source VENUS (Versatile ECR Ion Source for Nuclear Science) [85] at LBNL has been used for one heavy element research experiment as of the writing of this dissertation. Its large beam intensities (compared to the AECR-U ion source in use currently) are ideal for heavy-element studies, and it could be used to expand the experimental capability of this research program at the 88-Inch Cyclotron.

9. References

[1] A. Ghiorso, B.G. Harvey, G.R. Choppin, S.G. Thompson, G.T. Seaborg, Phys. Rev. **98,** 1518 (1955).

[2] V. Ninov, K.E. Gregorich, C.A. McGrath, AIP Conference Proceedings ENAM 98, **455,** 704 (1998).

[3] G. Münzenberg, W. Faust, S. Hofmann, P. Armbruster, K. Guettner, H. Ewald, Nuclear Instruments & Methods **161**, 65 (1979).

[4] A. Ghiorso, M. Nurmia, J.A. Harris, K.A. Eskola, P.L. Eskola, Physical Review Letters **22**, 1317 (1969).

[5] G.N. Flerov, Y.T. Oganesyan, Y.V. Lobanov, Y.A. Lazarev, S.P. Tret'yakova, I.V. Kolesov, V.M. Plotko, Nuclear Physics A **160,** 181 (1971).

[6] A. Ghiorso, J.M. Nitschke, J.R. Alonso, C.T. Alonso, M. Nurmia, G.T. Seaborg, E.K. Hulet, R.W. Lougheed, Physical Review Letters **33,** 1490 (1974)

[7] G. Münzenberg, S. Hofmann, F.P. Heßberger, W. Reisdorf, K.H. Schmidt, J.H.R. Schneider, P. Armbruster, C.C. Sahm, B. Thuma, Zeitschrift Für Physik A: Atoms and Nuclei **300**, 107 (1981).

[8] G. Münzenberg, P. Armbruster, H. Folger, F.P. Heßberger, S. Hofmann, J. Keller, K. Poppensieker, W. Reisdorf, K.H. Schmidt, H.J. Schött, Zeitschrift Für Physik A: Atoms and Nuclei **317**, 235 (1984).

[9] G. Münzenberg, W. Reisdorf, S. Hofmann, Y.K. Agarwal, F.P. Heßberger, K. Poppensieker, J.R.H. Schneider, W.F.W. Schneider, K.H. Schmidt, H.J. Schött, P. Armbruster, C.C. Sahm, D. Vermeulen, Zeitschrift Für Physik A: Atoms and Nuclei **315**, 145 (1984).

[10] S. Hofmann, V. Ninov, F.P. Heßberger, P. Armbruster, H. Folger, G. Münzenberg, H.J. Schött, A.G. Popeko, A.V. Yeremin, A.N. Andreyev, S. Saro, R. Janik, M. Leino, Zeitschrift Für Physik A: Hadrons and Nuclei **350**, 277 (1995).

[11] S. Hofmann, V. Ninov, F.P. Heßberger, P. Armbruster, H. Folger, G. Münzenberg, H.J. Schött, A.G. Popeko, A.V. Yeremin, A.N. Andreyev, S. Saro, R. Janik, M. Leino, Zeitschrift Für Physik A: Hadrons and Nuclei **350**, 281 (1995).

[12] S. Hofmann, V. Ninov, F.P. Heßberger, P. Armbruster, H. Folger, G. Münzenberg, H.J. Schött, A.G. Popeko, A.V. Yeremin, S. Saro, R. Janik, M. Leino, Zeitschrift Für Physik A: Hadrons and Nuclei **354**, 229 (1996).

[13] K. Morita, K. Morimoto, D. Kaji, T. Akiyama, S.-I. Goto, H. Haba, E. Ideguchi, R. Kanungo, K. Katori, H. Koura, H. Kudo, T. Ohnishi, A. Ozawa, T. Suda, K. Sueki, H. Xu, T. Yamaguchi, A. Yoneda, A. Yoshida, Y. Zhao, Journal of the Physical Society of Japan **73**, 2593 (2004).

[14] Y.T. Oganessian, V.K. Utyonkoy, Y.V. Lobanov, F.S. Abdullin, A.N. Polyakov, I.V. Shirokovsky, Y.S. Tsyganov, G.G. Gulbekian, S.L. Bogomolov, A.N. Mezentsev, S. Iliev, V.G. Subbotin, A.M. Sukhov, A.A. Voinov, G.V. Buklanov, K. Subotic, V.I. Zagrebaev, M.G. Itkis, J.B. Patin, K.J. Moody, J.F. Wild, M.A. Stoyer, N.J. Stoyer, D.A. Shaughnessy, J.M. Kenneally, R.W. Lougheed, Physical Review C: Nuclear Physics **69**, 021601/1 (2004).

[15] Y.T. Oganessian, V.K. Utyonkov, Y.V. Lobanov, F.S. Abdullin, A.N. Polyakov, I.V. Shirokovsky, Y.S. Tsyganov, G.G. Gulbekian, S.L. Bogomolov, B.N. Gikal, A.N. Mezentsev, S. Iliev, V.G. Subbotin, A.M. Sukhov, O.V. Ivanov, G.V. Buklanov, K. Subotic, M.G. Itkis, K.J. Moody, J.F. Wild, N.J. Stoyer, M.A. Stoyer, R.W. Lougheed, Physical Review C: Nuclear Physics **62**, 041604/1 (2000).

[16] Y.T. Oganessian, V.K. Utyonkov, Y.V. Lobanov, F.S. Abdullin, A.N. Polyakov, I.V. Shirokovsky, Y.S. Tsyganov, G.G. Gulbeckian, S.L. Bogomolov, B.N. Gikal, A.N. Mezentsev, S. Iliev, V.G. Subbotin, A.M. Sukhov, O.V. Ivanov, G.V. Buklanov, K. Subotic, M.G. Itkis, K.J. Moody, J.F. Wild, N.J. Stoyer, M.A. Stoyer, R.W. Lougheed, C.A. Laue, Y.A. Karelin, A.N. Tatarinov, Physical Review C **63**, 011301 (2000).

[17] Y.T. Oganessian, V.K. Utyonkov, Y.V. Lobanov, F.S. Abdullin, A.N. Polyakov, R.N. Sagaidak, I.V. Shirokovsky, Y.S. Tsyganov, A.A. Voinov, G.G. Gulbekian, S.L. Bogomolov, B.N. Gikal, A.N. Mezentsev, S. Iliev, V.G. Subbotin, A.M. Sukhov, K. Subotic, V.I. Zagrebaev, G.K. Vostokin, M.G. Itkis, K.J. Moody, J.B. Patin, D.A. Shaughnessy, M.A. Stoyer, N.J. Stoyer, P.A. Wilk, J.M. Kenneally, J.H. Landrum, J.F. Wild, R.W. Lougheed, Physical Review C: Nuclear Physics **74**, 044602/1 (2006).

[18] Y. Oganessian, Journal of Physics G: Nuclear and Particle Physics **34**, R165 (2007).

[19] K.S. Krane, *Introductory Nuclear Physics*, John Wiley and Sons, New York, (1988).

[20] S. Ćwiok, P.H. Heenen, W. Nazarewicz, Nature (London, United Kingdom) **433**, 705 (2005).

[21] V.M. Strutinsky, Nuclear Physics A**95**, 420 (1967).

[22] W. Reisdorf, M. Schädel, Z. Phys. A: Hadrons Nucl. **343**, 47 (1992).

[23] P. Armbruster, Acta Physica Polonica, B **34**, 1825 (2003).

[24] S. Hofmann, G. Münzenberg, Reviews of Modern Physics **72**, 733 (2000).

[25] J.P. Blocki, H. Feldmeier, W.J. Świątecki, Nuclear Physics A **459**, 145 (1986).

[26] T. Sikkeland, J. Maly, D.F. Lebeck, Phys. Rev. **169**, 1000 (1968).

[27] J.D. Jackson, Canadian Journal of Physics **34**, 767 (1956).

[28] W. Loveland, J. Radioanal. Nucl. Chem. **243**, 147 (2000).

[29] W.J. Świątecki, K. Siwek-Wilczyńska, J. Wilczyński, Physical Review C: Nuclear Physics **71**, 014602/1 (2005).

[30] W.J. Świątecki, K. Siwek-Wilczyńska, J. Wilczyński, Acta Physica Polonica, B **34**, 2049 (2003).

[31] I. Dragojević, *Symposium Honoring Wladyslaw Świątecki*, Lawrence Berkeley National Laboratory, (2006).

[32] W.J. Świątecki, private communication, (2007).

[33] W.J. Świątecki, private communication, (2006).

[34] S.N. Ghoshal, Physical Review **80**, 939 (1950).

[35] F.P. Heßberger, G. Münzenberg, S. Hofmann, Y.K. Agarwal, K. Poppensieker, W. Reisdorf, K.H. Schmidt, J.R.H. Schneider, W.F.W. Schneider, H.J. Schött, P. Armbruster, Zeitschrift Für Physik A: Atoms and Nuclei **322**, 557 (1985).

[36] F.P. Heßberger, S. Hofmann, D. Ackermann, V. Ninov, M. Leino, G. Münzenberg, S. Saro, A. Lavrentev, A.G. Popeko, A.V. Yeremin, C. Stodel, European Physical Journal A: Hadrons and Nuclei **12**, 57 (2001).

[37] C.M. Folden, III, S.L. Nelson, C.E. Düllmann, J.M. Schwantes, R. Sudowe, P.M. Zielinski, K.E. Gregorich, H. Nitsche, D.C. Hoffman, Physical Review C: Nuclear Physics **73**, 014611/1 (2006).

[38] G. Münzenberg, P. Armbruster, S. Hofmann, F.P. Heßberger, H. Folger, J.G. Keller, V. Ninov, K. Poppensieker, A.B. Quint, W. Reisdorf, K.-H. Schmidt, J.H.R. Schneider, H.J. Schött, K. Sümmerer, I. Zychor, M.E. Leino, D. Ackermann, U. Gollerthan, E. Hanelt, W. Morawek, D. Vermeulen, Y. Fujita, T. Schwab, Zeitschrift Für Physik A **333**, 163 (1989).

[39] S. Hofmann, F.P. Heßberger, V. Ninov, P. Armbruster, G. Münzenberg, C. Stodel, A.G. Popeko, A.V. Yeremin, S. Saro, M. Leino, Zeitschrift Für Physik A: Hadrons and Nuclei **358**, 377 (1997).

[40] G. Münzenberg, S. Hofmann, F.P. Heßberger, H. Folger, V. Ninov, K. Poppensieker, A.B. Quint, W. Reisdorf, H.J. Schött, K. Sümmerer, P. Armbruster, M.E. Leino, D. Ackermann, U. Gollerthan, E. Hanelt, W. Morawek, Y. Fujita, T. Schwab, A. Türler, Zeitschrift Für Physik A: Atomic Nuclei **330**, 435 (1988).

[41] C.M. Folden III, K.E. Gregorich, C.E. Düllmann, H. Mahmud, G.K. Pang, J.M. Schwantes, R. Sudowe, P.M. Zielinski, H. Nitsche, D.C. Hoffman, Physical Review Letters **93**, 212702/1 (2004).

[42] S. Hofmann, F.P. Heßberger, D. Ackermann, G. Münzenberg, S. Antalic, P. Cagarda, B. Kindler, J. Kojouharova, M. Leino, B. Lommel, R. Mann, A.G. Popeko, S. Reshitko, S. Saro, J. Uusitalo, A.V. Yeremin, European Physical Journal A: Hadrons and Nuclei **14**, 147 (2002).

[43] K. Morita, K. Morimoto, D. Kaji, H. Haba, E. Ideguchi, J.C. Peter, R. Kanungo, K. Katori, H. Koura, H. Kudo, T. Ohnishi, A. Ozawa, T. Suda, K. Sueki, I. Tanihata, H. Xu, A.V. Yeremin, A. Yoneda, A. Yoshida, Y.L. Zhao, T. Zheng, S. Goto, F. Tokanai, Journal of the Physical Society of Japan **73**, 1738 (2004).

[44] S. Hofmann, F.P. Heßberger, D. Ackermann, S. Antalic, P. Cagarda, S. Cwiok, B. Kindler, J. Kojouharova, B. Lommel, R. Mann, G. Münzenberg, A.G. Popeko, S. Saro, H.J. Schött, A.V. Yeremin, European Physical Journal A: Hadrons and Nuclei **10**, 5 (2001).

[45] J.M. Gates, M.A. Garcia, K.E. Gregorich, C.E. Düllmann, I. Dragojević, J. Dvořák, R. Eichler, C.M.Folden III, W. Loveland, S.L. Nelson, G.K. Pang, L. Stavsetra, R. Sudowe, A. Türler, H. Nitsche, Phys. Rev. C: Nuclear Physics, **77**, 034603 (2008).

[46] P. Eskola, Physical Review C: Nuclear Physics **7**, 280 (1973).

[47] A. Ghiorso, K. Eskola, P. Eskola, M. Nurmia, Physical Review C: Nuclear Physics **7**, 2032 (1973).

[48] S. Amiel, A. Chetham-Strode, Jr., G.R. Choppin, A. Ghiorso, B.G. Harvey, L.W. Holm, S.G. Thompson, Physical Review **106**, 553 (1957).

[49] K.E. Gregorich, J.M. Gates, Ch.E. Düllmann, R. Sudowe, S.L. Nelson, M.A. Garcia, I. Dragojević, C.M. Folden, III, S.H. Neumann, D.C. Hoffman, H. Nitsche, Physical Review C: Nuclear Physics **74**, 044611/1 (2006).

[50] W.J. Świątecki, private communication, (2004).

[51] S.L. Nelson, K.E. Gregorich, I. Dragojević, M.A. Garcia, J.M. Gates, R. Sudowe, H. Nitsche, Physical Review Letters **100**, 022501 (2008).

[52] R. Sudowe, M.G. Calvert, Ch.E. Düllmann, L.M. Farina, C.M.Folden III, K.E. Gregorich, S.E.H. Gallaher, D.C. Hoffman, S.L. Nelson, D.C. Phillips, J.M. Schwantes, R.E. Wilson, P.M. Zielinski, H. Nitsche, Radiochimica Acta **94**, 123 (2006).

[53] J.F. Ziegler, computer code SRIM-2003, available from http://www. srim.org.

[54] D.A. Peterson, private communication, (2004).

[55] K.E. Gregorich, W. Loveland, D. Peterson, P.M. Zielinski, S.L. Nelson, Y.H. Chung, Ch.E. Düllmann, C.M. Folden, III, K. Aleklett, R. Eichler, D.C. Hoffman, J.P. Omtvedt, G.K. Pang, J.M. Schwantes, S. Soverna, P. Sprunger, R. Sudowe, R.E. Wilson, H. Nitsche, Physical Review C: Nuclear Physics **72**, 014605/1 (2005).

[56] H.D. Betz, Rev. Mod. Phys. **44**, 465 (1972).

[57] K.E. Gregorich, private communication, (2004).

[58] A. Ghiorso, S. Yashita, M.E. Leino, L. Frank, J. Kalnins, P. Armbruster, J.P. Dufour, P.K. Lemmertz, Nuclear Instruments & Methods in Physics Research, Section A **269**, 192 (1988).

[59] M.M. Fowler, T.C. Sangster, M.L. Begemann-Bleich, T. Blaich, J.A. Boissevain, H.C. Britt, Y.D. Chan, A. Dacal, D.J. Fields, Z. Fraenckel, A. Gavron, A. Harmon, B.V. Jacak, R.G. Lanier, P.S. Lysaght, G. Mamane, D.J. Massoletti, M.N. Namboodiri, J. Pouliot, R.G. Stokstad, M.L. Webb, J.B. Wilhelmy, Nuclear Instruments & Methods A **281**, 517 (1989).

[60] R.B. Firestone, V.S. Shirley, C.M. Baglin, S.Y.F. Chu, J. Zipkin, *Table of Isotopes*, Wiley-Interscience, (1999).

[61] J.B. Moulton, J.E. Stephenson, R.P. Schmitt, G.J. Wozniak, Nuclear Instruments & Methods **157**, 325 (1978).

[62] E. Segre, *Nuclei and Particles*. 2nd Edition, Benjamin-Cummings, (1977.)

[63] K.H. Schmidt, Zeitschrift Für Physik A **316**, 19 (1984).

[64] C. M. Folden III, Ph.D. Thesis, University of California, Berkeley, LBNL-56749, (2004).

[65] K.E. Gregorich, private communication, (2005).

[66] I.J. Myung, J. Math. Psych., **47**, 90 (2003).

[67] Wikipedia, http://en.wikipedia.org/wiki/Maximum_likelihood (2008)

[68] K.E. Gregorich, Nucl. Instrum. Methods Phys. Res., Sect. A **302**, 135 (1991).

[69] I. Dragojević, K.E. Gregorich, Ch.E. Düllmann, M.A. Garcia, J.M. Gates, S.L. Nelson, L. Stavsetra, R. Sudowe, C.M.Folden III, H. Nitsche, in preparation, (2008).

[70] Y.T. Oganessian, A.G. Demin, N.A. Danilov, G.N. Flerov, M.P. Ivanov, A.S. Iljinov, N.N. Kolesnikov, B.N. Markov, V.M. Plotko, S.P. Tretyakova, Nuclear Physics A **273**, 505 (1976).

[71] J.B. Patin, Ph.D. Thesis, University of California, Berkeley, LBNL-49693, (2002).

[72] J.M. Gates, S.L. Nelson, K.E. Gregorich, I. Dragojević, C.E. Düllmann, C.M. Folden, III, M.A. Garcia, R. Sudowe, H. Nitsche, in preparation, (2008).

[73] W.D. Myers, W.J. Świątecki, Nuclear Physics A **601**, 141 (1996).

[74] G. Audi, O. Bersillon, J. Blachot, A.H. Wapstra, Nuclear Physics A **729**, 3 (2003).

[75] D.A. Shaughnessy, K.E. Gregorich, J.L. Adams, M.R. Lane, C.A. Laue, D.M. Lee, C.A. McGrath, V. Ninov, J.B. Patin, D.A. Strellis, E.R. Sylwester, P.A. Wilk, D.C. Hoffman, Physical Review C: Nuclear Physics **65**, 024612/1 (2002).

[76] Y.T. Oganessian, JINR Internal Report **D7**, 55 (1983).

[77] F.P. Heßberger, S. Hofmann, V. Ninov, P. Armbruster, H. Folger, G. Münzenberg, H.J. Schött, A.G. Popeko, A.V. Yeremin, A.N. Andreyev, S. Saro, Zeitschrift Für Physik A: Hadrons and Nuclei **359**, 415 (1997).

[78] G. Audi, A.H. Wapstra, C. Thibault, Nuclear Physics A **729**, 337 (2003).

[79] R. Smolanczuk, Physical Review C: Nuclear Physics **56**, 812 (1997).

[80] Z.G. Gan, J.S. Guo, X.L. Wu, Z. Qin, H.M. Fan, X.G. Lei, H.Y. Liu, B. Guo, H.G. Xu, R.F. Chen, C.F. Dong, F.M. Zhang, H.L. Wang, C.Y. Xie, Z.Q. Feng, Y. Zhen, L.T. Song, P. Luo, H.S. Xu, X.H. Zhou, G.M. Jin, Z. Ren, European Physical Journal A: Hadrons and Nuclei **20**, 385 (2004).

[81] C.E. Bemis, Jr., P.F. Dittner, R.J. Silva, R.L. Hahn, J.R. Tarrant, L.D. Hunt, D.C. Hensley, Physical Review C: Nuclear Physics **16**, 1146 (1977).

[82] K. Eskola, P. Eskola, M. Nurmia, A. Ghiorso, Phys. Rev. C **[3]4**, 632 (1971).

[83] K. Morita, A. Yoshida, T.T. Inamura, M. Koizumi, T. Nomura, M. Fujioka, T. Shinozuka, H. Miyatake, K. Sueki, H. Kudo, Y. Nagai, T. Toriyama, K. Yoshimura, Y. Hatsukawa, Nucl. Instrum. Methods Phys. Res., Sect. B **70**, 220 (1992).

[84] K.M. Hartmann, D.H.E. Gross, Zeitschrift Für Physik A **311**, 131 (1983).

[85] D. Leitner, M.L. Galloway, T.J. Loew, C.M. Lyneis, I.C. Rodriguez, D.S. Todd, available from: http://ecrgroup.lbl.gov/papers_pdf/VENUS-ICIS2007_accepted_Figures.pdf (2008).

Disclaimer

This work was supported in part by the Director, Office of High Energy and Nuclear Physics, Nuclear Physics Division of the U.S. Department of Energy, under contract DE-AC02-05CH11231.